An International ICT R&D Journal Sponsored by ZTE Corporation

ISSN 1673-5188
CN 34-1294/ TN

ZTE COMMUNICATIONS

中兴通讯技术(英文版)

http://tech-en.zte.com.cn

September 2020, Vol. 18 No. 3

Antennas and RF Technologies for 5G/B5G Mobile Communications

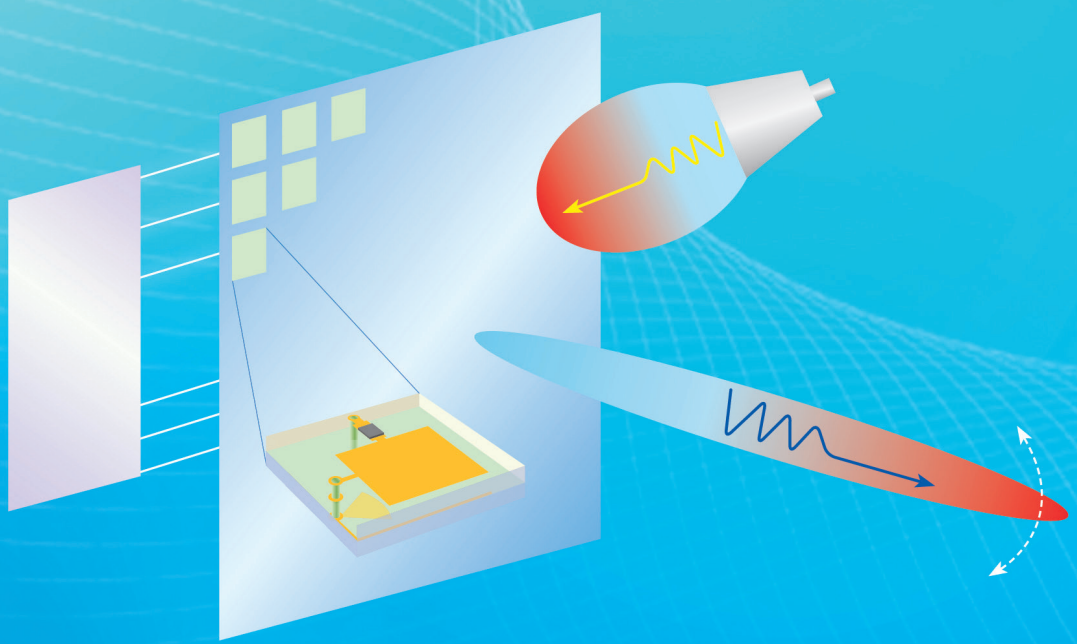

9 771673 518208 09>

The 8th Editorial Board of ZTE Communications

CONTENTS

ZTE COMMUNICATIONS September 2020 Vol. 18 No. 3 (Issue 71)

Special Topic

Antennas and RF Technologies for 5G/B5G Mobile Communications

CONTENTS

ZTE COMMUNICATIONS September 2020 Vol. 18 No. 3 (Issue 71)

Serial parmeters:CN 34-1294/TN*2003*q*16*70*en*P*¥ 20.00*5000*10*2020-09

Editorial: Special Topic on Antennas and RF Technologies for 5G/B5G Mobile Communications


Guest Editor

LI Ronglin received the B. S. degree in electrical engineering from Xi'an Jiaotong University, China in 1983, and the M. S. and Ph. D. degrees in electrical engineering from Chongqing University, China in 1990 and 1994, respectively. From 1983 to 1987, he worked as an assistant electrical engineer at Yunnan Electric Power Research Institute, China. From 1994 to 1996, he was a postdoctoral research fellow with Zhejiang University, China. In 1997, he visited Hosei University, Japan, as an HIF (Hosei International Fund) Research Fellow. In 1998, he became a professor with Zhejiang University. In 1999, he visited the University of Utah, USA, as a research associate. In 2000, he worked as a research fellow at the Queen's University of Belfast, UK. Since 2001, he has been a research scientist with Georgia Institute of Technology, USA. He is now an Endowed Professor with the South China University of Technology, China. Dr. LI has published more than 200 papers in refereed journals and conference proceedings, and authored three book chapters. His current research interests include new design techniques for antennas in mobile and satellite communication systems, phased arrays and smart antennas for radar applications, wireless sensors and RFID technology, electromagnetics, and information theory.


Guest Editor

ZHANG Yueping is a full professor with the School of Electrical and Electronic Engineering, Nanyang Technological University, Singapore, a distinguished lecturer of the IEEE Antennas and Propagation Society (IEEE AP-S), a member of the IEEE AP-S Paper Award Committee, and a Fellow of IEEE. Dr. ZHANG has published numerous papers, including two invited and one regular papers in the *Proceedings of the IEEE* and one invited paper in the *IEEE Transactions on Antennas and Propagation*. He is the first and only Chinese radio scientist who has managed to publish an article on radio history in the English learned journal, *IEEE Antennas and Propagation Magazine*. He received the prestigious 2012 IEEE AP-S Schelkunoff Prize Paper Award. Prof. ZHANG holds seven US patents. He has made pioneering and significant contributions to the development of Antenna-in-Package (AiP) technology for which he received the 2020 IEEE AP-S Kraus Antenna Award. His current research interests include the development of Antenna-on-Chip (AoC) technology for Very Large Scale Antenna Integration (VLSAI) and characterization of chip-scale propagation channels at terahertz for Wireless Chip Area Network (WCAN).


Guest Editor

MA Jianguo received the B. S. degree from Lanzhou University, China in 1982, and the Ph. D. degree in engineering from the University of Duisburg-Essen, Germany in 1996. He was with the Technical University of Nova Scotia, Canada, as a post-doctor fellow from 1996 to 1997. From 1997 to 2005, he was with Nanyang Technological University (NTU), Singapore, as a faculty member, where he was also the Founding Director of the Center for Integrated Circuits and Systems, NTU. From 2006 to 2009, he was with the University of Electronic Science and Technology of China. From 2009 to 2016, he was the dean of the School of Electronic Information Engineering, Tianjin University, China. Now he is with Guangdong University of Technology, China. His current research interests include microwave electronics, RFIC applications for wireless networks, RF device characterization and modeling, and Terahertz microelectronic systems. As a co-inventor, he holds 44 granted international patents from UK and USA and more than 50 granted invention patents from China. Dr. MA is the vice chair for Standard Committee of IEEE CRFID and a member of the IEEE MTT-S Publication Committee. He was a member of the Editorial Board of the *Proceedings of the IEEE* in 2013 – 2018 and a member of the IEEE University Program Ad Hoc Committee from 2010 to 2013. He served as an associate editor for *IEEE Microwave and Wireless Components Letters* in 2003 – 2005 and has been an associate editor for *IEEE Microwave Magazine* since 2018. Dr. MA is the Editor-in-Chief for *IEEE Transactions on Microwave Theory and Techniques*. He is a Fellow of IEEE.

The 5G mobile communication systems are being deployed worldwide and China has been a global leader in the new technology. The number of base stations for 5G mobile communications is increasing by more than ten thousand every week in China. By the end of this year, about 500 000 base stations will be built up nationwide, covering more than 300 cities. The beyond 5G (B5G) mobile systems with enhanced transmission technologies are also being developed and attracting much attention. The emerging millimeter wave (mmW) and massive multiple-input multiple-output (MIMO) technologies are expected to become key enabling technologies for 5G/B5G mobile communications. In China, the mmW bands 24.75 – 27.5 GHz and 37 – 42.5 GHz have been allocated for future 5G/B5G trials and it is anticipated that the 5G/B5G mobile communication systems based on mmW massive MIMO technologies will be ready for commercial use in 2022. As the key components in these communication systems, antennas and RF front ends play an important role in implementing ubiquitous connection among hundreds of different devices in 5G/B5G networks.

DOI: 10.12142/ZTECOM.202003001
Citation (IEEE Format): R. L. Li, Y. P. Zhang, and J. G. Ma, "Editorial: special topic on antennas and RF technologies for 5G/B5G mobile communications," *ZTE Communications*, vol. 18, no. 3, pp. 01 – 02, Sept. 2020. doi: 10.12142/ZTECOM.202003001.

LI Ronglin, ZHANG Yueping, MA Jianguo

In this special issue, we have collected seven papers concerning antennas and RF technologies for 5G/B5G mobile communications. Beamforming and multibeam are crucial technologies for mmW massive MIMO based 5G/B5G applications. Leaky-wave antennas (LWAs) are very suitable for beamforming in mmW bands. The paper "Leaky-Wave Antennas for 5G/B5G Mobile Communication Systems: A Survey" by HE et al. presents an overview of LWAs for 5G/B5G mobile communication systems. Classification and design methods of LWAs are introduced. The latest research progress of LWAs for 5G/B5G mobile communication systems is demonstrated. Challenges and future research directions of LWAs are discussed. Low loss, simple structure and broadband for beamforming LWAs are also essential for 5G/B5G mobile communication systems. Multibeam base station antennas are required to meet the increasing demands for higher data rates in 5G/B5G networks. In the paper "Multibeam Antenna Based on Butler Matrix for 3G/LTE/5G/B5G Base Station Applications", YE et al. propose a compact dual-band dual-polarized two-beam antenna array and a wideband dual-polarized two-beam antenna array for base-station applications. The dual-band dual-polarized two-beam antenna array is formed by two interleaved sub-arrays and two individual beamforming networks for different frequency operation. The wideband two-beam antenna array is composed of three 4 × 2 subarrays and two beam-forming networks. The proposed methods can easily be extended to the design of other multibeam base-station antenna arrays. Moreover, the paper "A Novel 28 GHz Phased Array Antenna for 5G Mobile Communications" by LI et al. presents a phased array antenna consisting of 16 × 16 patch elements. The antenna integrated with a wave control circuit can perform real-time beam scanning by reconfiguring the phase of an antenna unit. A prototype of the antenna is fabricated and measured to demonstrate the feasibility of this approach. The phased array has the advantages of low power consumption, low cost, and conformal geometry, suitable for base stations in B5G mmW mobile communication systems.

Antenna-in-package (AiP) technology has been widely adopted in mmW bands. It is believed that AiP technology may provide ultimate antenna solutions to 5G/B5G devices in the lower mmW bands. The paper "Design of Millimeter-Wave Antenna-in-Package (AiP) for 5G NR" by CHANG et al. discusses the design of mmW AiP for 5G spectrum. The system architectures and design considerations for 5G phased arrays are presented. Beamforming IC and up/down converter chips, fabrication technologies and materials, antenna and transition design, and feeding networks and filters design are described. A 4×4 low temperature co-fired ceramic (LTCC) unit AiP module for the 5G band (27.5 – 28.35 GHz) is designed and manufactured. A larger 8×8 array is also demonstrated by tiling up to four-unit modules on one single motherboard. The key design considerations of the beamforming antenna array are low loss, compact system and small size. In the paper "Integrated 3D Fan-out Package of RF Microsystem and Antenna for 5G Communications", XIA et al. investigate a three-dimensional (3D) fan-out packaging method for the integration of 5G communication RF microsystem and antennas. Through the double-sided wiring technology on the glass wafer, the fabrication of 5G antenna arrays is realized. A slot coupling antenna for 5G communications is fabricated on a 12-inch glass wafer. The antenna can operate at 60 GHz with a maximum gain of 6 dBi, which implies a feasible solution to the 3D fan-out integration of RF microsystem and antennas for 5G communications. Such a 3D fan-out integrated prototype is designed and manufactured.

Electronic design automation (EDA) software that can accurately simulate antennas, radio chips and microwave components is essential for 5G technologies. The paper "Electromagnetic Simulation with 3D FEM for Design Automation in 5G Era" by BALEWSKI et al. reviews challenges facing commercial tools for design of wireless devices where electromagnetic effects have to be taken into account. The focus is on simulation software based on finite-element method (FEM). Novel computational techniques based on FEM are introduced into state-of-the-art EDA software to accelerate numerical analysis, as well as to enable optimization, sensitivity analysis and interactive design tuning based on the rigorous electromagnetic model of a device. Several of these new techniques, helping to mitigate the most challenging issues related to FEM based simulation, are highlighted. It is demonstrated that these new computational techniques can significantly reduce the time needed for design closure with the acceleration rates reaching factors as large as tens or even over one hundred.

The paper "Robust Digital Predistortion for LTE/5G Power Amplifiers Utilizing Negative Feedback Iteration" by LIU et al. proposes a robust digital predistortion (DPD) technique utilizing negative feedback iteration for linearizing power amplifiers. Different from the conventional direct learning and indirect learning structure, the proposed DPD suggests a two-step method to identify the predistortion. A negative feedback-based iteration is used to estimate the optimal DPD signal. The corresponding DPD parameters are extracted by forward modeling with the input signal and optimal DPD signal. The iteration can be applied to both single-band and dual-band PAs, which will achieve superior linear performance than conventional direct learning DPD while having a relatively low computational complexity.

We would like to thank all the authors for their valuable contributions and all the reviewers for their timely and constructive comments on the submitted manuscripts. We hope that this special issue is informative and useful for all readers.

Leaky-Wave Antennas for 5G/B5G Mobile Communication Systems: A Survey

HE Yejun[1], JIANG Jiachun[1], ZHANG Long[1], LI Wenting[1], WONG Sai-Wai[1], DENG Wei[2], CHI Baoyong[2]

(1. College of Electronics and Information Engineering, Shenzhen University, Shenzhen 518060, China; 2. Institute of Microelectronics, Tsinghua University, Beijing 100084, China)

Abstract: Since leaky-wave antennas (LWAs) have the advantages of high directivity, low loss and structural simplicity, LWAs are very suitable for designing millimeter-wave (mmW) antennas. The purpose of this paper is to review the latest research progress of LWAs for 5G/B5G mobile communication systems. Firstly, the conventional classification and design methods of LWAs are introduced and the effects of the phase constant and attenuation constant on the radiation characteristics are discussed. Then two types of new LWAs for 5G/B5G mobile communication systems including broadband fixed-beam LWAs and frequency-fixed beam-scanning LWAs are summarized. Finally, the challenges and future research directions of LWAs for 5G/B5G mobile communication systems are presented.

Keywords: 5G/B5G; beam-scanning; frequency-fixed; fixed-beam; millimeter-wave (mmW); leaky-wave antenna (LWA)

DOI: 10.12142/ZTECOM.202003002

https://kns.cnki.net/kcms/detail/34.1294.TN.20200909.1435.004.html, published online September 10, 2020

Manuscript received: 2020-06-16

Citation (IEEE Format): Y. J. He, J. C. Jiang, L. Zhang, et al., "Leaky-wave antennas for 5G/B5G mobile communication systems: a survey," *ZTE Communications*, vol. 18, no. 3, pp. 03 – 11, Sept. 2020. doi: 10.12142/ZTECOM.202003002.

1 Introduction

Due to the rapid growth of mobile data services, the existing spectrum resources can no longer meet the requirements of mobile communication systems. In order to increase the data transmission rate, a higher carrier frequency must be used to provide greater bandwidth. Since the millimeter-wave (mmW) frequency band has rich spectrum resources which can provide greater bandwidth, mmW antennas can be used in 5G/B5G mobile communication systems.

Unlike traditional 4G antennas, mmW antennas must have the characteristics of low loss and high directivity to counteract the greater path loss of mmW propagation in free space. The dimensions of mmW antennas are in the level of millimeters, which poses a challenge to their process technology. Thus, the 5G/B5G mmW antennas should be designed as simply as possible. In addition, 5G/B5G mmW antennas should also have the characteristic of broadband to support 5G/B5G high data rate transmissions.

Generally, antenna arrays are used to generate highly directional beams. However, in mmW systems, the feeding network of an array antenna significantly increases the system complexity and brings additional loss to the system. Phased-array antennas have the characteristics of electrically controlled

This work is supported in part by the National Natural Science Foundation of China (NSFC) under Grants 62071306 and 61801299, in part by the Mobility Program for Taiwan Young Scientists under Grant RW2019TW001, and in part by Shenzhen Science and Technology Program under Grants GJHZ20180418190529516 and JSGG20180507183215520.

beam-scanning and high directivity[1]. In Ref. [2], the design considerations and solutions of mmW phased-array antennas applied to 5G smartphones are discussed in detail. Multi-beam antennas[3-4] can simultaneously generate multiple beams with the high directivity, where each beam covers a predetermined angular range. In Ref. [5], the applicability of multi-beam antennas for 5G mobile communications and related challenges are introduced. However, phased-array antennas and multi-beam antennas have complex feeding networks, which is not conducive to massive production. Since leaky-wave antennas (LWAs) have the advantages of high directivity, low loss, and structural simplicity, they are expected to be an effective solution for 5G/B5G mmW antennas.

This paper is organized as follows. In Section 2, the classification and design methods of LWAs are introduced. Section 3 describes the latest research progress of LWAs for 5G/B5G mobile communication systems. Section 4 presents the challenges and future research directions of LWAs for 5G/B5G mobile communication systems. Finally, we draw the conclusions in Section 5.

2 Classification and Design Methods of LWAs

LWAs are based on guided wave structures and can continuously radiate along their guided wave structures. Since LWAs have a large radiation aperture and do not require a complicated feeding network, their structures are very simple and they have the characteristics of low loss and high directivity.

2.1 Classification of LWAs

Generally, LWAs can be categorized into three types, namely uniform LWAs, periodic LWAs and quasi-uniform LWAs[6].

A uniform LWA has a constant cross section along its guided wave structure. Since its fundamental mode is a fast wave ($\beta_0 < k_0$), it can radiate when its guided wave structure is open. When a uniform LWA is fed, its main beam scans from endfire direction to broadside direction as frequency increases. However, in most practical designs, the beam of a uniform LWA cannot scan to endfire or broadside direction. As shown in **Fig. 1**[7], it is difficult for a slotted air-filled rectangular waveguide LWA to scan to broadside direction since the operating frequency corresponds to the cut-off frequency of the waveguide. It is also difficult for a slotted air-filled rectangular waveguide LWA to scan to endfire direction since the long slot of the rectangular waveguide is equivalent to a magnetic current source, and the endfire direction corresponds to the radiation zero point of the magnetic current source.

Compared with uniform LWAs, the fundamental mode of a periodic LWA is a slow wave. Thus, even if its guided wave structure is open, it cannot radiate. However, since a periodic LWA introduces periodic modulations along its guided wave structure, an infinite number of space harmonics[8-9] are generated in the guided wave structure of the periodic LWA, where each space harmonic has a phase constant

$$\beta_n = \beta_0 + 2\pi n/p, \quad (1)$$

where β_0 is the fundamental mode phase constant of the periodic LWA (slightly different from the fundamental mode phase constant when there is no periodic modulations), n is the harmonic order, and p is the period length. Although the fundamental mode of a periodic LWA is a slow wave, it is possible to obtain a space harmonic (usually the first space harmonic) that is a fast wave by designing a certain period length. As shown in **Fig. 2**, a rectangular dielectric rod with periodic metal strips is a classic example of periodic LWAs[10]. Compared with the uniform LWA, the main advantage of a periodic LWA is that its phase constant can be negative (for example, $\beta_{-1} < k_0$), thus allowing its beam scan from backward to forward. However, due to the open stop band of periodic structures, the performance of a periodic LWA significantly deteriorates when its beam is scanned close to the broadside direction[8-9]. The reason is that the period length is equal to the fundamental mode guided wavelength of the periodic LWA at the frequency corresponding to the open stop band. Thus, the

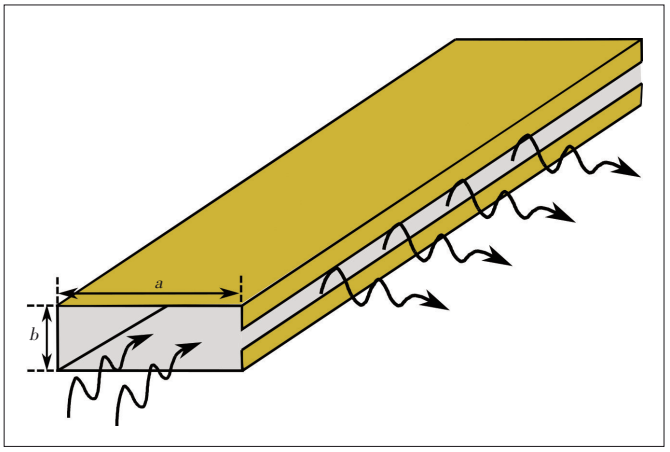

▲Figure 1. A slotted air-filled rectangular waveguide.

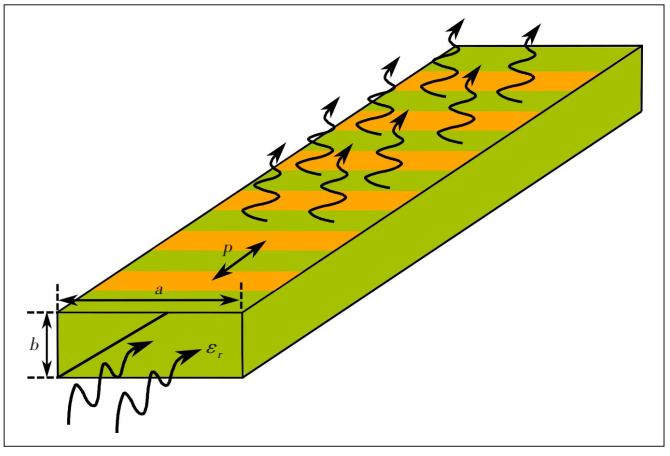

▲Figure 2. A rectangular dielectric rod with periodic metal strips.

reflections from all periodic elements are superposed in phase so that most of the energy is reflected back to the input port of the periodic LWA. In recent years, many articles have proposed various methods to suppress the open stop band of periodic LWAs[11 - 16].

Similar to periodic LWAs, a quasi-uniform LWA also introduces periodic modulation along its guided wave structure. Thus, it can also generate infinite space harmonics. However, the fundamental mode of the quasi-uniform LWA is a fast wave like uniform LWAs, and its period length is selected to be small enough to ensure that radiation only comes from the fundamental mode. Thus, the period length of a uniform LWA does not directly determine the radiation mode. However, periodic modulations can be used to control the attenuation constant of leaky mode. A classic example of quasi-uniform LWAs is shown in **Fig. 3**, where it radiates by a series of closely spaced periodic holes which are on the side wall of an air-filled rectangular waveguide[17]. Compared with the slotted air-filled rectangular waveguide LWA[7], this design can provide a smaller attenuation constant since periodic holes cannot completely cut the current lines on the side wall of the rectangular waveguides. However, the long slot of the side wall of the rectangular waveguides in Fig. 1 cuts the current lines.

2.2 Design Methods of LWAs

LWAs can be designed by the microstrip line[18 - 23] and substrate integrated waveguide (SIW)[24 - 29]. Their radiation characteristics are determined by the phase constants and attenuation constants where the phase constants determine their beam directions and the attenuation constants determine their beam widths. The beam direction of an LWA can be approximated as

$$\theta = \arcsin(\beta/k_0), \tag{2}$$

where θ is the angle measured from the broadside direction, β is the phase constant of the LWA, and k_0 is the propagation constant of free space. The guided wave structure of an LWA is dispersive, which means that its phase constant does not change linearly with frequency, resulting in β/k_0 to change with frequency. Thus, the beam of an LWA will be scanned with frequency. We can obtain the required beam-scanning range by controlling the phase constant of an LWA. The beam width $\Delta\theta$ of an LWA can be approximated as

$$\Delta\theta = 2(\alpha/k_0)/\sin(\theta), \tag{3}$$

where α is the attenuation constant. We can obtain a narrow beam by designing a small attenuation. The reason is that an LWA with small attenuation needs a long guided wave structure to fully radiate energy, and the long guided wave structure means that the effective radiation aperture is large.

Uniform LWAs use their fundamental mode to radiate. When designing a uniform LWA, we must first determine which waveguide will be used. The required operating band and phase constant of a uniform LWA can be obtained by selecting the geometry and material of its waveguide. As shown in Fig. 1, the width and height of the rectangular are used to determine its operating band and phase constant. By adjusting the geometry of the slot, the attenuation constant can be controlled to obtain the required beam width. Quasi-uniform LWAs are similar to uniform LWAs, except that quasi-uniform LWAs introduce periodic disturbances such as the periodic holes. As shown in Fig. 3, the attenuation constant of the rectangular waveguide can be controlled by adjusting the geometry and spacing of the holes to obtain the required beam width.

Since the fundamental mode of a periodic LWA is a slow wave, periodic modulation needs to be introduced to allow it to radiate. Periodic modulations will introduce infinite space harmonics and the phase constant of each space harmonic can be expressed as $\beta_n = \beta_0 + 2\pi n/p$. It can be seen that even if its fundamental mode is a slow wave, we can also obtain a space harmonic which is a fast wave. Usually the first space harmonic is used to radiate and its phase constant can be expressed as $\beta_{-1} = \beta_0 - 2\pi/p$. By properly selecting the period length, an operating band, where the first space harmonic wave is a fast wave and the rest of the harmonics waves are slow waves, can be obtained. Within this operating frequency band, controllable single beam radiation can be achieved. Fig. 2 shows a classic periodic LWA. Its guided wave structure is a rectangular dielectric rod. The width and height of the dielectric rod are a and b, respectively, and the dielectric constant is ϵ_r. the fundamental mode phase constant β_0 of the dielectric rod can be determined by these parameters. By properly selecting the period length of the periodic metal strips, a specified operating frequency band with the first harmonic being the fast wave and the remaining harmonics being the slow waves can be obtained, thereby obtaining the designated single beam-scanning range within the designated operating frequency band. By adjusting the geometry of the metal strip, the attenuation con-

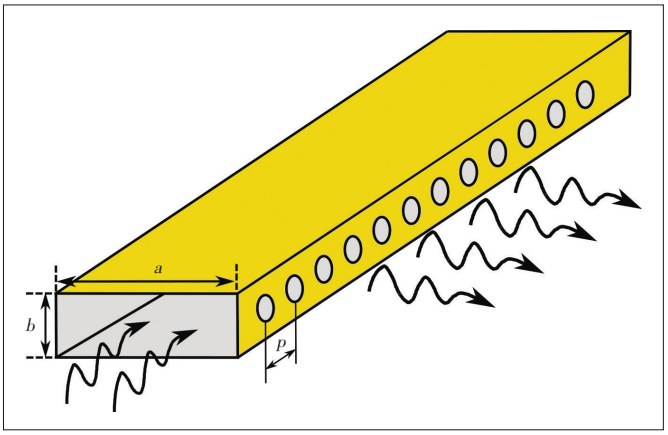

▲**Figure 3. An air-filled rectangular waveguide with closely spaced periodic holes.**

stant can be controlled to obtain the specified beam width.

3 Latest Research Progress of LWAs for 5G/B5G Mobile Communication systems

3.1 Broadband Fixed Beam LWAs

The characteristic of frequency beam-scanning makes the pattern bandwidth (3 dB bandwidth of fixed direction radiated power density) of LWAs very narrow. The 5G/B5G antennas as devices for receiving and transmitting electromagnetic signals should have the characteristic of broadband to obtain high data rate transmissions. In order to improve the pattern bandwidth of LWAs, various methods to reduce or completely cancel the dispersion characteristics of LWAs have been proposed[30 - 36].

In Ref. [30], an LWA loaded with a Huygens metasurface is proposed, which works in the *X*-band. As shown in **Fig. 4**, by loading a Huygens matasurface above a coplanar waveguide (CPW) LWA, the frequency beam squint of the LWA can be effectively reduced. This reduction is due to the frequency dependence of the metasurface. In Ref. [31], an LWA loaded with a prism is proposed, which is integrated on a dielectric board. By loading a prism with complementary dispersion characteristics on the radiation aperture of the LWA, the frequency beam squint of the LWA can be eliminated. The operating principle is illustrated in **Fig. 5**. The LWA has a 20% 3 dB pattern bandwidth, and in the frequency range of 35 GHz to 40 GHz, the steering of the main radiation direction is only ±0.5°.

In Ref. [32], a low-dispersion LWA based on groove gap waveguide[33] technology is proposed. Similar to Ref. [31], a prism with complementary dispersion characteristics is used to reduce frequency beam squint. The difference is that by using low-loss groove gap waveguide technology, higher gain and radiation efficiency are obtained in the frequency band of 11.4 GHz to 13.4 GHz. **Fig. 6** shows the structure of this LWA. In Ref. [34], a hybrid dispersion compensation method is proposed to reduce the frequency beam squints of LWAs. It can be seen as a combination of Refs. [30] and [32]. **Fig. 7** illustrates the operating principles of the LWA when only the metasurface is loaded and when the complementary lens and metasurface are simultaneously loaded. Compared with Ref. [32], by loading a gradient metasurface in front of the radiation aperture of the lens, the dimension of the compensation lens is reduced to a quarter of that in Ref.

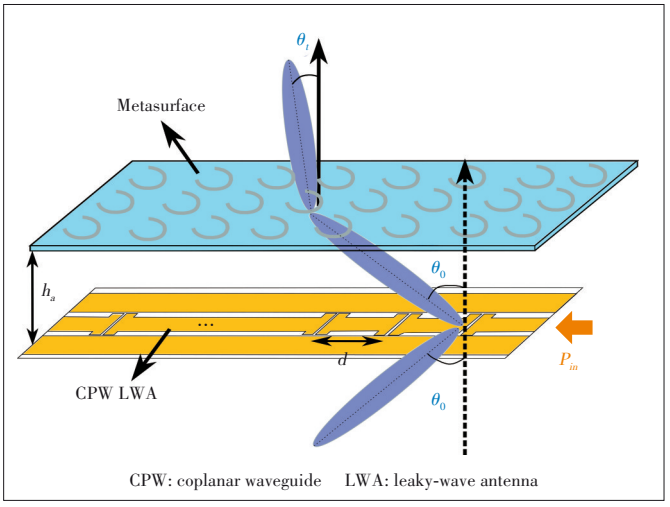

▲**Figure 4. A CPW LWA with a Huygens metasurface.**

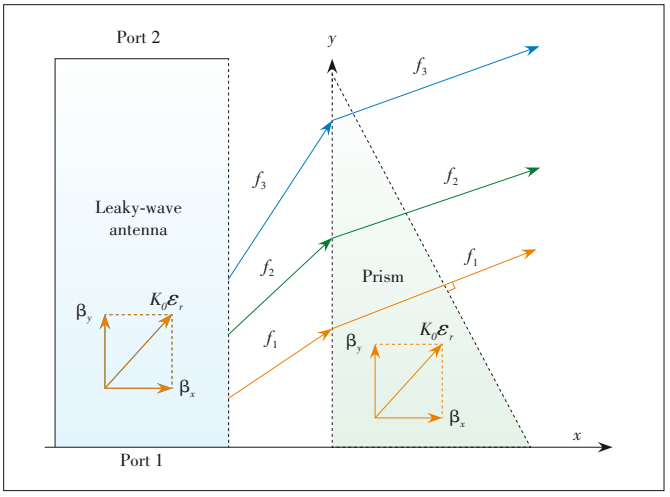

▲**Figure 5. Operating principle of a prism to eliminate beam squinting of leaky-wave antennas.**

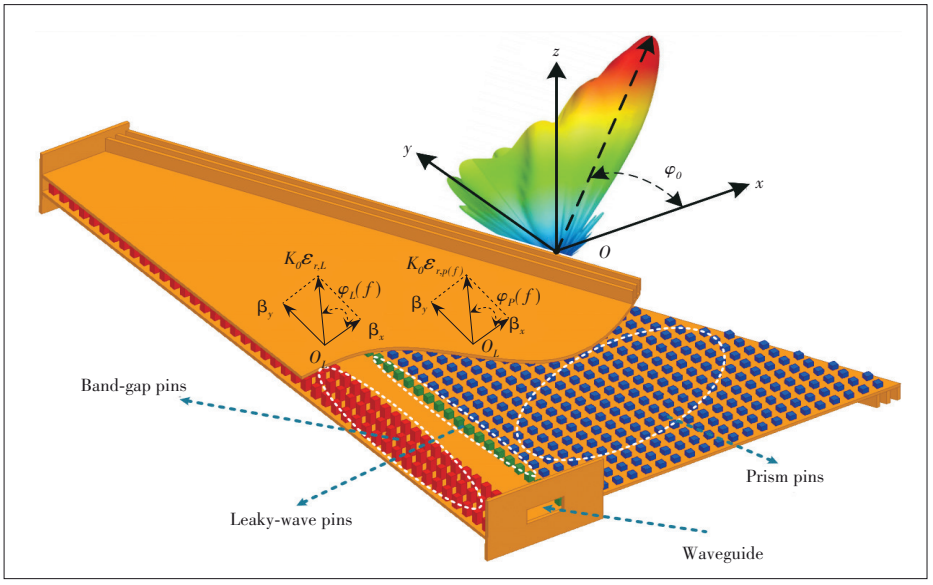

▲**Figure 6. Low-dispersion leaky-wave antenna (LWA) in groove-gap waveguide technology[32].**

[32] and the beam direction can be customized.

In Ref. [35], a low-dispersion LWA operating in the 60 GHz band is proposed. Similar to Ref. [32], the frequency beam squint of the LWA is reduced by loading a lens with complementary dispersion characteristics on the radiation aperture of the LWA. The difference is that the electromagnetic band gap structure, leakage structure, and lens structure are all implemented with metal periodic round holes, as shown in **Fig. 8**. Thus, the solution in Ref. [35] has higher cost-efficiency and a more stable manufacturing process. Ref. [36] is based on the design ideas of Ref. [32]. Compared with Ref. [32], it discusses how to simultaneously obtain low side lobes and low dispersion characteristics. In addition, it is confirmed that an LWA loaded with a complementary dispersion lens can simultaneously generate dual beams. In Ref. [36], two low-dispersion LWAs that operate in the 60 GHz band are designed. These two antennas use symmetric and asymmetric structures, respectively. The asymmetric structure can obtain the optimal side lobes and the symmetric structure can simultaneously obtain two stable beams. Both LWAs can obtain 20% bandwidth when the beam tilt angle is within ±0.5°. In the operating frequency band, the gains obtained by the asymmetric and symmetric structures are stable at 17 dBi and 15 dBi, respectively. A comparison of the broadband fixed beam LWAs introduced above is given in **Table 1**.

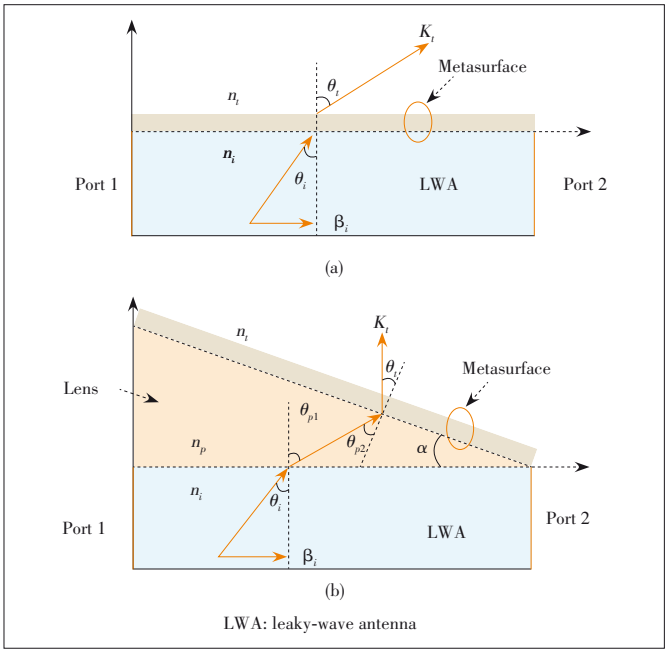

▲ **Figure 7. Operating principles of LWAs (a) loaded with metasurface and (b) loaded with both metasurface and compensation lens.**

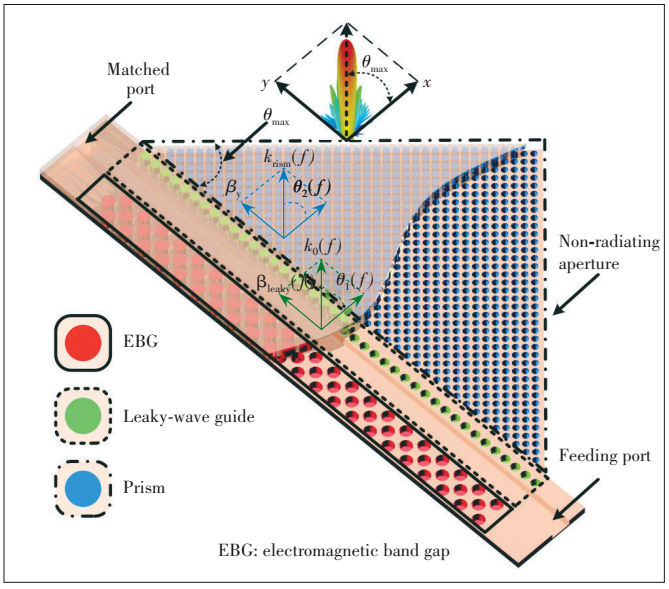

▲ **Figure 8. Low-dispersion leaky-wave antenna (LWA) using fully holey groove gap waveguide technology[35].**

3.2 Frequency-Fixed Beam-Scanning LWAs

5G mmW antennas should have high directivity to counteract the greater path loss of mmW propagation in free space. However, the disadvantage of a highly directional beam is that its beam width becomes narrower, resulting in a smaller coverage area. Using an LWA with frequency-fixed beam-scanning capability can improve beam coverage.

In Ref. [37], a frequency-fixed circularly polarized beam-scanning LWA is proposed. The unit cells of the LWA are composed of a varactor diode and a subwavelength square patch. As shown in **Fig. 9**, changing the capacitance of the varactor diode can control the dispersion behavior of the LWA. By adding different bias voltages, the capacitance of the varactor diode can be changed, thereby realizing electronically controlled frequency-fixed beam-scanning. In Ref. [38], an LWA composed of corrugated microstrip lines with triangular modulation surface impedance is proposed (**Fig. 10**). Due to the periodic modulation of the surface impedance, the guided waves propagating on the microstrip line can be effectively converted into leaky waves. By adding different bias voltages, the capacitance of the varactor diode can be changed, thereby controlling the surface impedance of the corrugated microstrip line. Different surface impedances correspond to different dispersion behaviors, thus, the electronically controlled beam-scanning of the LWA can be achieved by changing the bias voltage. This LWA can reach a beam-scanning range of 45° at each frequency from 5.5 to 5.8 GHz.

In Ref. [39], a frequency-fixed beam-scanning LWA based on a corrugated substrate integrated waveguide is proposed. **Fig. 11** shows its structure. The unit cells of the LWA consist of a rectangular ring slot and a metallic via connected to the ground. The rectangular ring slot is loaded by four varactor diodes. By adjusting the direct current (DC) bias voltage, the series and shunt capacitance of the varactor diodes can be controlled. Thus, the dispersion behaviors of the LWA can be controlled by the DC bias voltages to obtain electronically controlled frequency-fixed beam-scanning. In Ref. [40], a composite right/left-hand (CRLH) microstrip LWA enabling frequen-

▼Table 1. Comparison of the broadband fixed beam LWAs

	Antenna Type	Guided Wave Structure	Advantage	Operating Frequencies/GHz	Max Gain/dBi	Beam Squinting/°
[30]	LWA loaded with metasurface	Coplanar waveguide	• Simple structure	9.5 – 10.45	5	12
[31]	LWA loaded with prism	Substrate integrated waveguide	• Lightweight • Easy to integrate with other circuits	35 – 40	8.5	1
[32]	LWA loaded with prism	Groove gap waveguide	• Low loss	11.5 – 13	16.5	0.6
[34]	LWA loaded with prism and metasurface	Ridged gap waveguid	• Custom beam direction • Miniturization	9.3 – 11.3 (Radiating at an angle of 38.3°)	15.7	1.5
				9.5 – 11.3 (Radiating at an angle of −0.4°)	15.2	1.2
[35]	LWA loaded with prism	Groove gap waveguide	• Low side lobe level • High cost-efficiency • Stable manufacturing process	54.81 – 61.19 (Glide-symmetric)	16.5	3.4
				54.81 – 61.19 (Mirror-symmetric)	17.5	1.8
[36]	LWA loaded with prism	Groove gap waveguide	• Low side lobe level • Dual beam radiation	54 – 66 (Asymmetric)	17	1
				54 – 66 (Symmetric)	15	1

LWA: leaky-wave antenna

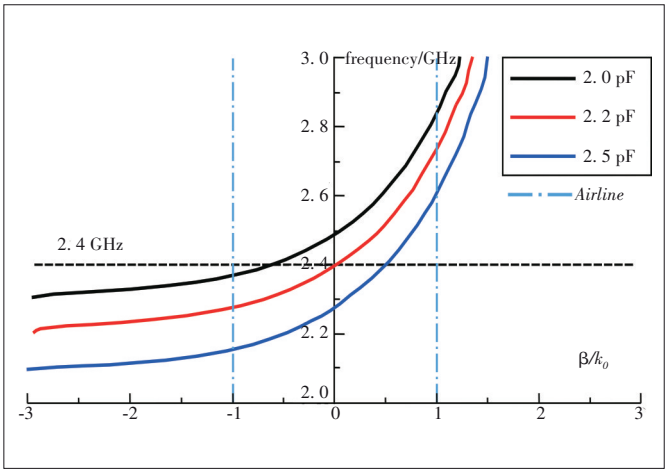

▲Figure 9. Dispersion curves corresponding to different capacitances of the varactor diodes[37].

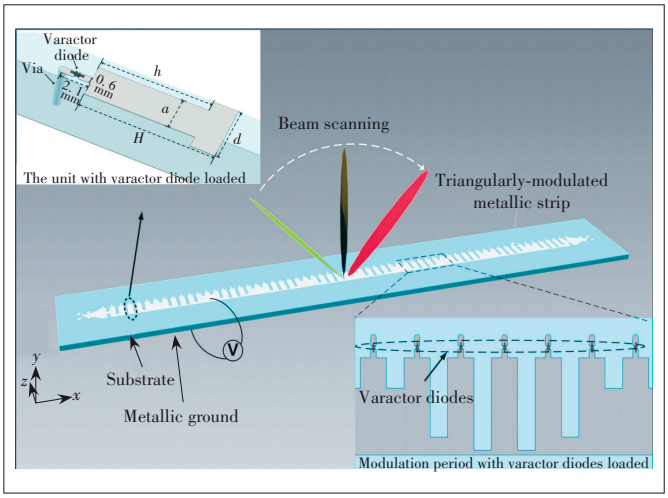

▲Figure 10. Corrugated microstrip leaky-wave antenna (LWA) loaded with varactor diodes[38].

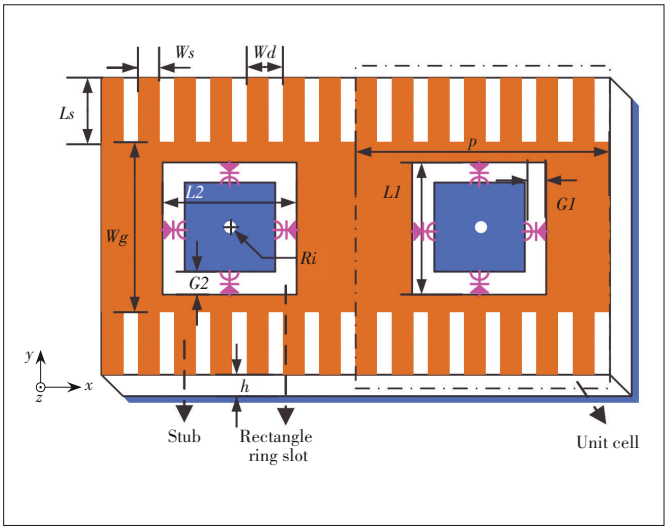

▲Figure 11. Structure of the corrugated substrate integrated waveguide leaky-wave antenna (LWA)[39].

cy-fixed electronically controlled beam-scanning in the frequency band of 4.75 GHz to 5.25 GHz is designed. **Fig. 12** shows its structure. By loading two sets of varactor diodes, the circuit parameters of the CRLH microstrip LWA can be controlled to change its dispersion behavior. Thus, by adding different amplitudes bias voltages to change the capacitance of the varactor diodes, the electronically controlled frequency-fixed beam-scanning can be achieved. The measured results show that it can achieve beam-scanning from −37° to 32° at 5 GHz and from −15° to 34° at 5.25 GHz.

In Ref. [41], a method is proposed to achieve frequency-fixed beam-scanning by controlling the period lengths of periodic LWAs. The designed antenna consists of a substrate integrated waveguide with an H-shaped slot and two rows of patch

elements. Two symmetrical dumbbell-shaped slots are etched on the element. **Fig. 13** shows the structure and equivalent circuit of the element. By controlling the operating state of each patch element through the diode on the parasitic strip, the LWA can obtain different effective period lengths at a frequency-fixed; thus, the frequency-fixed electronically controlled beam-scanning capability can be obtained. The measured results show that the antenna can achieve 125° beam-scanning range and the peak gain can reach 11.8 dBi. A comparison of the frequency-fixed beam-scanning LWAs introduced above is given in **Table 2**.

4 Challenges and Future Research Directions of LWAs

Leaky-wave antennas play a very important role in 5G/B5G mmW mobile communication systems, especially affecting the performance of the entire mobile communication systems. A high-performance transceiver antenna can significantly improve the communication quality. In order to obtain a high gain beam to counteract the greater path loss of mmW propagation in free space, 5G/B5G mmW antennas should have the characteristics of high directivity and low loss. In addition, in order to improve the data transmission rate, 5G/B5G mmW antennas should also have a larger bandwidth. Based on these requirements, both fixed-beam and frequency-fixed beam-scanning LWAs are still facing the challenges of low loss, simple structure and broadband.

Since LWAs have the characteristics of high directivity, low loss and structural simplicity, they are very suitable for designing mmW antennas. However, due to the dispersion characteristics of LWAs, their beams scan with frequency. Thus, the 3 dB pattern bandwidths of LWAs are very narrow, which is not conducive to high data rate transmission for 5G/B5G mobile communication systems. How to increase the pattern bandwidth of LWAs is a major challenge. Some recent articles have proposed several methods of using complementary metasurfaces or lenses to cancel the dispersion characteristics of LWAs. Although these methods effectively improve the pattern bandwidth of LWAs, they make the antenna structure larger and increase the complexity and losses of LWAs. In addition, more complex structures are not con-

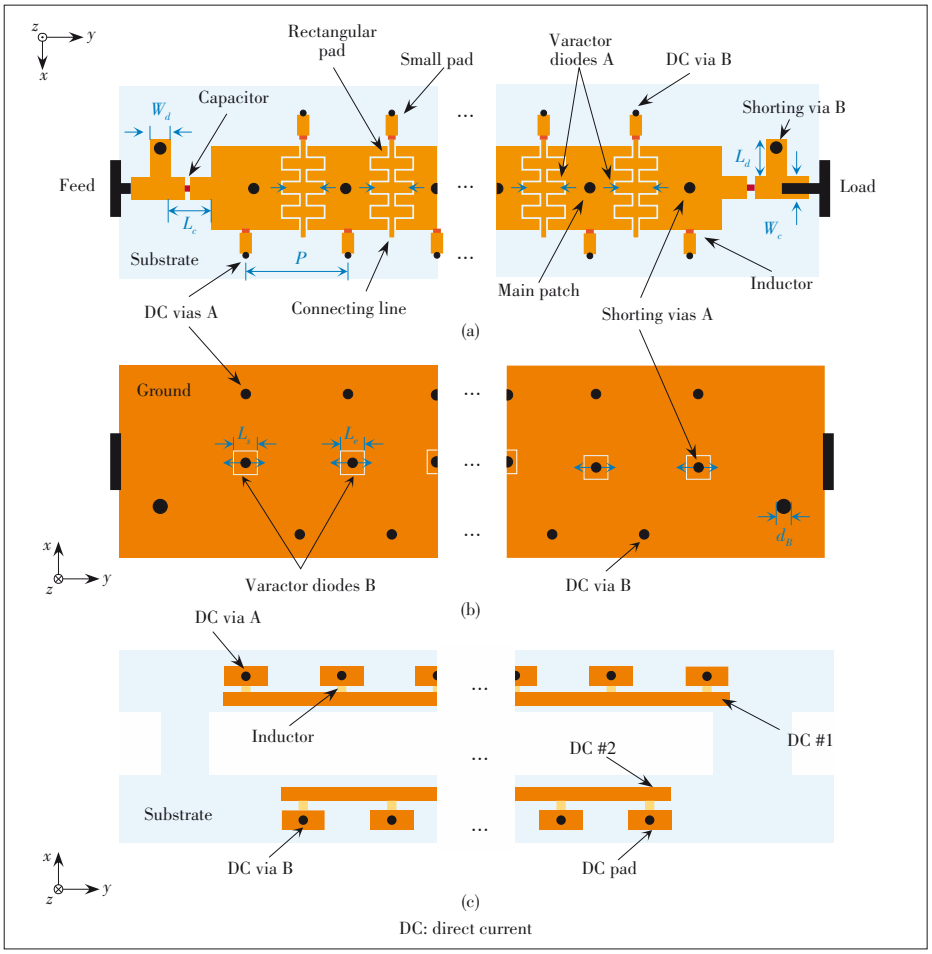

▲**Figure 12. Composite right/left-hand (CRLH) leaky-wave antenna (LWA) configuration[40]: (a) top view of the patch layer; (b) bottom view of the ground layer; (c) bottom view of the biasing layer.**

▼**Table 2. Comparison of the frequency-fixed beam-scanning LWAs**

	Antenna Type	Operating Principle	Operating Frequencies/GHz	Max Gain/dBi	Beam Scanning Range/deg
[37]	CRLH	Manipulation on dispersion characteristic	2.4	6.15	40 to −17
[38]	Corrugated microstrip line	Modulation on surface impedance	5.5 – 5.8	8	−16 to 27 (at 5.8 GHz)
[39]	Corrugated SIW	Manipulation on dispersion characteristic	4.5	7.5	−40.66 to 31.32
[40]	Microstrip CRLH	Manipulation on dispersion characteristic	5	5.7	−37 to 32
			5.25	6.4	−15 to 34
[41]	Slotted SIW	Reconfiguration of period length	5	11.8	−60 to 65

CRLH: composite right/left-hand LWA: leaky-wave antenna SIW: substrate integrated waveguide

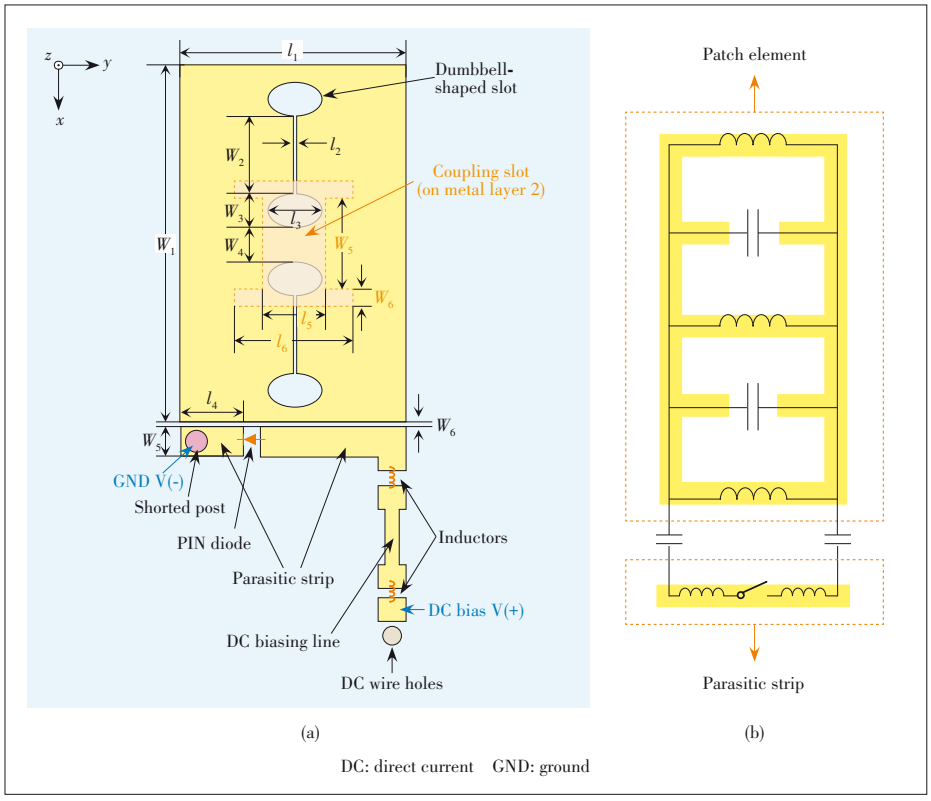

▲**Figure 13. Configuration and equivalent circuit of the patch element proposed in [41]: (a) element structure; (b) equivalent circuit model.**

ducive to cost efficiency. Thus, how to obtain a larger pattern bandwidth without significantly increasing the complexity of LWAs is an important research direction of LWAs.

The 5G/B5G mmW mobile communication system requires an antenna with high directivity that also means a smaller coverage area. Using LWA with frequency-fixed beam-scanning capability can improve beam coverage. Recent articles have introduced various methods to achieve frequency-fixed beam-scanning, most of which use active circuits to control the dispersion characteristics of LWAs to achieve frequency-fixed electronically controlled beam-scanning. Due to the introduction of active circuits, the loss will increase and the structures become more complicated. How to overcome these problems is another important research direction of LWAs. In addition, most frequency-fixed beam-scanning LWAs can only be implemented at one frequency or a narrow band. How to achieve frequency-fixed beam-scanning in a broadband range is also a major challenge for LWAs.

5 Conclusions

This paper reviews the recent research on LWAs for 5G/B5G mobile communication systems. The structural characteristics and radiation characteristics of uniform LWAs, quasi-uniform LWAs and periodic LWAs are first introduced in detail. The latest studies on broadband fixed-beam LWAs and frequency-fixed beam-scanning LWAs are then presented. The operating principles and applicability to 5G/B5G mobile communication systems of the broadband fixed-beam LWAs and frequency-fixed beam-scanning LWAs are discussed. Future research directions on LWAs for 5G/B5G mobile communication systems should be how to obtain a larger pattern bandwidth without significantly increasing the complexity of LWAs and how to achieve frequency-fixed beam-scanning in a broadband range.

References

[1] REBEIZ G M, KIM S-Y, INAC O, et al. Millimeter-wave large-scale phased-arrays for 5G systems [C]//IEEE MTT-S International Microwave Symposium. Phoenix, USA: IEEE, 2015: 1 – 3. DOI: 10.1109/MWSYM.2015.7167090
[2] HONG W, BAEK K, KO S. Millimeter-wave 5G antennas for smartphones: overview and experimental demonstration [J]. IEEE transactions on antennas and propagation, 2017, 65(12): 6250 – 6261. DOI: 10.1109/TAP.2017.2740963
[3] MARZETTA T L. Noncooperative cellular wireless with unlimited numbers of base station antennas [J]. IEEE transactions on wireless communications, 2010, 9(11): 3590 – 3600. DOI: 10.1109/TWC.2010.092810.091092
[4] BOGALE T E, LE L B. Massive MIMO and mmwave for 5G wireless hetnet: potential benefits and challenges [J]. IEEE Vehicular technology magazine, 2016, 11(1): 64 – 75. DOI: 10.1109/MVT.2015.2496240
[5] HONG W, JIANG Z, YU C, et al. Multibeam antenna technologies for 5G wireless communications [J]. IEEE transactions on antennas and propagation, 2017, 65(12): 6231 – 6249. DOI: 10.1109/TAP.2017.2712819
[6] JACKSON D R, OLINER A A. Leaky-wave antennas [M]//Balanis CA. Modern antenna handbook. New York, USA: Wiley, 2008
[7] HANSEN W W. Radiating electromagnetic waveguide: U.S. Patent No. 2,402, 622 [P]. 1940
[8] HESSEL A. General characteristics of traveling-wave antennas: in antenna theory [M]. New York, USA: McGraw-Hill, 1969
[9] TAMIR T. Leaky-wave antennas: in antenna theory [M]. New York, USA: McGraw-Hill, 1969
[10] HINES J N, UPSON J R. A wide aperture tapered-depth scanning antenna [R]. Columbus, USA: OH, 1957
[11] PAULOTTO S, BACCARELLI P, FREZZA F, et al. A novel technique for open-stopband suppression in 1-D periodic printed leaky-wave antennas [J]. IEEE transactions on antennas and propagation, 2009, 57(7): 1894 – 1906. DOI: 10.1109/TAP.2009.2019900
[12] LIU J, ZHOU W, LONG Y. A simple technique for open-stopband suppression in periodic leaky-wave antennas using two nonidentical elements per unit cell [J]. IEEE transactions on antennas and propagation, 2018, 66(6): 2741 – 2751. DOI: 10.1109/TAP.2018.2819701
[13] KARMOKAR D, GUO Y, QIN P, et al. Substrate integrated waveguide-based periodic backward-to-forward scanning leaky-wave antenna with low cross-polarization [J]. IEEE transactions on antennas and propagation, 2108, 66(8): 3846 – 3856. DOI: 10.1109/TAP.2018.2835502

[14] LYU Y, LIU X, WANG P, et al. Leaky-wave antennas based on non-cutoff substrate integrated waveguide supporting beam scanning from backward to forward [J]. IEEE transactions on antennas and propagation, 2016, 64(6): 2155 – 2164. DOI: 10.1109/TAP.2016.2550054
[15] CHEN S, KARMOKAR D, LI Z, et al. Circular-polarized substrate-integrated-waveguide leaky-wave antenna with wide-angle and consistent-gain continuous beam scanning [J]. IEEE transactions on antennas and propagation, 2019, 67 (7): 4418 – 4428. DOI: 10.1109/TAP.2019.2911398
[16] ZHOU W, LIU J, LONG Y. Applications of the open-stopband suppression in various periodic leaky-wave antennas with tapered half-wavelength line [J]. IEEE transactions on antennas and propagation, 2019, 67(11): 6811 – 6820. DOI: 10.1109/TAP.2019.2925192
[17] OLINER A A, JOHNSON D R. Leaky-wave antennas [M]//Volakis J. Antenna engineering handbook. New York, USA: McGraw-Hill, 2007
[18] MENZEL W. A new travelling-wave antenna in microstrip [C]//8th European Microwave Conference, Paris, France: IEEE, 1978. DOI: 10.1109/EUMA.1978.332503
[19] XIE D, ZHU L, ZHANG X. An EH0-mode microstrip leaky-wave antenna with periodical loading of shorting pins [J]. IEEE transactions on antennas and propagation, 2017, 65(7): 3419 – 3426. DOI: 10.1109/TAP.2017.2700882
[20] XIE D, ZHU L. Microstrip leaky-wave antennas with nonuniform periodical loading of shorting pins for enhanced frequency sensitivity [J]. IEEE transactions on antennas and propagation, 2018, 66(7): 3337 – 3345. DOI: 10.1109/TAP.2018.2829884
[21] LIU J, LI Y, LONG Y. Design of periodic shorting-vias for suppressing the fundamental mode in microstrip leaky-wave antennas [J]. IEEE transactions on antennas and propagation, 2015, 63(10): 4297 – 4304. DOI: 10.1109/TAP.2015.2459136
[22] LYU Y, MENG F, YANG G, et al. Periodic leaky-wave antenna based on complementary pair of radiation elements [J]. IEEE transactions on antennas and propagation, 2018, 66(9): 4503 – 4515. DOI: 10.1109/TAP.2018.2842304
[23] KARMOKAR D, ESSELLE K, BIRD T. Wideband microstrip leaky-wave antennas with two symmetrical side beams for simultaneous dual-beam scanning [J]. IEEE transactions on antennas and propagation, 2016, 64(4): 1262 – 1269. DOI: 10.1109/TAP.2016.2529646
[24] LIU J, JACKSON D, LONG Y. Substrate integrated waveguide (SIW) leaky-wave antenna with transverse slots [J]. IEEE transactions on antennas and propagation, 2012, 60(1): 20 – 29. DOI: 10.1109/TAP.2011.2167910
[25] XU F, WU K, ZHANG X. Periodic leaky-wave antenna for millimeter wave applications based on substrate integrated waveguide [J]. IEEE transactions on antennas and propagation, 2010, 58(2): 340 – 347. DOI: 10.1109/TAP.2009.2026593
[26] CHENG Y, HONG W, WU K, et al. Millimeter-wave substrate integrated waveguide long slot leaky-wave antennas and two-dimensional multibeam applications [J]. IEEE transactions on antennas and propagation, 2010, 59(1): 40 – 47. DOI: 10.1109/TAP.2010.2090471
[27] GENG Y, WANG J, LI Y, et al. High-efficiency leaky-wave antenna array with sidelobe suppression and multibeam generation [J]. IEEE antennas and wireless propagation letters, 2017, 16: 2787 – 2790. DOI: 10.1109/LAWP.2017.2746090
[28] DONG Y, ITOH T. Composite right/left-handed substrate integrated waveguide and half mode substrate integrated waveguide leaky-wave structures [J]. IEEE transactions on antennas and propagation, 2011, 59(3): 767 – 775. DOI: 10.1109/TAP.2010.2103025
[29] ZHOU W, LIU J, LONG Y. Investigation of shorting vias for suppressing the open stopband in an SIW periodic leaky-wave structure [J]. IEEE transactions on microwave theory and techniques, 2018, 66(6): 2936 – 2945. DOI: 10.1109/TMTT.2018.2818140
[30] MEHDIPOUR A, WONG J, ELEFTHERIADES G. Beam-squinting reduction of leaky-wave antennas using huygens metasurfaces [J]. IEEE transactions on antennas and propagation, 2015, 63(3): 978 – 992. DOI: 10.1109/TAP.2015.2389240
[31] WANG L, GÓMEZ-TORNERO J, QUEVEDO-TERUEL O. Substrate integrated waveguide leaky-wave antenna with wide bandwidth via prism coupling [J]. IEEE transactions on microwave theory and techniques, 2018, 66(6): 3110 – 3118. DOI: 10.1109/TMTT.2018.2818149
[32] WANG L, GÓMEZ-TORNERO J, RAJO-IGLESIAS E, et al. Low-dispersive leaky-wave antenna integrated in groove gap waveguide technology [J]. IEEE transactions on antennas and propagation, 2018, 66(11): 5727 – 5736. DOI: 10.1109/TAP.2018.2863115
[33] RAJO-IGLESIAS E, FERRANDO-ROCHER M, ZAMAN A. Gap waveguide technology for millimeter-wave antenna systems [J]. IEEE communications magazine, 2018, 56(7): 14 – 20. DOI: 10.1109/MCOM.2018.1700998
[34] CHEN J, YUAN W, ZHANG C, et al. Wideband leaky-wave antennas loaded with gradient metasurface for fixed-beam radiations with customized tilting angles [J]. IEEE transactions on antennas and propagation, 2020, 68(1): 161 – 170. DOI: 10.1109/TAP.2019.2940542
[35] CHEN Q, ZETTERSTROM O, PUCCI E, et al. Glide-symmetric holey leaky-wave antenna with low dispersion for 60 GHz point-to-point communications [J]. IEEE transactions on antennas and propagation, 2020, 68(3): 1925 – 1936. DOI: 10.1109/TAP.2019.2944535
[36] ZETTERSTROM O, PUCCI E, PADILLA P, et al. Low-dispersive leaky-wave antennas for mmwave point-to-point high-throughput communications [J]. IEEE transactions on antennas and propagation, 2019, 68(3): 1322 – 1331. DOI: 10.1109/TAP.2019.2943437
[37] FU J-H, LI A, CHEN W, et al. An electrically controlled CRLH-inspired circularly polarized leaky-wave antenna [J]. IEEE antennas and wireless propagation letters, 2017, 16: 760 – 763. DOI: 10.1109/LAWP.2016.2601960
[38] WANG M, MA H, ZHANG H, et al. Frequency-fixed beam-scanning leaky-wave antenna using electronically controllable corrugated microstrip line [J]. IEEE transactions on antennas and propagation, 2018, 66(9): 4449 – 4457. DOI: 10.1109/TAP.2018.2845452
[39] CHEN K, ZHANG Y, HE S, et al. An electronically controlled leaky-wave antenna based on corrugated SIW structure with fixed-frequency beam scanning [J]. IEEE antennas and wireless propagation letters, 2019, 18(3): 551 – 555. DOI: 10.1109/LAWP.2019.2896354
[40] CHEN S, KARMOKAR D, LI Z, et al. Continuous beam scanning at a fixed frequency with a composite right-/left-handed leaky-wave antenna operating over a wide frequency band [J]. IEEE transactions on antennas and propagation, 2019, 67(12): 7272 – 7284. DOI: 10.1109/TAP.2019.2935088
[41] LI Z, GUO Y, CHEN S, et al. A period-reconfigurable leaky-wave antenna with fixed-frequency and wide-angle beam scanning [J]. IEEE transactions on antennas and propagation, 2019, 67(6): 3720 – 3732. DOI: 10.1109/TAP.2019.2907636

Biographies

HE Yejun (yjhe@szu.edu.cn) received his Ph.D. degree in Information and Communication Engineering from Huazhong University of Science and Technology (HUST), China in 2005. Since 2011, he has been a professor with the College of Electronics and Information Engineering, Shenzhen University, China, where he is currently the Director of the Guangdong Engineering Research Center of Base Station Antennas and Propagation and the Director of the Shenzhen Key Laboratory of Antennas and Propagation. He was selected as Pengcheng Scholar Distinguished Professor, Shenzhen, China. He was also a recipient of the Shenzhen Overseas High-Caliber Personnel Level B ("Peacock Plan Award" B) and Shenzhen High-Level Professional Talent (Local Leading Talent). He was a visiting professor first at the University of Waterloo, Canada and later at Georgia Institute of Technology, USA. He received the 2016 Shenzhen Science and Technology Progress Award and the 2017 Guangdong Provincial Science and Technology Progress Award. He has authored or co-authored about 200 research papers and books (chapters), and holds about 20 patents. His research interests include wireless communications, antennas and radio frequency. Dr. HE is a Fellow of IET and the Chair of IEEE Antennas and Propagation Society—Shenzhen Chapter. He is serving as the associate editor of *IEEE Network*, *International Journal of Communication Systems*, *China Communications*, and *Wireless Communications and Mobile Computing*.

➡ To Page 41

Multibeam Antenna Based on Butler Matrix for 3G/LTE/5G/B5G Base Station Applications

YE Lianghua[1], CAO Yunfei[2], ZHANG Xiuyin[2]

(1. School of Physics and Optoelectronic Engineering, Guangdong University of Technology, Guangzhou 510600, China;
2. School of Electronic and Information Engineering, South China University of Technology, Guangzhou 510600, China.)

Abstract: With the rapid development of mobile communication technology and the explosion of data traffic, high capacity communication with high data transmission rate is urgently needed in densely populated areas. Since multibeam antennas are able to increase the communication capacity and support a high data transmission rate, they have attracted a lot of research interest and have been actively investigated for base station applications. In addition, since multi-beam antennas based on Butler matrix (MABBMs) have the advantages of high gain, easy design and low profile, they are suitable for base station applications. The purposes of this paper is to provide an overview of the existing MABBMs. The specifications, principles of operation, design method and implementation of MABBMs are presented. The challenge of MABBMs for 3G/LTE/5G/B5G base station applications is discussed in the end.

Keywords: multi-beam antenna; base station application; Butler matrix; wideband antenna; multi-band antenna

DOI: 10.12142/ZTECOM.202003003

https://kns.cnki.net/kcms/detail/34.1294.TN.20200903.1755.002.html, published online September 4, 2020

Manuscript received: 2020-08-06

Citation (IEEE Format): L. H. Ye, Y. F. Cao, and X. Y. Zhang, "Multibeam antenna based on Butler matrix for 3G/LTE/5G/B5G base station applications," *ZTE Communications*, vol. 18, no. 3, pp. 12–19, Sept. 2020. doi: 10.12142/ZTECOM. 202003003.

1 Introduction

The high-capacity communication is urgently needed in densely populated areas with the fast growth of mobile communication technology and the development of data traffic. In order to increase the channel capacity for mobile communications, two main typical methods are usually employed. One is to improve the frequency bandwidth by employing wideband or multiband antennas[1-5], and the other is to divide a sector into multiple ones by using multibeam antennas[6-23]. Moreover, both the two methods, namely wideband/multiband and multibeam operation, can be simultaneously used to further enhance the communication capacity. For example, to improve the capacity, a conventional sector base station antenna can be replaced by a wideband or dual-band multibeam. In addition, as one of the key technologies of 5G communications, the multi-beam antenna technology, widely employed for 3G/LTE/5G mobile communication and as a potential technology for B5G mobile communication, is able to provide high data transmission rate, improved signal-to-interference-plus-noise ratio, increased spectral and energetic efficiency, and versatile beam shaping[24].

To realize the design of a multibeam antenna, several typical methods have been employed. One approach is to employ a reflector antenna. Multiple beams radiated at different angles can be easily obtained by placing multiple feeds at different positions in front of a reflector antenna[6-10]. Another method is to use a lens antenna[11-14]. When a lens is excited by multiple feeds in different points, the propagation direction of the electromagnetic wave can be changed by the focusing or reflection function of the lens, thus generating multiple radia-

tion beams[15 - 17]. However, reflector-based and lens-based multibeam antennas suffer from large dimensions, which are generally suitable for millimeter wave frequencies, while not suitable for sub 6 GHz base station applications. Since multi-beam antennas fed by Butler matrix have advantages of high gain, low profile and simple structure [18 - 24], they are expected to be an effective solution of multi-beam antenna for 3G/LTE/5G/B5G mobile communication systems.

In this paper, the multi-beam antennas based on Butler matrix (MABBM) technologies are reviewed. This paper is organized as follows. In Section 2, the specifications for base station applications are discussed. In Section 3, the principles of operation and design approach of MABBMs are provided. Section 4 discusses the latest research progress of MABBMs for mobile communication systems. Section 5 presents the challenges and Section 6 gives the conclusions.

2 Specifications for Base-Station Applications

For practical base station applications, several important specifications of an MABBM should be required. The first one is that the multiple beams need to exhibit stable 10 dB beam width of around 120° in the horizontal plane to realize good coverage. The second specification is that the cross level between adjacent beams is required to be around −10 dB for good communication, as observed in **Fig. 1**. If it is too high, the signals from two sectors will overlap, which will cause continual handoff. On the contrary, the good coverage is not guaranteed if the cross level is too low. The third specification is that the side lobe and grating lobe for each beam should be suppressed in a low level, to reduce signal interference with neighbor beams. Therefore, MABBMs with such performances over a multiple frequency or wide frequency band are in urgent need to meet the application requirements of base stations in densely populated areas.

3 Design Principle and Method of MABBMs

As a kind of passive multiport network, Butler matrix[25 - 27] has advantages of multiple phase differences, low loss, low profile and simple structure, which has been widely employed as antenna feeding network for multi-beam radiation. When an $N \times M$ Butler matrix is connected to an antenna array with M elements, N independent beams with different directions can be produced as the input ports are excited simultaneously. The principles of operation and design method of multi-beam antennas based on Butler matrix are described in detail below.

3.1 Principles of Operation for MABBMs

The beam-scanning theory of the antenna array is used to analyze the working mechanism of an antenna array for generating multi-beam radiation, which can be employed to guide the comprehensive design of MABBMs. According to the comprehensive theory of antenna array[28], the beam-scanning angle θ_0 of a linear antenna array can be calculated as follows.

$$\theta_0 = \arcsin\left(-\frac{\varphi\lambda}{2\pi d}\right), \tag{1}$$

where φ and d represent the phase difference and spacing between adjacent elements respectively, and λ represents the wavelength associated with the working frequency in vacuum, with the schematic diagram shown in **Fig. 2**. According to Eq. (1), it is seen that the beam-scanning direction of the antenna array is determined by the wavelength λ corresponding to the operating frequency of the antenna, the phase difference φ and the spacing d between adjacent elements. When the working frequency and spacing are selected, the

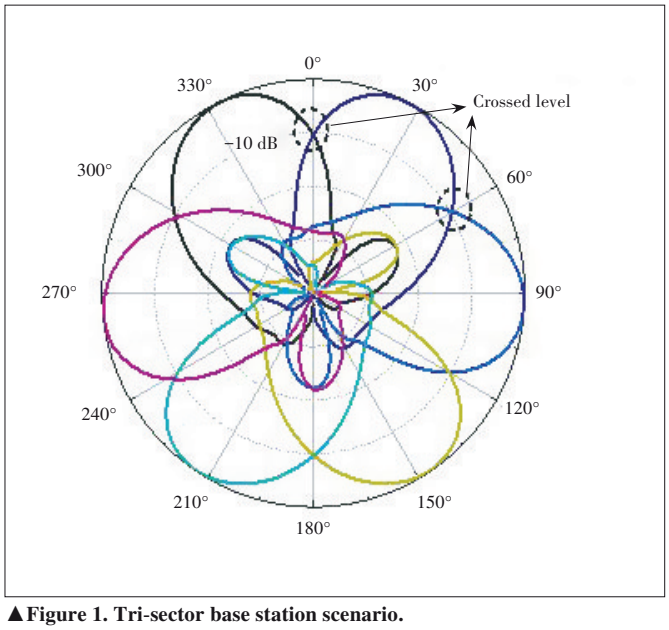

▲Figure 1. Tri-sector base station scenario.

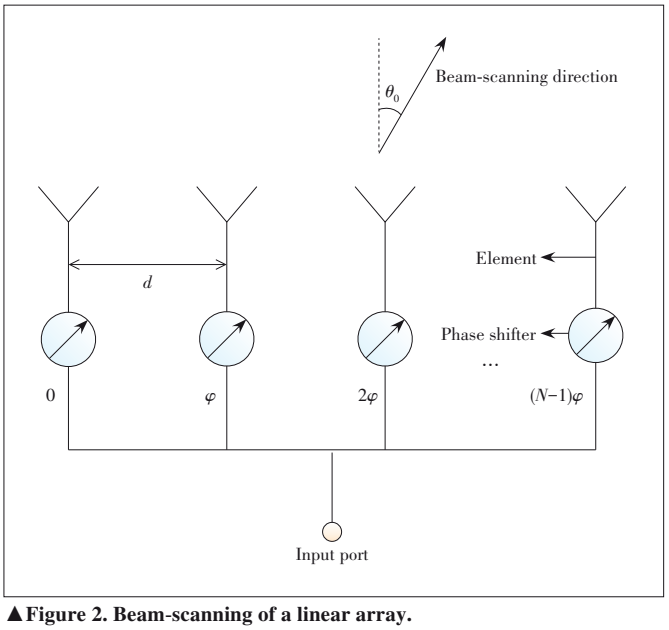

▲Figure 2. Beam-scanning of a linear array.

beam-scanning direction of the array is only determined by the phase difference of adjacent elements, and different phase differences produce different beam-scanning directions. Therefore, when multiple signals with different phase differences excite an antenna array simultaneously, the antenna array can radiate multiple beams with different directions, realizing multi-beam radiation.

Fig. 3 shows the radiation pattern of a three-beam antenna array fed by a 3 × 5 Butler matrix at 2.2 GHz. The element is a half-wavelength electric dipole, and the spacing between elements is 75 mm. The excitation of the array has equal amplitude and phase differences of −120°, 0°, +120°. It can be seen that 3 beams with different directions have been successfully produced for the MABBM.

3.2 Design Method of MABBMs

In practical applications, the multi-beam radiation of the MABBMs includes two types: multiple beams in the horizontal plane or in the vertical plane[29 - 30], and 2D multiple beams in both horizontal and vertical planes[31 - 33]. In order to simplify the analysis without loss of generality, this paper provides the design method of MABBMs with multiple beams in the horizontal plane. Another type of 2D MABBMs can be designed in a similar way. Generally, a 1D MABBM is mainly formed by an $M \times L$ array, $N \times M$ Butler matrices and L-way power dividers, as shown in **Figs. 4a**, **4b** and **4c** respectively. The design steps of the MABBM can be summarized as follows.

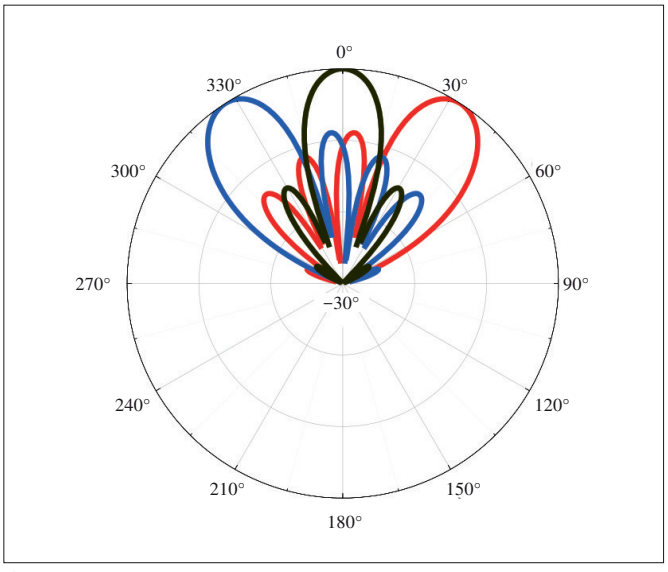

▲**Figure 3. Radiation pattern of three-beam antenna array.**

Step 1: Implementing $N \times M$ Butler matrix. Firstly, the numbers (N) of radiation beams of an MABBM and input ports of Butler matrix are determined. The communication capacity is associated with the number of radiation beams, with greater number of radiation beams providing more capacity. The number of radiation beams is obtained by the communication capacity required, which is equal to the number of input ports of Butler matrix. Then the numbers (M) of the output ports of the Butler matrix, and the amplitude and phase difference of the Butler matrix are determined by the side lobe level required for each beam. On the basis above, the $N \times M$ Butler matrix is designed, which will meet the bandwidth, amplitude and phase difference requirements.

Step 2: Designing $M \times L$ array. The number (M) of elements in the horizontal plane of the array is equal to the number of the output ports of the Butler matrix, and the number (L) of the elements in the vertical plane is determined by the required gain. In addition, the spacing between adjacent elements in the horizontal plane plays an important role in the coverage area of the multiple beams and cross level between adjacent beams, which should be carefully selected. On this basis, the antenna element is designed, which will meet the requirement of the needed bandwidth and then the required $M \times L$ array is implemnted.

Step 3: Implementing the MABBM. The output port of each power splitter is connected to the antenna element in the vertical plane through 50 Ω coaxial cables firstly, and then the input port of each power splitter is connected to the output port of the Butler matrix through 50 Ω coaxial cables for implementing the proposed multi-beam antenna.

4 Latest Research Progress of MABBMs for Base-Station Applications

Recently, various MABBMs have been proposed for mobile communication applications. In Ref. [34], a compact dual-

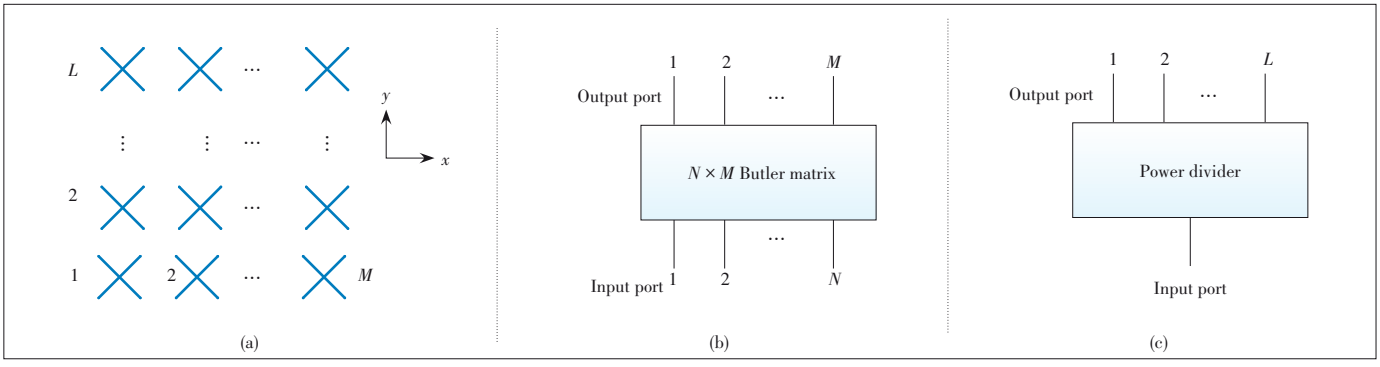

▲**Figure 4. Multi-beam antenna based on $N \times M$ Butler matrix with (a) $M \times L$ array; (b) $N \times M$ Butler matrix; (c) power divider.**

band two-beam 4 × 8 antenna array with dual polarizations for base station applications is proposed. It consists of two 4 × 4 subarrays operating at 3G (1 710 – 2 170 MHz) and long term evolution (LTE) (2 490 – 2 690 MHz) bands. For size miniaturization, the elements of the two 4 × 4 subarrays are interleaved with each other, as shown in **Fig. 5a**. The mutual coupling between the elements operating at different bands is suppressed by using filtering antennas[35] with out-of-band radiation suppression. To obtain stable two-beam radiation patterns within the two operating bands, the beam-forming networks with little magnitude and phase imbalances are specially designed for each band. The configuration of the beam-forming network is illustrated in **Fig. 5b.** It is composed of one 2 × 4 Butler matrix and four filtering power dividers (PDs).The array exhibits a stable 10 dB beam width around 120° in the azimuth plane within the two entire bands, and the two-beam radiation patterns satisfy the coverage requirement of 120° in the azimuth plane for base station applications. Additionally, 16.4 dBi/15.5 dBi peak gains and around −10 dB cross levels at the junction of two beams are achieved within the two operating bands.

In Ref. [36], a wideband dual-polarized 4 × 6 antenna array with two beams for base station applications is provided. It consists of three 4 × 2 subarrays, with the configuration shown in **Fig. 6a**. To obtain ±45° dual-polarized radiation, a wideband crossed dipole is employed as a basic element. For each 4 × 2 subarray, the lower and upper 4 × 1 subarrays are misaligned in the horizontal plane. In this way, the 4 × 2 subarray is equivalent to an 8 × 1 subarray with a half of adjacent element spacing, resulting in good grating-lobe suppression. To achieve stable two-beam radiation with low side lobe over a wide frequency band, specific wideband beam-forming networks with little magnitude and phase imbalances are designed. The diagram of the beam-forming network is plotted in **Fig. 6b**. It consists of two 1-to-2 power dividers, two −45° phase shifters (PSs), two 2 × 4 Butler matrices (BMs) and eight 1-to-3 power dividers. Moreover, the adjacent element spacing is optimized to obtain a stable 10 dB beam width around 120°, thus satisfying the coverage requirement of 120° in the horizontal plane for base station applications. The array exhibits two beams with a stable 10 dB beam width around 120° in the horizontal plane and around −10 dB cross level between two beams. The impedance bandwidth is measured to be 56.1% (1.64 – 2.92 GHz) for voltage standing wave ratio (VSWR) <1.5 and horizontally side-lobe and grating-lobe levels of the two beams are measured to be better than 18 dB.

In Ref. [37], broad band three-beam antenna arrays based on Butler matrices are presented, which are employed to increase the capacity of 3G/LTE base stations. The essential part of the three-beam arrays is a wideband 3 × 3 Butler matrix, which is formed by quadrature couplers and fixed wideband phase shifters. Wideband quadrature and phase shifters are implemented by strip lines. To achieve the suitable beam width and the required crossed level between adjacent beams, beam-forming networks consisting of augmented 3 × 3 Butler matrices and power dividers are proposed to expand the number of output ports from three to five or six, as shown in **Figs. 7a** and **7b** respectively. Dual-polarized, three-beam antenna arrays with five and six elements covering 3G/LTE band are developed with good impedance matching, high isolation between beams, and three-beam radiation in the horizontal plane over the wide frequen-

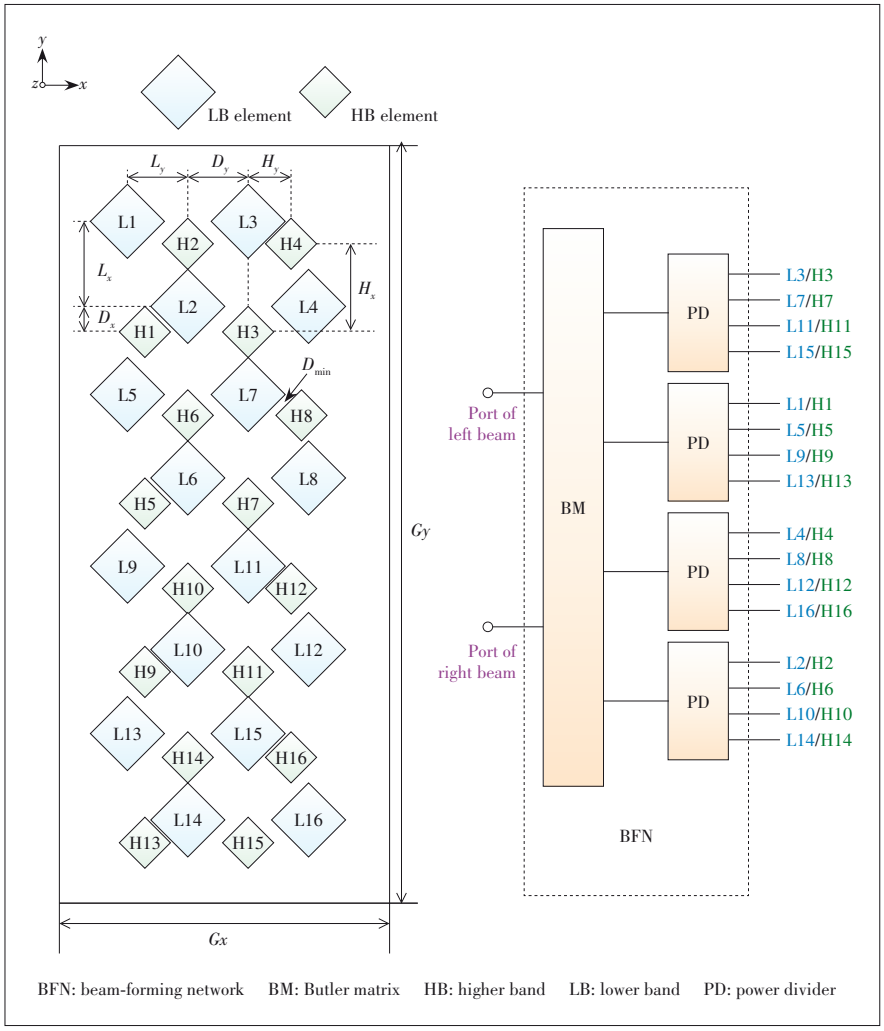

▲ Figure 5. Dual-band two-beam antenna in Ref. [34]. (a) Elements distribution of the interleaved configuration; (b) Beam forming network diagram.

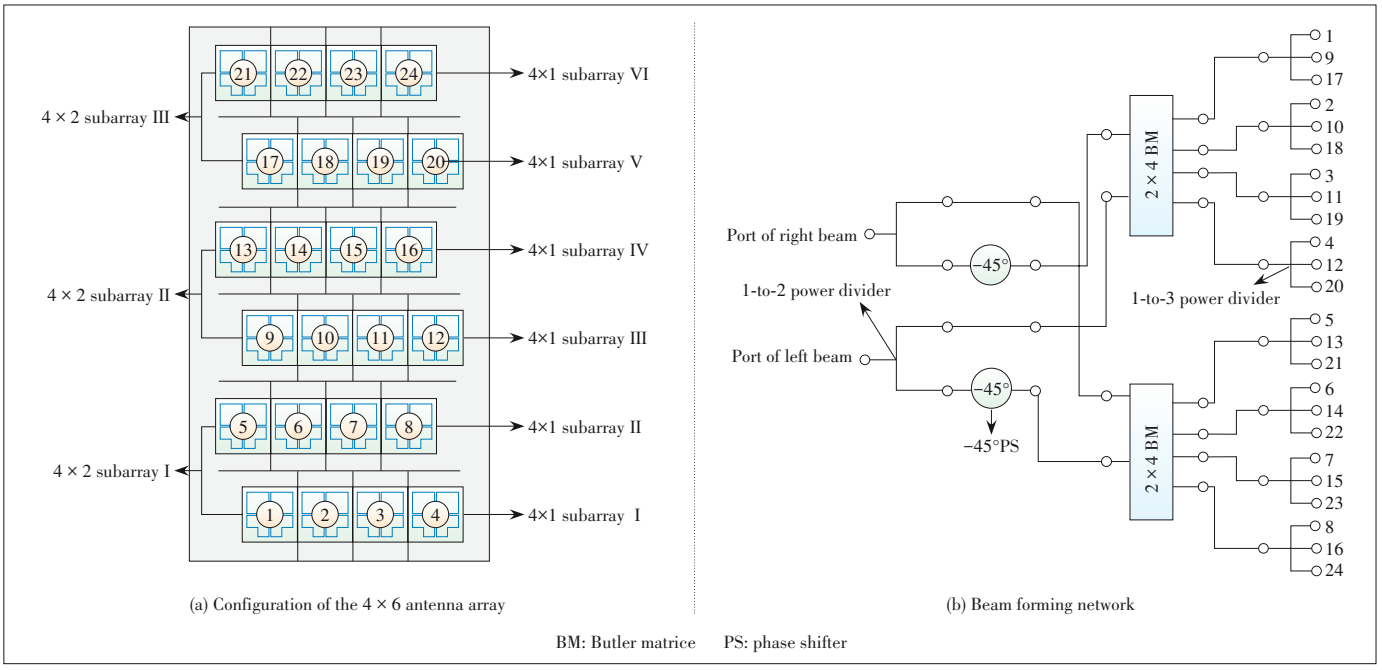

▲Figure 6. Wideband two-beam antenna in Ref. [36].

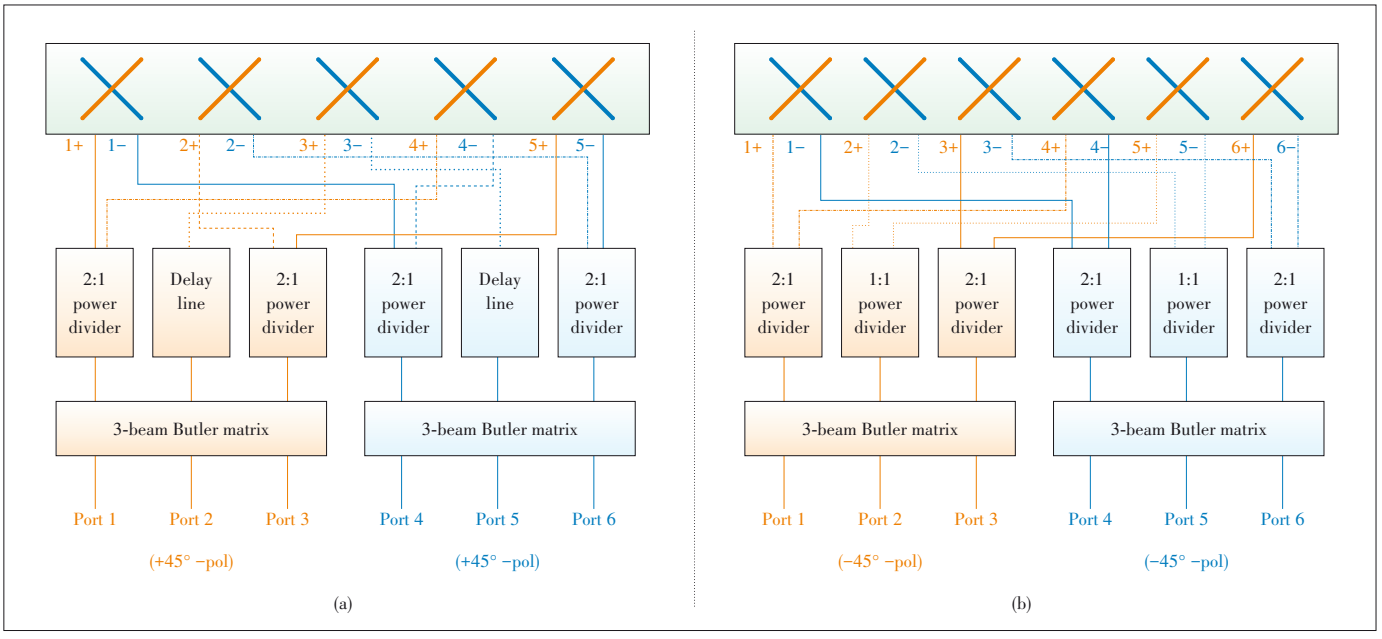

▲Figure 7. Three-beam antennas with (a) five elements and (b) six elements in Ref. [37].

cy band of 1.7 – 2.7 GHz.

In Ref. [38], a compact four-beam slot antenna array fed by a dual-layer 4 × 8 Butler matrix with side lobe level suppression by substrate integrated waveguide technology is proposed. To address the excessive crossovers in the classic 4 × 8 Butler matrix, a novel dual-layer configuration is proposed, which is formed by a 4 × 4 Butler matrix and an amplitude taper, as illustrated in **Fig. 8a.** The 4 × 4 Butler matrix is employed to provide four outputs with equal powers and desired phases, and the amplitude taper is used to convert the four outputs with equal power divisions into eight outputs with unequal power distributions for reducing side lobe level. The proposed topology of the 4 × 8 Butler matrix is employed to reduce the required crossovers from original five sets to merely one set. Therefore, the 4 × 8 Butler matrix can be significantly simplified to achieve better compactness. Finally, a slot antenna array with eight elements is fed by the proposed BM to produce four-beam radiation with low side lobe level, with the

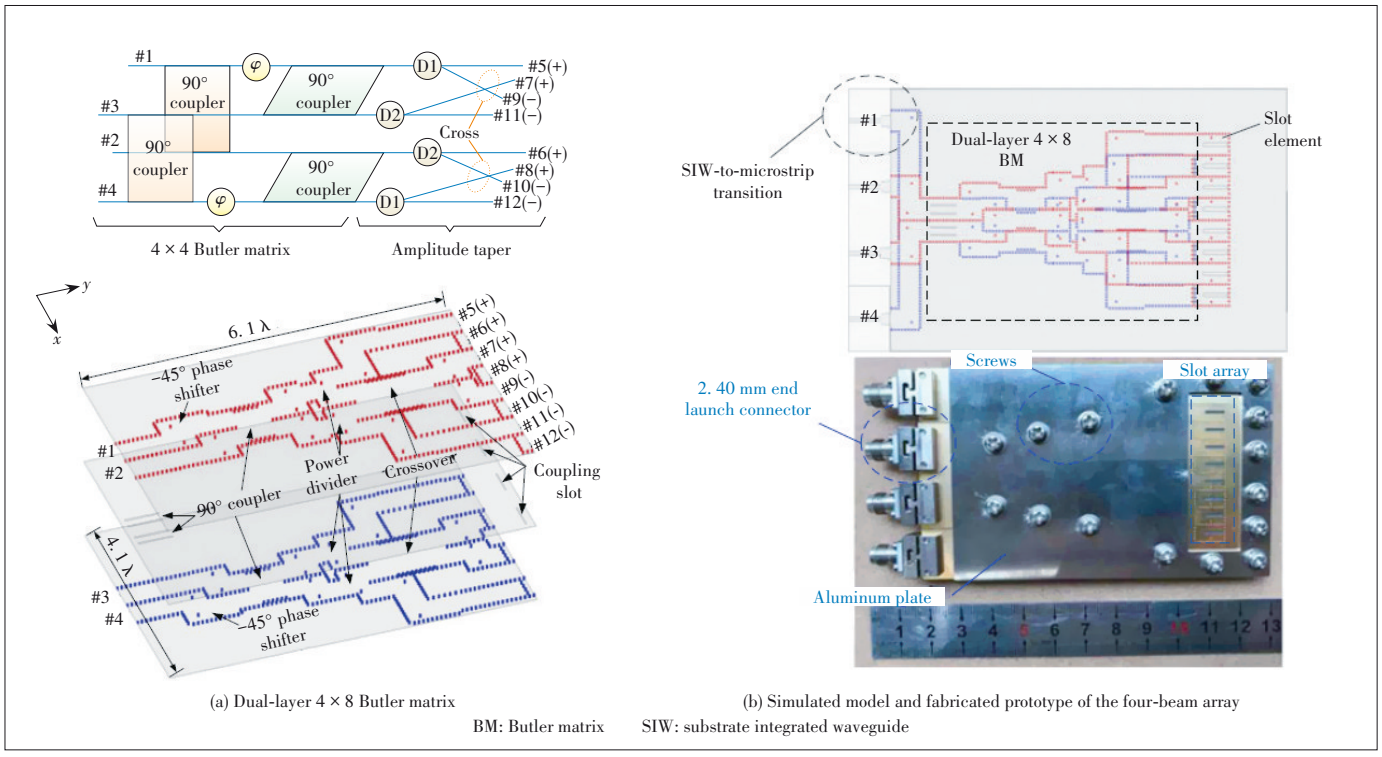

▲**Figure 8. Four-beam array in Ref. [38].**

simulated model and prototype as shown in **Fig. 8b**.

To further increase the communication capacity, a modified topology of a 2D multibeam antenna array[39] fed by a passive beamforming network is proposed by introducing two sets of vertical interconnections into the conventional array configuration. Different from the traditional design, the proposed array structure shown in **Fig. 9** can be integrated into multi-layered planar substrates conveniently, which has advantages of low loss characteristics, ease of realization, and low fabrication cost for millimeter wave applications. A 4 × 4 multibeam antenna array that can generate 16 beams is then designed. The proposed array configuration provides a new means to implement the relatively large size 2D multibeam antenna arrays with planar passive beamforming networks, which would be attractive for future millimeter wave wireless systems used for 5G/B5G communications.

5 Challenges of MABBMs

With the rapid development of mobile communication technology, mobile communication systems are developing towards the trend of broad frequency band, multiple frequency bands, miniaturization, and low cost, which leads to the following challenges for MABBMs.

(1) Design of Wideband or Multi-band MABBMs

In the 5G/B5G era, mobile communication systems such as 2G, 3G, 4G, 5G and B5G will coexist for a long time in the future. In order to comply with the development trend of mobile communication, reduce the number of antennas, and improve the utilization of space resources and spectrum resources, an MABBM is required to cover multiple communication frequen-

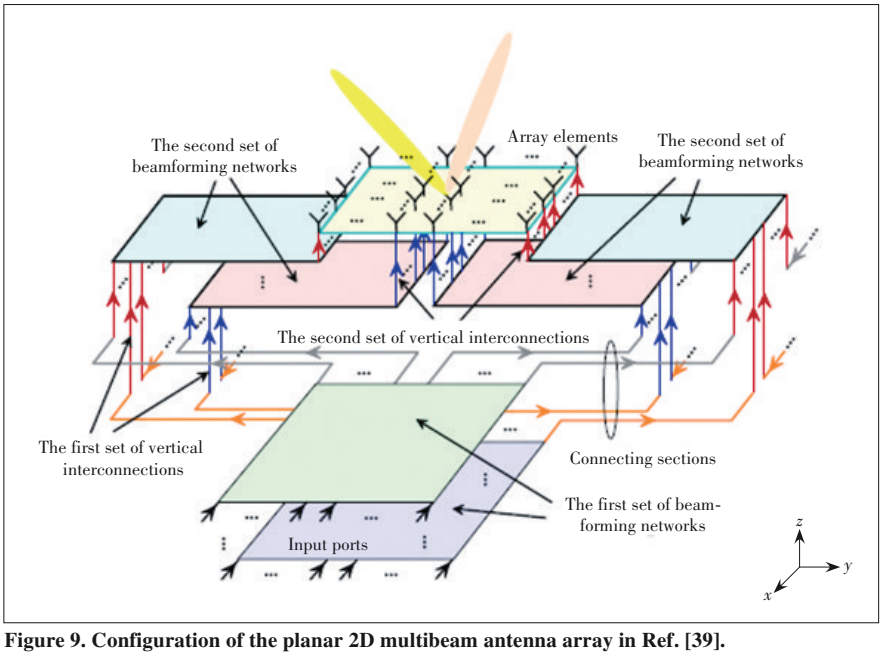

Figure 9. Configuration of the planar 2D multibeam antenna array in Ref. [39].

cy bands. Therefore, a broadband or multi-band MABBM with good impedance matching, high beam isolation, and excellent side lobe suppression is a major challenge.

(2) Miniaturization of MABBMs

Miniaturized MABBMs can not only reduce the spacing of mobile communication system, but also decrease the associated cost. In order to achieve miniaturization of MABBMs, it is necessary to narrow the distance between antenna elements and reduce the size of the Butler matrix. This would introduce strong electromagnetic coupling and radiation interference, causing problems such as deterioration of beam solation and distortion of radiation pattern. Therefore, miniaturization of a MABBM with good electrical performance and radiation performance is another challenge.

6 Conclusions

In summary, the MABBM technologies have been reviewed in this paper. The specifications for base station applications, principles of operation, design and implementation of MABBMs are presented, and the latest research progress on broadband or multi-band MABBMs is analyzed. Even though a few related challenges remain to be solved, the full MABBM is regarded as a promising pathway towards the realization of high-performance 3G/LTE/5G/B5G mobile communication systems.

References

[1] LI M, LI Q L, WANG B, et al. A low-profile dual-polarized dipole antenna using wideband AMC reflector [J]. IEEE transactions on antennas and propagation, 2018, 66(5): 2610 – 2615. DOI:10.1109/tap.2018.2806424
[2] WANG J, WANG W, LIU A M, et al. Cross-polarization suppression of a dual-polarized microstrip antenna using enclosed substrate-integrated cavities [J]. IEEE antennas and wireless propagation letters, 2020, 19(1): 64 – 68. DOI: 10.1109/lawp.2019.2953076
[3] WANG X Y, TANG S C, YANG L L, et al. Differential-fed dual-polarized dielectric patch antenna with gain enhancement based on higher order modes [J]. IEEE antennas and wireless propagation letters, 2020, 19(3): 502 – 506. DOI: 10.1109/lawp.2020.2964569
[4] SAEIDI-MANESH H, SAEEDI S, ZHANG G F. Dual-polarized perpendicularly fed balanced feed antenna with high polarization purity [J]. IEEE antennas and wireless propagation letters, 2020, 19(2): 368 – 372. DOI: 10.1109/lawp.2020.2963958
[5] HUANG H, LI X P, LIU Y M. A low-profile, single-ended and dual-polarized patch antenna for 5G application [J]. IEEE transactions on antennas and propagation, 2020, 68(5): 4048 – 4053. DOI:10.1109/tap.2019.2948743
[6] SUDHAKAR RAO K, MORIN G A, TANG M Q, et al. Development of a 45 GHz multiple-beam antenna for military satellite communications [J]. IEEE transactions on antennas and propagation, 1995, 43(10): 1036 – 1047. DOI: 10.1109/8.467639
[7] EGAMI S. A power-sharing multiple-beam mobile satellite in Ka band [J]. IEEE journal on selected areas in communications, 1999, 17(2): 145 – 152. DOI: 10.1109/49.748778
[8] RAHMAT-SAMII Y, DENSMORE A C. Technology trends and challenges of antennas for satellite communication systems [J]. IEEE transactions on antennas and propagation, 2015, 63(4): 1191 – 1204. DOI:10.1109/tap.2014.2366784
[9] ZHANG Z Y, ZHAO Y R, LIU N W, et al. Design of a dual-beam dual-polarized offset parabolic reflector antenna [J]. IEEE transactions on antennas and propagation, 2019, 67(2): 712 – 718. DOI:10.1109/tap.2018.2882593
[10] CHOU H T, CHOU S J, CHIU C W, et al. Quasi-orthogonal multibeam radiation of reflector antennas for radio coverage of mobile communication at millimeter-wave frequencies [J]. IEEE transactions on antennas and propagation, 2018, 66(11): 6340 – 6345. DOI:10.1109/tap.2018.2861988
[11] MANOOCHEHRI O, DARVAZEHBAN A, SALARI M A, et al. A parallel plate ultra wideband multibeam microwave lens antenna [J]. IEEE transactions on antennas and propagation, 2018, 66(9): 4878 – 4883. DOI: 10.1109/tap.2018.2845548
[12] LIAN J W, BAN Y L, CHEN Z, et al. SIW Folded cassegrain lens for millimeter-wave multibeam application [J]. IEEE antennas and wireless propagation letters, 2018, 17(4): 583 – 586. DOI:10.1109/lawp.2018.2804923
[13] LARIMORE Z, JENSEN S, GOOD A, et al. Additive manufacturing of luneburg lens antennas using space-filling curves and fused filament fabrication [J]. IEEE transactions on antennas and propagation, 2018, 66(6): 2818 – 2827. DOI:10.1109/tap.2018.2823819
[14] MEI Z L, BAI J, NIU T M, et al. A half maxwell fish-eye lens antenna based on gradient-index meta materials [J]. IEEE transactions on antennas and propagation, 2012, 60(1): 398 – 401. DOI:10.1109/tap.2011.2167914
[15] HUANG M, YANG S W, GAO F, et al. A 2-D multibeam half maxwell fish-eye lens antenna using high impedance surfaces [J]. IEEE antennas and wireless propagation letters, 2014, 13: 365 – 368. DOI:10.1109/lawp.2014.2306207
[16] KWON D H, WERNER D H. Beam scanning using flat transformation electromagnetic focusing lenses [J]. IEEE antennas and wireless propagation letters, 2009, 8: 1115 – 1118. DOI:10.1109/lawp.2009.2033619
[17] JIANG Z H, GREGORY M D, WERNER D H. Broadband high directivity multibeam emission through transformation optics-enabled metamaterial lenses [J]. IEEE transactions on antennas and propagation, 2012, 60(11): 5063 – 5074. DOI:10.1109/tap.2012.2207685
[18] WU Q, HIROKAWA J, YIN J X, et al. Millimeter-wave multibeam end fire dual-circularly polarized antenna array for 5g wireless applications [J]. IEEE transactions on antennas and propagation, 2018, 66(9): 4930 – 4935. DOI: 10.1109/tap.2018.2851667
[19] LI Y J, WANG J H, LUK K M. Millimeter-wave multibeam aperture-coupled magnetoelectric dipole array with planar substrate integrated beamforming network for 5G applications [J]. IEEE transactions on antennas and propagation, 2017, 65(12): 6422 – 6431. DOI:10.1109/tap.2017.2681429
[20] KIM D H, HIROKAWA J, ANDO M. Design of waveguide short-slot two-plane couplers for one-body 2-D beam-switching butler matrix application [J]. IEEE transactions on microwave theory and techniques, 2016: 1 – 9. DOI:10.1109/tmtt.2016.2515605
[21] ZHONG L H, BAN Y L, LIAN J W, et al. Miniaturized SIW multibeam antenna array fed by dual-layer 8 × 8 Butler matrix [J]. IEEE antennas and wireless propagation letters, 2017, 16: 3018 – 3021. DOI:10.1109/lawp.2017.2758373
[22] LIAO W J, TUAN S K, LEE Y, et al. A Diversity receiver-based high-gain broad-beam reception array antenna [J]. IEEE antennas and wireless propagation letters, 2018, 17(3): 410 – 413. DOI:10.1109/lawp.2018.2792438
[23] WINCZA K, STASZEK K, GRUSZCZYNSKI S. Broadband multibeam antenna arrays fed by frequency-dependent butler matrices [J]. IEEE transactions on antennas and propagation, 2017, 65(9): 4539 – 4547. DOI: 10.1109/tap.2017.2722823
[24] HONG W, JIANG Z H, YU C, et al. Multibeam antenna technologies for 5G wireless communications [J]. IEEE transactions on antennas and propagation, 2017, 65(12): 6231 – 6249. DOI:10.1109/tap.2017.2712819
[25] WANG Y Q, MA K X, JIAN Z. A low-loss Butler matrix using patch element and honeycomb concept on SISL platform [J]. IEEE transactions on microwave theory and techniques, 2018, 66(8): 3622 – 3631. DOI: 10.1109/tmtt.2018.2845868
[26] DING K J, KISHK A A. 2D Butler matrix and phase-shifter group [J]. IEEE transactions on microwave theory and techniques, 2018, 66(12): 5554 – 5562. DOI:10.1109/tmtt.2018.2879013
[27] DYAB W M, SAKR A A, WU K. Dually-polarized Butler matrix for base stations with polarization diversity [J]. IEEE transactions on microwave theory and techniques, 2018, 66(12): 5543 – 5553. DOI:10.1109/tmtt.2018.2880786

[28] BALANIS C A. Antenna theory: analysis and design [M]. Hoboken, USA: Wiley, 1996
[29] TAJIK A, SHAFIEI ALAVIJEH A, FAKHARZADEH M. Asymmetrical 4 × 4 Butler matrix and its application for single layer 8 × 8 Butler matrix [J]. IEEE transactions on antennas and propagation, 2019, 67(8): 5372 – 5379. DOI: 10.1109/tap.2019.2916695
[30] SHAO Q, CHEN F C, WANG Y, et al. Design of modified 4 × 6 filtering butler matrix based on all-resonator structures [J]. IEEE transactions on microwave theory and techniques, 2019, 67(9): 3617 – 3627. DOI: 10.1109/tmtt.2019.2925113
[31] LIAN J W, BAN Y L, YANG Q L, et al. Planar millimeter-wave 2D beam-scanning multibeam array antenna fed by compact SIW beam-forming network [J]. IEEE transactions on antennas and propagation, 2018, 66(3): 1299 – 1310. DOI:10.1109/tap.2018.2797873
[32] LI Y J, LUK K M. 60-GHz dual-polarized two-dimensional switch-beam wideband antenna array of aperture-coupled magneto-electric dipoles [J]. IEEE transactions on antennas and propagation, 2016, 64(2): 554 – 563. DOI: 10.1109/tap.2015.2507170
[33] KIM D H, HIROKAWA J, ANDO M. Design of waveguide short-slot two-plane couplers for one-body 2D beam-switching Butler matrix application [J]. IEEE transactions on microwave theory and techniques, 2016: 1 – 9. DOI:10.1109/tmtt.2016.2515605
[34] ZHANG X Y, XUE D, YE L H, et al. Compact dual-band dual-polarized interleaved two-beam array with stable radiation pattern based on filtering elements [J]. IEEE transactions on antennas and propagation, 2017, 65(9): 4566 – 4575. DOI:10.1109/tap.2017.2723914
[35] DUAN W, ZHANG X Y, PAN Y M, et al. Dual-polarized filtering antenna with high selectivity and low cross polarization [J]. IEEE transactions on antennas and propagation, 2016, 64(10): 4188 – 4196. DOI:10.1109/tap.2016.2594818
[36] YE L H, ZHANG X Y, GAO Y, et al. Wideband dual-polarized two-beam antenna array with low sidelobe and grating-lobe levels for base-station applications [J]. IEEE transactions on antennas and propagation, 2019, 67(8): 5334 – 5343. DOI:10.1109/tap.2019.2913795
[37] ZHU H, SUN H H, JONES B, et al. Wideband dual-polarized multiple beamforming antenna arrays [J]. IEEE transactions on antennas and propagation, 2019, 67(3): 1590 – 1604. DOI:10.1109/tap.2018.2888728
[38] LIAN J W, BAN Y L, XIAO C H, et al. Compact substrate-integrated 4 × 8 Butler matrix with sidelobe suppression for millimeter-wave multibeam application [J]. IEEE antennas and wireless propagation letters, 2018, 17(5): 928 – 932. DOI:10.1109/lawp.2018.2825367
[39] LI Y J, WANG J H, LUK K M. Millimeter-wave multibeam aperture-coupled magnetoelectric dipole array with planar substrate integrated beamforming network for 5G applications [J]. IEEE transactions on antennas and propagation, 2017, 65(12): 6422 – 6431. DOI:10.1109/tap.2017.2681429

Biographies

YE Lianghua (lianghuaye@gdut.edu.cn) received the B.S. degree in electronics and information engineering from Shandong University of Science and Technology, China in 2007, the M.S. degree in electronic and information engineering from South China University of Technology (SCUT), China in 2010. He is currently pursuing the Ph. D. degree with the School of Electronic and Information Engineering, SCUT. He is currently a full lecturer with the School of Physics and Optoelectronic Engineering, Guangdong University of Technology. His current research interests include wide band antennas, multiband antennas, and base station antennas.

CAO Yunfei received the B.E. degree in information engineering from South China University of Technology (SCUT), China in 2012, and the Ph.D. degree in electrical and electronic engineering from the University of Hong Kong, China in 2016. He is currently the Associate Research Fellow in the School of Electronic and Information Engineering of SCUT. He was a recipient of the Pearl River Talent Support Program for postdoctoral fellows. His current research interests include massive MIMO antenna, filtering antenna, reconfigurable antenna, and wearable antenna.

ZHANG Xiuyin received the B.S. degree in communication engineering from Chongqing University of Posts and Telecommunications, China in 2001, the M.S. degree in electronic engineering from South China University of Technology, China in 2006, and the Ph.D. degree in electronic engineering from City University of Hong Kong, China in 2009. He is currently a full professor and vice dean with the School of Electronic and Information Engineering, South China University of Technology. He has authored or coauthored more than 100 internationally referred journal papers including 70 IEEE Transactions. His research interests include microwave circuits and sub-systems, antennas and arrays. He has served as a Technical Program Committee (TPC) chair or member for a number of conferences. He was a recipient of the National Science Foundation for Distinguished Young Scholars of China and the Young Scholar of the Changjiang Scholars Program of Chinese Ministry of Education.

A Novel 28 GHz Phased Array Antenna for 5G Mobile Communications

LI Yezhen[1], REN Yongli[1], YANG Fan[1], XU Shenheng[1], ZHANG Jiannian[2]

(1. Department of Electronic Engineering, Tsinghua University, Beijing 100084, China;
2. Beijing Actenna Technology Co., Ltd., Beijing 100089, China)

Abstract: A novel phased array antenna consisting of 256 elements is presented and experimentally verified for 5G millimeter-wave wireless communications. The antenna integrated with a wave control circuit can perform real-time beam scanning by reconfiguring the phase of an antenna unit. The unit, designed at 28 GHz using a simple patch structure with one PIN diode, can be electronically controlled to generate 1 bit phase quantization. A prototype of the antenna is fabricated and measured to demonstrate the feasibility of this approach. The measurement results indicate that the antenna achieves high gain and fast beam-steering, with the scan beams within ±60° range and the maximum gain up to 21.7 dBi. Furthermore, it is also tested for wireless video transmission. In ZTE Shanghai, the antenna was used for the 5G New Radio (NR) test. The error vector magnitude (EVM) is less than 3% and the adjacent channel leakage ratio (ACLR) less than −35 dBc, which can meet 5G system requirements. Compared with the conventional phased array antenna, the proposed phased array has the advantages of low power consumption, low cost and conformal geometry. Due to these characteristics, the antenna is promising for wide applications in 5G millimeter-wave communication systems.

Keywords: 5G mobile communications; millimeter wave; phased array antenna

DOI: 10.12142/ZTECOM.202003004

https://kns.cnki.net/kcms/detail/34.1294.TN.20200908.1108.004.html, published online September 10, 2020

Manuscript received: 2020-07-16

Citation (IEEE Format): Y. Z. Li, Y. L. Ren, F. Yang, et al., "A novel 28 GHz phased array antenna for 5G mobile communications," *ZTE Communications*, vol. 18, no. 3, pp. 20 – 25, Sept. 2020. doi: 10.12142/ZTECOM.202003004.

1 Introduction

5G wireless communication systems are actively tested and deployed worldwide now. They are supposed to enable extremely fast communication speed of up to 10 Gbit/s[1 – 2]. Compared with 1G to 4G wireless communications, 5G systems are mostly concerned with the channel capacity, power consumption, and system cost. They provide multiple application scenarios, such as enhanced mobile broadband (eMBB), ultra-reliable and low-latency communications (uRLLC), and massive machine type communications (mMTC). 5G will affect every aspect of our lives, implementing the virtual reality (VR), Internet of Things (IoT), smart home, and so on. A lot of challenges need to be overcome to realize the above goals, including those in the transmission network.

Antennas are critical components in 5G wireless transmission networks[3]. While a lot of efforts have been devoted to antenna designs in mobile devices, here we focus on antennas on base stations. Gain and coverage are two critical requirements for base station antennas; however, they contradict each other: a higher gain results in a narrower beamwidth and hence a limited coverage area. To solve this problem, multiple beams and

beam scanning techniques, usually realized by phase array antennas, provide a feasible solution.

This paper presents a novel phased array antenna operating at 28 GHz for 5G wireless communications. The phased array design method is introduced first, and the element and array configuration are discussed next. The measured results of the antenna array and the communication test of 1 transmitter-1 reciever (1T-1R) and 1 transmitter-2 recievers (1T-2R) systems are presented to demonstrate the promising potential of the proposed mm-wave phased array for 5G systems. In addition, the antenna was used for the 5G NR test of ZTE Shanghai, which shows good performance in the error vector magnitude (EVM) and adjacent channel leakage ratio (ACLR).

2 Design Methods for Phased Arrays

To achieve the beam scanning capability in an antenna array, the excitation phase of each element needs to be tunable in order to form a coherent phase front at the desired beam direction. As shown in **Fig. 1**, the phase control method is the key point in the design of phased arrays and two different methods can achieve phased arrays.

The major trend in phased array development is based on the microwave and millimeter-wave integrated circuit (MMIC) technology. The phase control function is realized from the antenna element "downward" and a representative device is a transmit/receive module connected to each element. This circuit approach has a lot of advantages, such as excellent radiation performance and flexible radiation beam; however, the power efficiency, antenna weight, and system cost are major concerns, especially for those large-scale and high-frequency phased arrays.

A novel alternative approach is to move the phase control function "upward" from antenna element and an example is a reconfigurable reflective surface. As shown in **Fig. 2**, when electromagnetic wave impinges on this surface, an additional reflection phase is added upon reflection, which can be tuned by active components such as PIN diodes and varactor diodes. In this field approach, both "radiation" and "phase control" functions are integrated onto the surface. This new approach has attracted growing interests because of its high efficiency, conformal geometry, feasibility for millimeter-wave and tera hertz operation, and low system cost.

The phased array using the field approach consists of three major components: a reconfigurable surface, a control module,

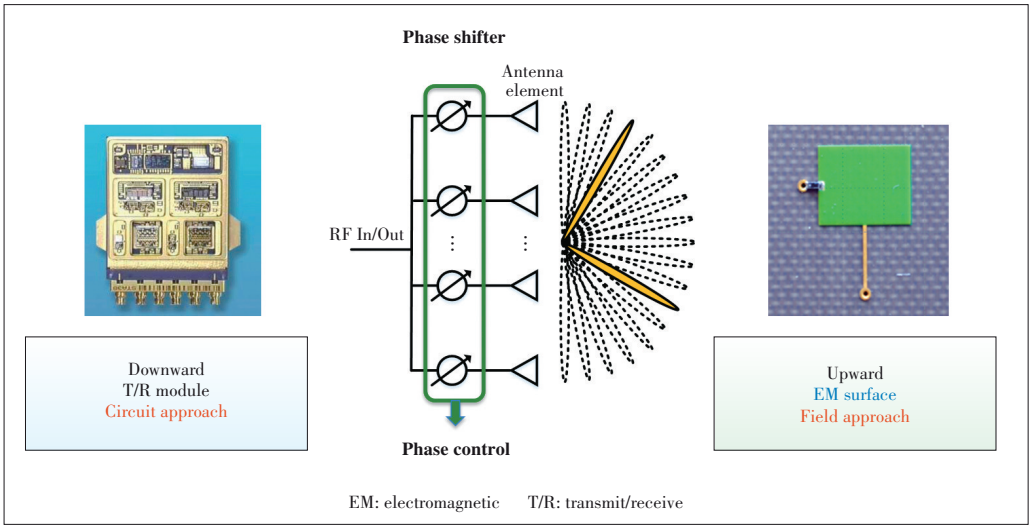

▲ **Figure 1. Design approaches for phased array antennas: circuit approach using T/R modules and field approach using reconfigurable electromagnetic surfaces.**

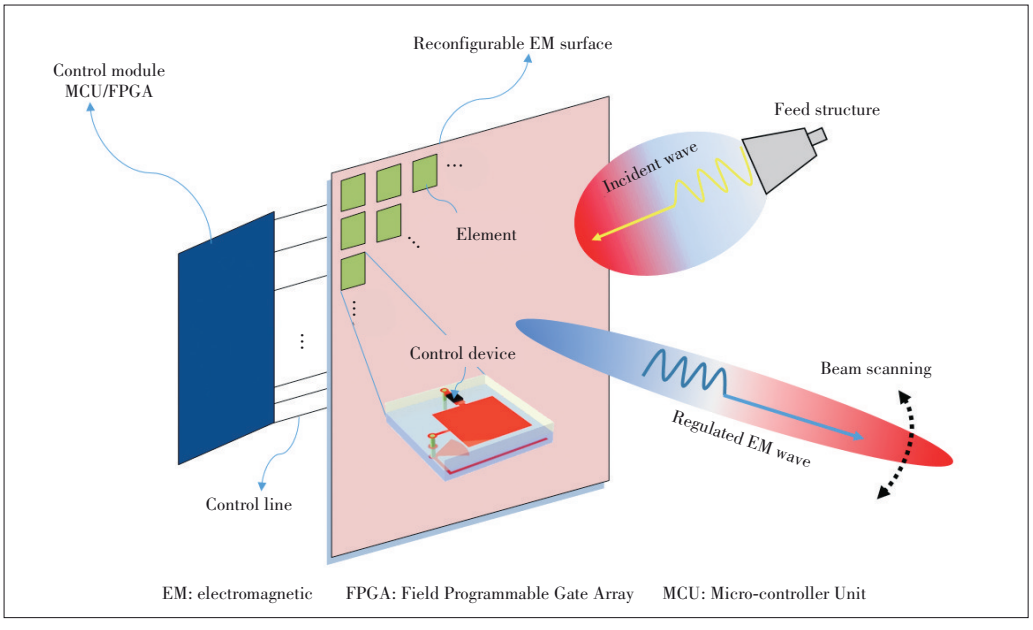

▲ **Figure 2. Structure of the novel phased array antenna.**

and a feeding structure[4 – 6]. An array of patch elements are arranged on the surface, and each element is integrated with control devices, such as PIN diodes, varactor diodes, MEMS switches and mechanic actuators. The statuses of these devices are determined by a control module, usually a Micro-controller Unit (MCU) or a Field Programmable Gate Array (FPGA) board. To transmit/receive wave to/from the surface, a feed structure is necessary, which can be a horn in the far field[7], a passive array in the near field, or even a constrained feed network connected to the surface, as shown in **Fig. 3**.

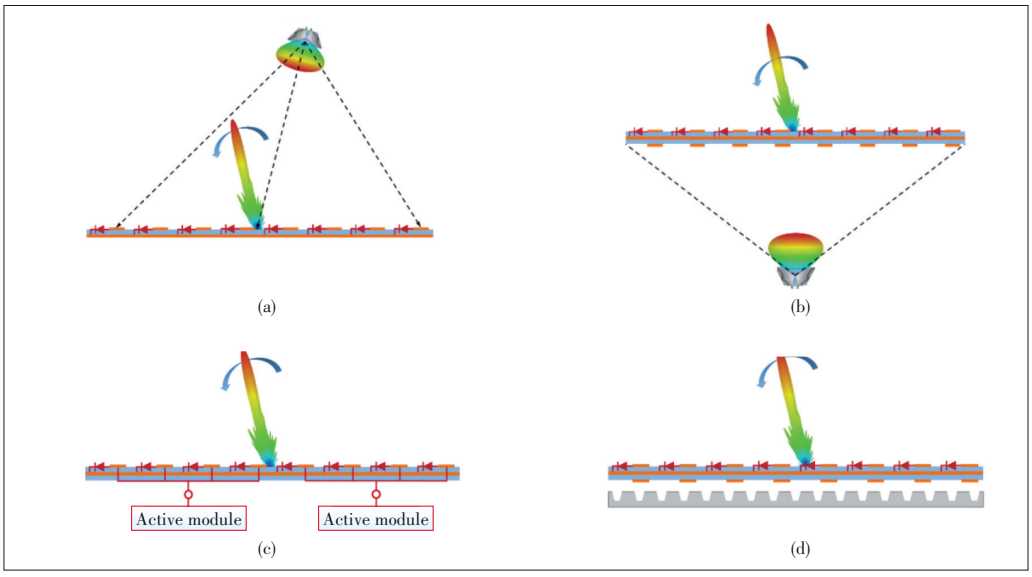

▲ **Figure 3. Various structures of reconfigurable EM surface: (a) reflectarray with horn antenna; (b) transmitarray with horn antenna; (c) transmitarray with active module; (d) transmitarray with coupling network.**

3 A Novel Mm-Wave Phased Array Antenna Design and Measurement

3.1 Electromagnetic Surface Element

A phased electromagnetic surface antenna operating at 28 GHz for 5G millimeter-wave communications is designed and tested. The element geometry, array configuration, and measurement results for both the antenna radiation and system throughput are presented in this section.

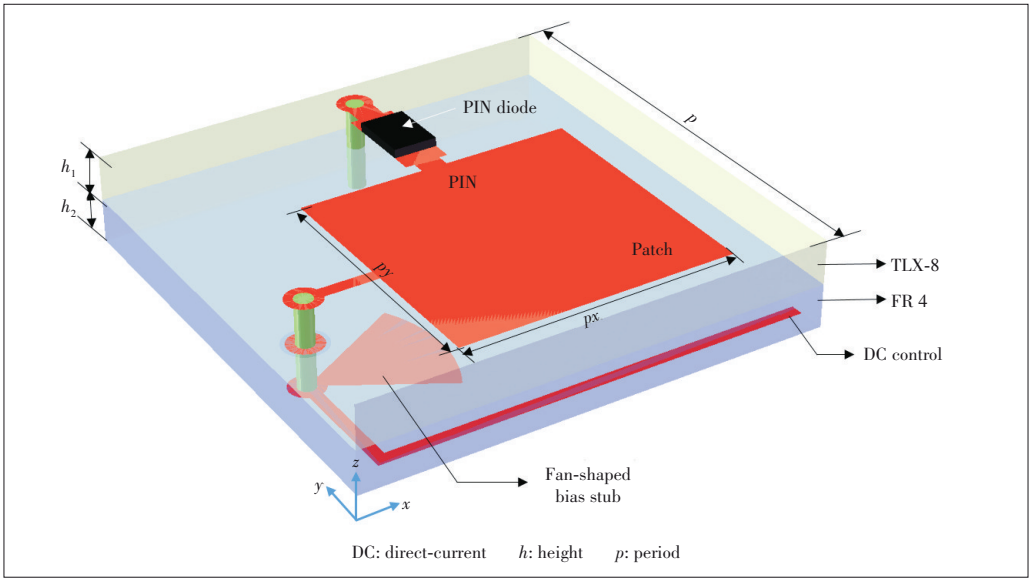

▲ **Figure 4. Geometry of a reconfigurable element designed at 28 GHz: p=5.35 mm; px=3.15 mm; py=3.025 mm; h_1=0.508 mm; h_2=0.500 mm.**

Fig. 4 shows the geometry of a reconfigurable element, which consists of a patch layer, a ground layer, and a biasing line layer. A PIN diode is connected to the patch to control its reflection phase at 28 GHz. One side of the PIN diode is grounded directly, and the other side is connected to a DC biasing voltage through the patch and the biasing line. A fan-shaped stub is used to isolate the DC and RF interference. The element dimensions are listed in the caption of Fig. 4 and the element is carefully designed to obtain a 180° phase difference between PIN On-Off statuses at 28 GHz. Moreover, the reflection loss of the element is less than 1 dB at 28 GHz, as shown in **Fig. 5**.

3.2 Phased Array Antenna Design

Based on element design and simulation, a phased array consisting of 16 × 16 patch elements is designed. In space-fed array designs, the reconfigurable reflective surface is usually placed in the far-field region of the feed. The magnitude of incident wave on the surface is related to the radiation pattern of feed, as well as the spatial distance between the feed and each element.

In this paper, a horn antenna is designed as the feed. The −10 dB beam width of the feed is ±30°, so the chosen distance between the phase center of feed horn and the reflective surface is 66 mm to balance spillover efficiency and illumination efficiency.

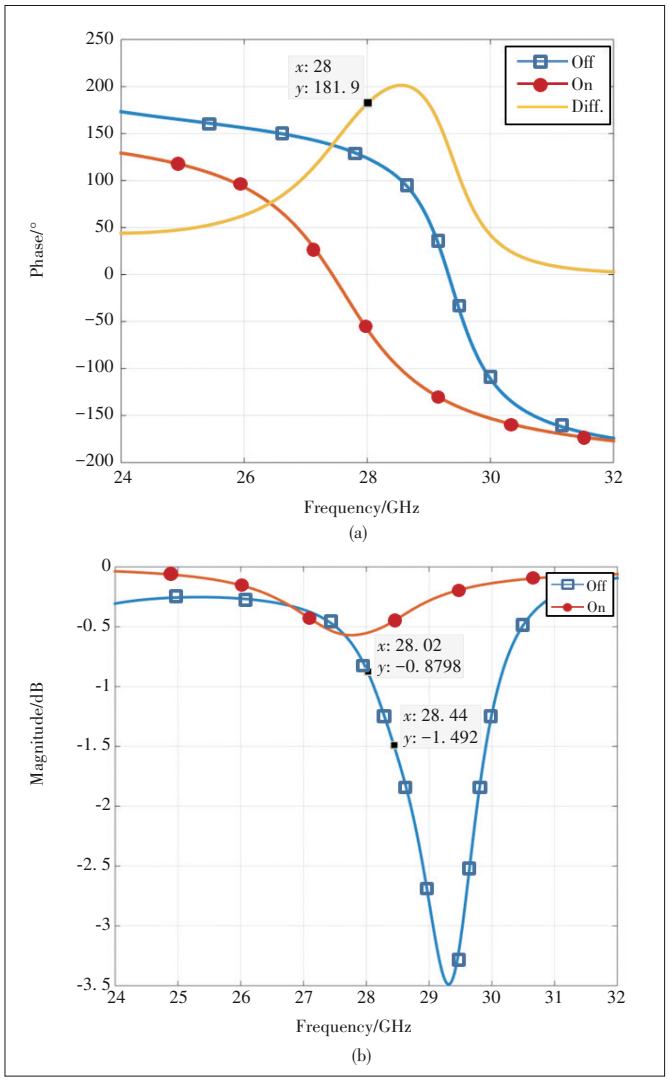

▲ **Figure 5. Simulated results of element: (a) phase result; (b) magnitude result.**

For a reconfigurable reflective surface, the required compensation phase ϕ_{rmn} for the (m, n)th element is computed by

$$\phi_{rmn} = \phi_{imn} - k \times \widehat{u_0} \times \overrightarrow{r_{mn}} + \Delta\phi, \quad (1)$$

where ϕ_{imn} is the incident phase of the (m, n)th element, k is the free space wavenumber, $\widehat{u_0}$ is the unit vector in the main beam direction, $\overrightarrow{r_{mn}}$ is the position vector of the (m, n)th element, and $\Delta\phi$ is an additional optimized phase[8]. If we use reconfigurable elements with 360° full-phase coverage, the required compensation phase for each element will be continuous. For a 1 bit phased array, there are only two-phase states for each element and they are controlled by PIN On or Off. Therefore, the required compensation phase should be quantized. As simulated in Fig. 5 at 28 GHz, PIN Off means 130° and PIN ON means −50°. We use Eq. (2) to quantize the continuous phase into 1 bit compensation phase.

$$\phi_{rmn\_quantized} = \begin{cases} 130^\circ, \phi_{rmn\_continous} \in [40^\circ, 220^\circ) \\ -50^\circ, \phi_{rmn\_continous} \in \text{others} \end{cases}. \quad (2)$$

The phase distribution on the electromagnetic reflective surface of the boresight beam is calculated, **Fig. 6a** shows the continuous compensation phase and **Fig. 6b** shows the quantized phase.

3.3 Phased Array Antenna Measurement

A phased array antenna prototype is built (**Fig. 7**). It consists of 256 patch elements and each is individually controlled by an FPGA board behind the array surface. A horn antenna is designed as the feed for this antenna and the waveguide structure minimizes the feed loss.

The antenna prototype is measured in an anechoic chamber at Tsinghua University. **Fig. 8a** shows the measured patterns at representative scanning angles: 0°, 15°, 30°, 45° and 60°,

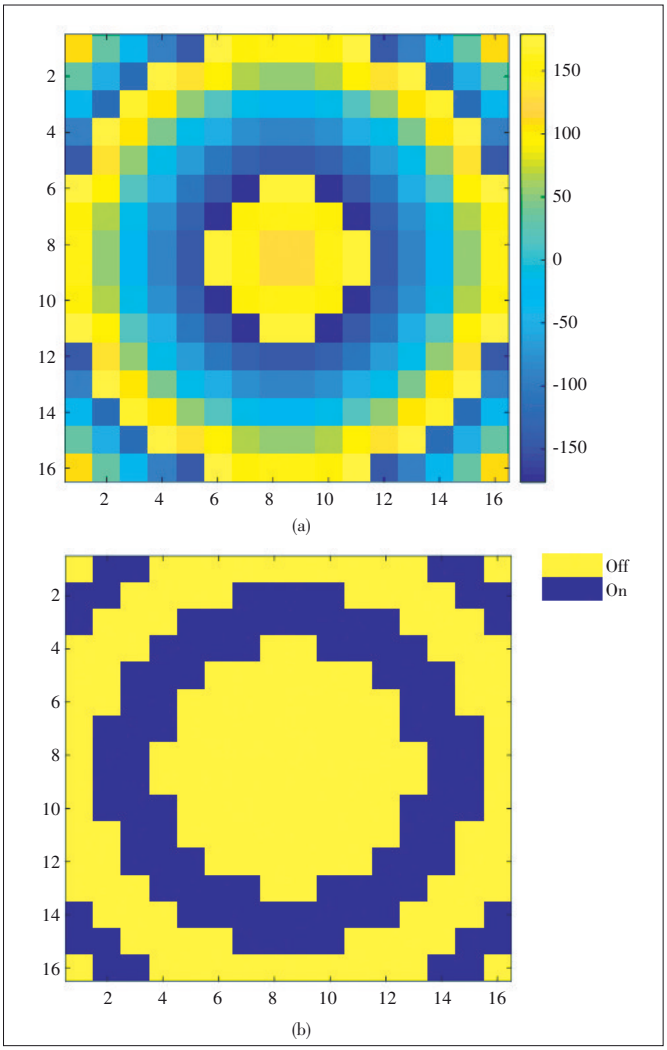

▲ **Figure 6. Boresight beam phase distribution on the electromagnetic reflective surface: (a) continuous phase distribution; (b) 1 bit quantized phase distribution.**

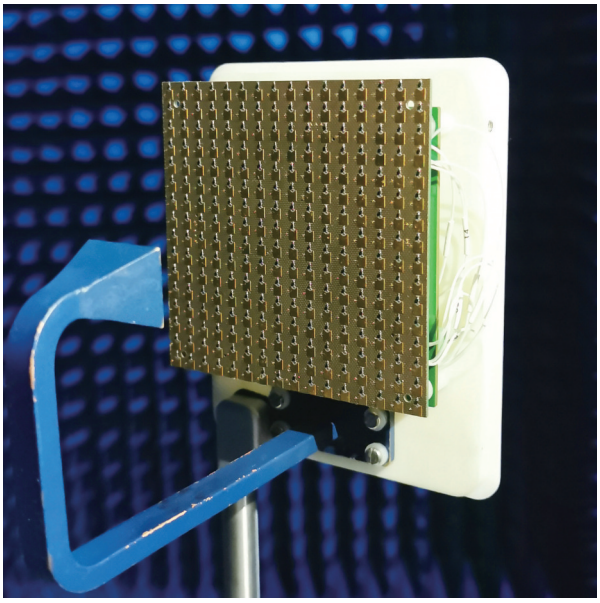

▲Figure 7. Photo of a 256-element phased array prototype for 5G mm-Wave communications.

and **Fig. 8b** shows the measured gains of different scanning beams. It is observed that by reconfiguring the elements' statuses on the surface, the antenna beam can be scanned to the desired direction. In addition, the antenna is also measured from 27 GHz to 29 GHz, which shows the −3 dB gain-bandwidth of the phased array.

After measuring the phased array antenna, a wireless communication system is also built. A National Instrument (NI) millimeter-wave transceiver works at 28 GHz with a bandwidth of 800 MHz. We use 64 Quadrature Amplitude Modulation (64QAM) modulation cooperating with 7/8 turbo coding to build two test scenarios for video data transmission: 1T-1R and 1T-2R. The phased array produces one switching beam for the 1T-1R test and dual beams for the 1T-2R test. The bit rate of both scenarios can achieve up to 2.87 bit/s when the distance between transmitter and reciever(s) is 6 m.

3.4 5G NR Measurement

In order to verify the communication performance of the phased array in mm-Wave band, 5G NR measurement was conducted in the chamber of ZTE Shanghai. **Fig. 9** shows the connections of NR test system.

As depicted in Fig. 9, the phased array acts as the transmitter antenna, and the horn antenna connected with the spectrum analyzer acts as a receiver antenna. The EVM and ACLR were measured by this system. EVM is usually used as a mark to measure the linear performance of transmitter, as well as the transmitter antenna. ACLR indicates interference of transmission signal leakage to the same or similar communication system. After tested by the ZTE 5G NR system, the EVM and

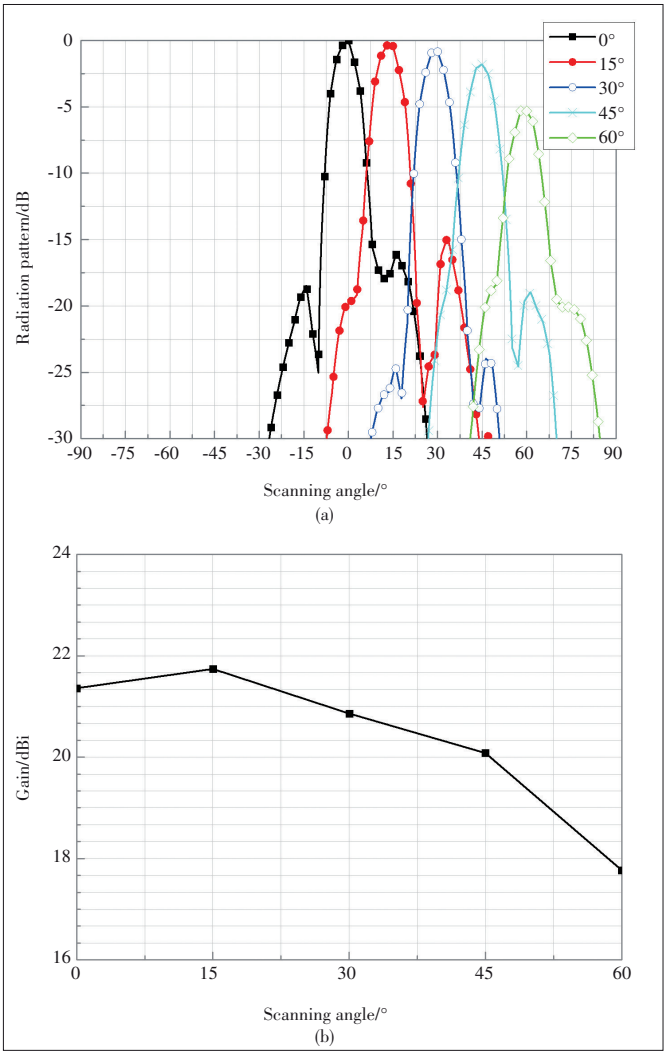

▲Figure 8. Measured results of the 256-element phased array: (a) beam scanning measurement at 28 GHz; (b) gain measurement at 28 GHz.

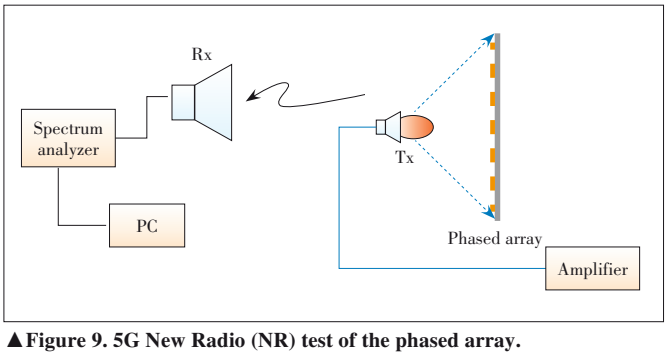

▲Figure 9. 5G New Radio (NR) test of the phased array.

ACLR indices (**Tables 1** and **2**) show that the antenna can be used in 5G wireless communications, and it provides comparable performance to the existing products of ZTE.

4 Conclusions

The demand of phased array antennas for 5G millimeter-

▼Table 1. EVM measurement results

Frequency/GHz	EVM/64QAM
27.05	2.97%
27.85	3.2%
28.15	2.5%
28.95	3%

64QAM: 64 Quadrature Amplitude Modulation EVM: error vector magnitude

▼Table 2. ACLR measurement results

Frequency/GHz	Flatness/dB	ACLR/dBc
27.2	0.78	−35.13
28	0.93	−35.8
28.8	2.4	−35.16

ACLR: adjacent channel leakage ratio

wave wireless communications has been increasing in recent years. This paper introduces a novel phased array approach using reconfigurable electromagnetic surface, which shows good performance in wireless fast data transmission. A 1 bit 256-element phased array operating at 28 GHz band is thoroughly investigated with measurements. The measured beams can scan ±60° and the maximum gain achieves up to 21.7 dBi. The array also achieves dual beams for 1T-2R wireless video transmission successfully. In addition, the array was tested for 5G NR system successfully and the EVM and ACLR indices also show good performance. Because the array only uses PIN diodes to control beam scanning, the power consumption is very low when it provides comparable performance to conventional phased arrays. The measured results show that the phased array is suitable for base stations and have a promising future for 5G millimeter-wave communication systems.

References

[1] MAHMOUD K R, MONTASER A M. Synthesis of multi-polarised upside conical frustum array antenna for 5G mm-wave base station at 28/38 GHz [J]. IET microwaves antennas & propagation, 2018, 12(9): 1559 – 1569. DOI: 10.1049/iet-map.2017.1138
[2] MALLAT N K, ISHTIAQ M, REHMAN AUR, et al. Millimeter-wave in the face of 5G communication potential applications [J]. IETE journal of research, 2020: 1 – 9. DOI: 10.1080/03772063.2020.1714489
[3] BASAR E, DI RENZO M, DE ROSNY J, et al. Wireless communications through reconfigurable intelligent surfaces [J]. IEEE access, 2019: 116753 – 116773. DOI: 10.1109/ACCESS.2019.2935192
[4] YANG H H, YANG F, CAO X Y, et al. A 1600-element dual-frequency electronically reconfigurable reflectarray at x/ku-band [J]. IEEE transactions on antennas and propagation, 2017, 65(6): 3024 – 3032. DOI: 10.1109/TAP.2017.2694703
[5] HUM S V, PERRUISSEAU-CARRIER J. Reconfigurable reflectarrays and array lenses for dynamic antenna beam control: a review [J]. IEEE transactions on antennas and propagation, 2014, 62(1): 183 – 198. DOI: 10.1109/TAP.2013.2287296
[6] NAYERI P, YANG F, ELSHERBENI A Z. Beam-scanning reflectarray antennas: a technical overview and state of the art [J]. IEEE antennas and propagation magazine, 2015, 57(4): 32 – 47. DOI: 10.1109/MAP.2015.2453883
[7] WANG M, XU S H, YANG F, et al. Design and measurement of a 1-bit reconfigurable transmitarray with subwavelength H-shaped coupling slot elements [J]. IEEE transactions on antennas and propagation, 2019, 67(5): 3500 – 3504. DOI: 10.1109/TAP.2019.2902676
[8] YANG H H, YANG F, XU S H, et al. A 1-bit 10×10 reconfigurable reflectarray antenna: design, optimization, and experiment [J]. IEEE transactions on antennas and propagation, 2016, 64(6): 2246 – 2254. DOI: 10.1109/TAP.2016.2550178

Biographies

LI Yezhen received the M.S. degree from Shanghai Jiao Tong University, China in 2016. In 2017, he joined the Department of Electronic Engineering, Tsinghua University, as an engineer. His current research interests include microstrip antenna design, reflectarray and microwave circuits.

REN Yongli received the M.S. degree from University of Electronic Science and Technology of China, China in 2014. In 2018, he joined the Department of Electronic Engineering, Tsinghua University, as an engineer. Her current research interests include reflectarray design, microwave and THz circuits.

YANG Fan (fan_yang@mail.tsinghua.edu.cn) received the B.S. and M.S. degrees from Tsinghua University, China and the Ph.D. degree from the University of California at Los Angeles (UCLA), USA. He joined the Electrical Engineering Department, University of Mississippi, USA, as an assistant professor and was promoted to an associate professor in 2009. In 2011, he joined the Electronic Engineering Department, Tsinghua University, as a professor. He has authored or coauthored more than 300 journal articles and conference articles, six book chapters, and five books. Dr. YANG is an ACES Fellow, IEEE Fellow, and a recipient of several prestigious awards and recognition, including the Young Scientist Awards of the 2005 URSI General Assembly and of the 2007 International Symposium on Electromagnetic Theory, the 2008 Junior Faculty Research Award of the University of Mississippi, the 2009 Inaugural IEEE Donald G. Dudley Jr. Undergraduate Teaching Award, and the 2011 Recipient of Global Experts Program of China. He was the Technical Program Committee (TPC) Chair of 2014 IEEE International Symposium on Antennas and Propagation and USNC-URSI Radio Science Meeting. He is also an IEEE APS Distinguished Lecturer from 2018 to 2020. His current research interests include antennas, surface electromagnetics, computational electromagnetics and applied electromagnetic systems.

XU Shenheng received the B.S. and M.S. degrees from Southeast University, China in 2001 and 2004, respectively and the Ph.D. degree in electrical engineering from the University of California at Los Angeles (UCLA), USA in 2009. From 2000 to 2004, he was a research assistant with the State Key Laboratory of Millimeter Waves, Southeast University, China. From 2004 to 2011, he was a graduate student researcher and then became a post-doctoral researcher with the Antenna Research, Analysis, and Measurement Laboratory, UCLA. In 2012, he joined the Department of Electronic Engineering, Tsinghua University, China, as an associate professor. His current research interests include novel designs of high-gain antennas for advanced applications, artificial electromagnetic structures, and electromagnetic and antenna theories.

ZHANG Jiannian received the B.S degree from Tsinghua University, China. He has 20 years of experience in system development. He was a senior engineer with the State Key Laboratory of Microwave and Digital Communication of Tsinghua University. He was the head of the System Department of Analogix Semiconductor, Inc., USA. Now he is the CEO of Beijing Actenna Technology Co., Ltd.

Design of Millimeter-Wave Antenna-in-Package (AiP) for 5G NR

CHANG Su-Wei, LIN Chueh-Jen, TSAI Wen-Tsai, HUNG Tzu-Chieh, HUANG Po-Chia
(TMY Technology Inc., New Taipei City, Taiwan 235, China)

Abstract: For 5G new radio (NR), there are two frequency bands: Frequency Range 1 (FR-1) (low frequency) and Frequency Range 2 (FR-2) (millimeter-wave frequency). Millimeter-wave has been officially utilized in mobile applications. The wide bandwidth is the key for the millimeter-wave band. However, higher loss has become the major challenge for the wide use of this frequency range. Antenna array and beamforming technologies have been introduced to resolve the path loss and coverage problems. The key design considerations of the beamforming antenna array are low loss, compact system and small size. Antenna-in-package (AiP) has become the most attractive technology for millimeter-wave front-end system. For the design of AiP, many parameters such as RF transition, material and heat need to be considered and designed properly. The Over-the-Air (OTA) testing technology is also very critical for AiP mass production. In this paper, the detail of AiP design and new OTA testing technology are discussed and demonstrated.

Keywords: 5G; antenna-in-package (AiP); beamforming; FR-2; millimeter-wave; new radio (NR); phased-array; low temperature cofired ceramic (LTCC)

DOI: 10.12142/ZTECOM.202003005

https://kns.cnki.net/kcms/detail/34.1294.TN.20200917.0851.002.html, published online September 17, 2020

Manuscript received: 2020-06-16

Citation (IEEE Format): S.-W. Chang, C.-J. Lin, W.-T. Tsai, et al., "Design of millimeter-wave antenna-in-package (AiP) for 5G NR," *ZTE Communications*, vol. 18, no. 3, pp. 26 – 32, Sept. 2020. doi: 10.12142/ZTECOM.202003005.

1 Introduction

Antenna-in-package (AiP) is a technology that integrates antennas along with the transceiver and power dies into a system-in-package module. It has been widely used in the millimeter-wave antenna array such as 60 GHz gesture sensors, 77 GHz automobile radars, 94 GHz phased array, or even frequencies as high as 122 GHz for imaging sensors and 300 GHz for wireless links. 5G millimeter-wave spectrum can promise sufficient bandwidth to provide the next-generation user experience and industrial applications by using millimeter-wave as the carrier frequencies.

The idea of AiP technology can be traced back to the 90s when antenna designers had dedicated their time to minimizing the size of the antenna. In the meantime, another idea was to integrate the antenna with the front-end system to achieve a more compact system. At an early development stage, AiP was developed together with Bluetooth technology. Later on, AiP was widely implemented into millimeter-wave radar systems. IBM, Intel, Samsung, Google, etc., have realized the AiP modules at 60 GHz, 77 GHz, and 94 GHz. Recently, 5G mobile communications and terahertz technology are becoming more and more important. Qualcomm has announced the world's first 28 GHz AiP module for cellphone[1]. Except for radar applications, 60 GHz is used for wireless communications of the

IEEE 802.15.3c standard. Besides the AiP technology, antenna-on-chip (AoC) has also been studied for 60 GHz, where the antenna is fabricated with other circuits on a wafer. AoC technology is more suitable for terahertz applications. However, the efficiency of AoC is only 11.5%. Instead, AiP has shown high efficiency of more than 90% when low temperature co-fired ceramic (LTCC)[2] is used for manufacturing.

The requirements of AiP are multifunction, high-capacity and small size. The multilayer integration and package technology have demonstrated its capability of low profile, low cost and potentially high-volume production. A proper multilayer design can help to improve the bandwidth and impedance match and lower the coupling effect between lines. For millimeter-wave systems, the fabrication process and capability affect the performance significantly. High density interconnects printed circuit board (HDI PCB) and LTCC are conventional multilayer technologies. The microstrip line is the most common technology for signal transmission between the layers. However, the flexibility of the microstrip line is limited by its two-dimensional structure. An innovative multilayer substrate integrated waveguide (SIW) is presented to give designers more freedom when designing AiP modules. SIW is an emerging type of rectangular dielectric-filled waveguide which is fabricated by arrays of metallic vias to realize the bilateral edge or sidewalls. The three-dimensional structure supports very high flexibility when designing an AiP module [3].

In this paper, the design considerations and architectures will be discussed along with the capabilities and the products of TMY Technology Inc. (TMYTEK). TMYTEK is a millimeter-wave company that specializes in 5G solutions such as AiP front-end modules, beamforming technologies and testing systems.

2 Design Considerations and Architectures

To fulfill the increasing demands in the millimeter-wave front-end module (FEM), AiP turns into the most promising and suitable technology to achieve the phased arrays cost-effectively. At the same time, the material and process choices involving tradeoffs among engineering constraints are also considered, including heat management, control design, RF performance, calibrations, and more (**Fig. 1**). The solution to multiple dimensional engineering problems is not linear and needs a lot of experience and creativity to realize the products. In addition to design, mass production is also a significant challenge, especially in Over-the-Air (OTA) testing.

2.1 System Architectures

Fig. 2 shows three different architectures for the 5G phased array. In the antenna and beamformer architecture, the block shows an RF FEM with an analog beamformer which includes antenna array, duplexer and beamformer. Nowadays, a couple of beamformer chip makers have announced beamformer chips optimized for 5G millimeter-wave bands. The second architecture integrates intemediate frequency (IF)-radio frequency (RF) conversion into the module as indicated in the rectangular block labeled with up and down conversion. Given that frequency converters dramatically affect the quality of communication, embedding it into the system increases system performance and reduces the complication of integration. Integrating mixers and filters in the package is not a trivial job, and local oscillator (LO) signal distribution is another concern, especially in large, tiled array. The third architecture is based on open radio access network's (ORAN's) split option 7.2 to integrate the low physical (Low PHY) layer into the module to offload the front-haul network on the radio access network (RAN). In this architecture, digital components are included, which raise the challenges to a new level.

2.2 Design Considerations

The design considerations of AiP are the multi-dimensional engineering problems due to its complexity and high density. This section is divided into four sub-sections: beamforming integrated circuit (IC) and up/down converter chips, fabrication technologies and materials, design of antenna and transition, and design of feeding networks and filters.

2.2.1 Beamforming IC and Up/Down Converter Chips

A modern beamformer chip integrates power amplifiers (PAs), low noise amplifiers (LNAs), phase shifters (PSs), variable attenuators and T/R switches. Complementary metal oxide semiconductor (CMOS), CMOS silicon on insulator (SOI), and bipolar CMOS (BiCMOS) technologies are preferred due to the benefit of digital circuit integration and low cost, even if the output power is not as good as the III-V compound processes such as GaAs and GaN. The main specifications that need to be considered are transmitter gain and power, receiver gain

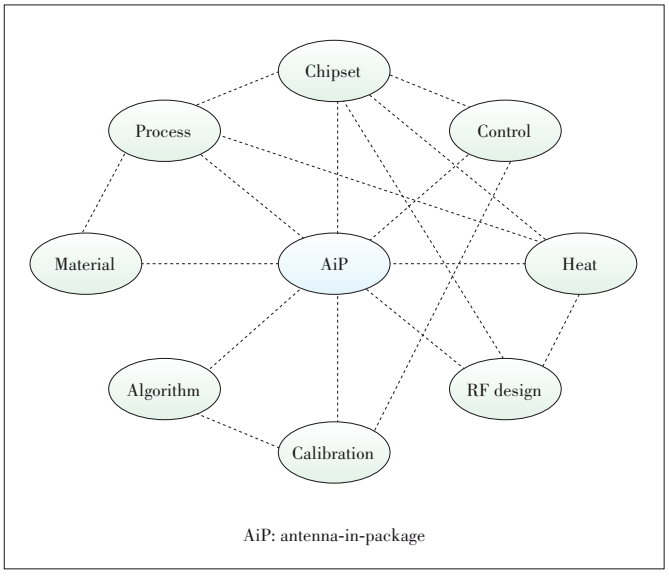

▲**Figure 1. System context diagram of AiP design parameters.**

and noise, phase resolution and RMS error, attenuation range and resolution, memory size, beamforming control speed, power consumption, and cost. In a 5G millimeter-wave phased array, the output power is not the only concern. Due to the feature of Orthogonal Frequency Division Multiplexing (OFDM) in 5G, the power amplifier (PA) back-off operation is necessary. It is considered along with antenna array gain to form a system with targeted equivalent isotropically radiated power (EIRP) and reasonable power efficiency (**Table 1**). The design considerations of up/down converters are conversion gain, noise, linearity, LO pumping power, and isolations.

2.2.2 Fabrication Technologies and Materials

Fabrication technologies and materials are critical for the performance, cost, and size of the AiP module. There are three major technologies for AiP manufacturing: HDI PCB, LTCC and fan-out wafer-level packaging (FOWLP)[4]. **Table 2** shows the capability comparison of the three technologies. For the material selection, dielectric constant (Dk) and loss tangent (Df) are the main considerations. Thermal conductivity, Dk and Df change with temperature. Thickness ranges of core board and prepreg are also important in AiP design. **Fig. 3** shows the performances of Dk and Df with different materials.

2.2.3 Design of Antenna and Transition

In low frequency (FR-1), the antenna radiation pattern is typically designed as omnidirectional antenna. In millimeter-wave frequency (FR-2), antenna array has become the essential solution to compensating for the higher path loss at this frequency range. The consideration of the antenna array is dif-

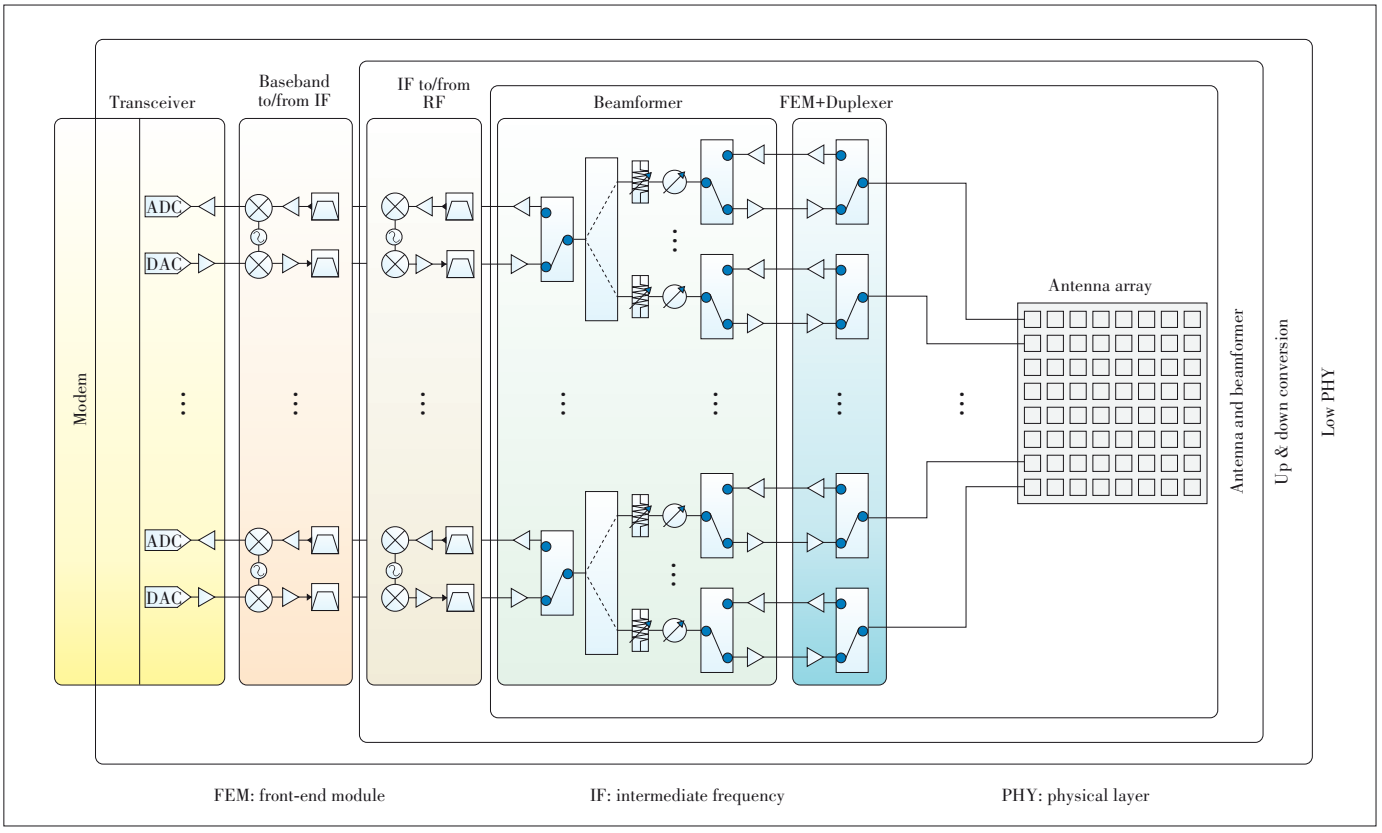

▲**Figure 2. Three different system architectures of antenna-in-package (AiP) design.**

▼**Table 1. Beamforming design considerations and TMYTEK's capability**

Index	Consideration	TMYTEK's Capability
Tx Power	Output power of each element	18 dBm for 28 GHz 15 dBm for 39 GHz
Frequency	Meeting operator's frequency bands	n257, n258, n260, n261 Ranges from 24 to 41 GHz
Rx NF	Better system sensitivity provided by lower noise floor	4.5 dBm in 28 GHz 6.5 dBm for 39 GHz.
Phase	Phase difference is the basic of beamforming; step size and error are the key considerations.	6-bit phase shifter ±3° RMS phase error

NF: noise figure RMS: root-mean square

▼ **Table 2. Capability comparison of three main antenna-in-package (AiP) fabrication technologies**

Parameter	HDI PCB	LTCC	FOWLP
Maximum layer	16	60	2 – 6
Minimum layer thickness/μm	35	25	5
Minimum board thickness/μm	300	500	400
Dielectric constant	3 – 6	4 – 8	2.6 – 3.6
Loss tangent	0.002 – 0.02	0.002 – 0.005	0.004 – 0.01
Metal	Cu	Au, Ag, Cu	Cu
Line/space/μm	45/45	40/40	5/5
Via diameter/μm	75	50	25
Inner cavity build	x	v	v

FOWLP: fan-out wafer-level packaging
HDI PCB: high density interconnects printed circuit board
LTCC: low temperature cofired ceramic

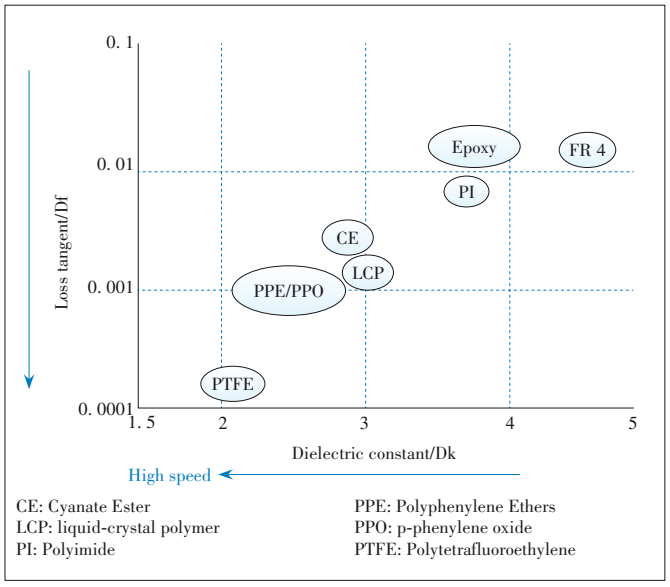

▲ **Figure 3. Dielectric constant and loss tangent of different materials.**

ferent compared with the design of single antenna, especially including the beamforming technology. Beam pattern, beam steering range, sidelobe suppression, beam pattern symmetry between two polarizations, antenna gain, isolation between array elements, antenna bandwidth, antenna efficiency, and return loss are all the critical design parameters. Normally, the traditional planar antenna has a design of two layers, which is hard to have a good performance for the above parameters simultaneously. The multilayer antenna technology has more design flexibility to achieve better performance. However, the design also becomes more complicated. The design of multilayer introduces the vertical structures such as the via wall into the antenna to improve the isolation or the director to improve the directivity. Nevertheless, the transition design between layers is the most critical part of this multilayer antenna design. A good transition design means having a better impedance match. The manufacturing process and capability affect the flexibility of transition and limit the final performance. **Fig. 4**

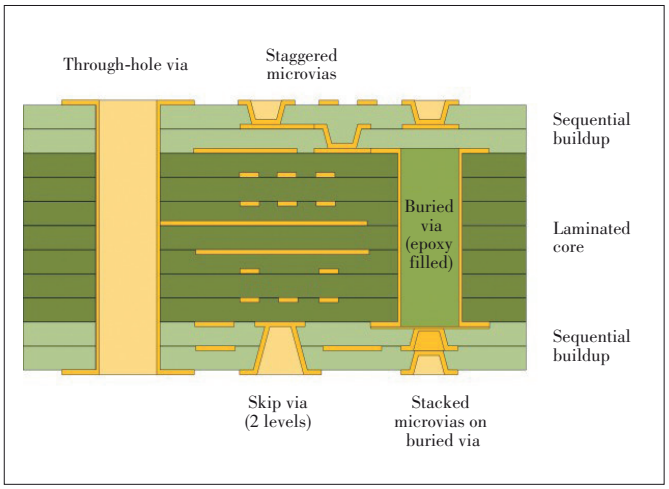

▲ **Figure 4. High density interconnects (HDI) type III structure[5].**

shows the HDI type III stack and via types. It has two levels of microvias, buried vias and regular through-hole vias. The microvias are used effectively in improving signal and power integrity.

2.2.4 Design of Feeding Networks and Filters

Building a feeding network is critical to the antenna array as the components cannot be placed off-board. Size and complexity are important for measuring feeding network performance. The commercial off-the-shelf (COTS) beamforming ICs has 4, 8, or 16 channels. For 5G gNB, 4 × 4 or 8 × 8 antenna array is used as a standard unit cell, which might operate as single or dual polarization. Since the feeding network connects the beamforming ICs and antenna elements, it has to incorporate matching circuits to achieve wideband operation. Good isolation between dual-polarization ports has to be assured to achieve a low cross-polarization coefficient[6]. The multilayer design which is described in the last section is also considered for achieving a better impedance match of transition.

The filter design is limited to the board area available for passive components. The larger the room for filters, the better the rejection performance can be achieved. At the same time, thermal stability and repeatability are also challenging for designers to reduce the tuning effort to achieve an SMT- capable device. As an example of the microstrip structure, the tolerance of substrate thickness, etching size and even dielectric constant should be considered and calculated carefully to achieve the best performance at the millimeter-wave range.

2.3 OTA Measurement for AiP Module

Conductive testing is no longer an option for the millimeter-wave module implemented by AiP technology. There are no connectors or testing points available for the purpose. The only way to characterize the module is through the OTA method.

Traditionally, a bulky chamber along with one or more mechanical positioners needs to ensure the device under test's (DUT's) radiation pattern can be measured correctly and pre-

cisely, as shown in **Fig. 5**[7]. More recently, a compact antenna test range (CATR) technology has reduced the size of the chamber but still retains the same concept of mechanical parts and testing items based on radiation patterns shown in **Fig. 6**[8]. The approach used for decades has become an industry standard for research and design. However, in the coming 5G era, the number of devices to be tested on the product line will overwhelm this old technology. A traditional chamber or CATR is a good tool for research and design purposes, but it is too slow and bulky for production lines. For example, the latest technology in the industry can get a pattern in about a few minutes, which is impressive if we compare it to our predecessors with a half-hour or longer testing cycles. However, achieving the level of seconds is still not guaranteed. Furthermore, the nature of mechanical positioners makes automation integration in product lines not a straightforward task.

A new method for OTA measurement of production lines is built for 5G millimeter-wave beamforming antenna arrays by TMYTEK[9]. It adopts different approaches to meet the production demands of millimeter-wave AiP modules. The mechanical positioner is removed to speed up the OTA testing time. TMYTEK's BBox™ technology is used to measure the RF performance of a millimeter-wave module or device, including error vector magnitude (EVM), EIRP, frequency error, adjacent channel leakage ratio (ACLR), etc. [10–11]. The system architecture is shown in **Fig. 7**. The main idea is to measure AiP with another beamforming array (BBox™). This topology requires the calibration process to eliminate the phase and amplitude errors due to the angular misalignment between the two antenna patterns. The results are measured by a signal analyzer with a signal generator and integrate the up/down converters (UD Box) to down-convert the millimeter-wave signal to lower frequency. The measuring time is dramatically decreased since the scanning is done by electronic control.

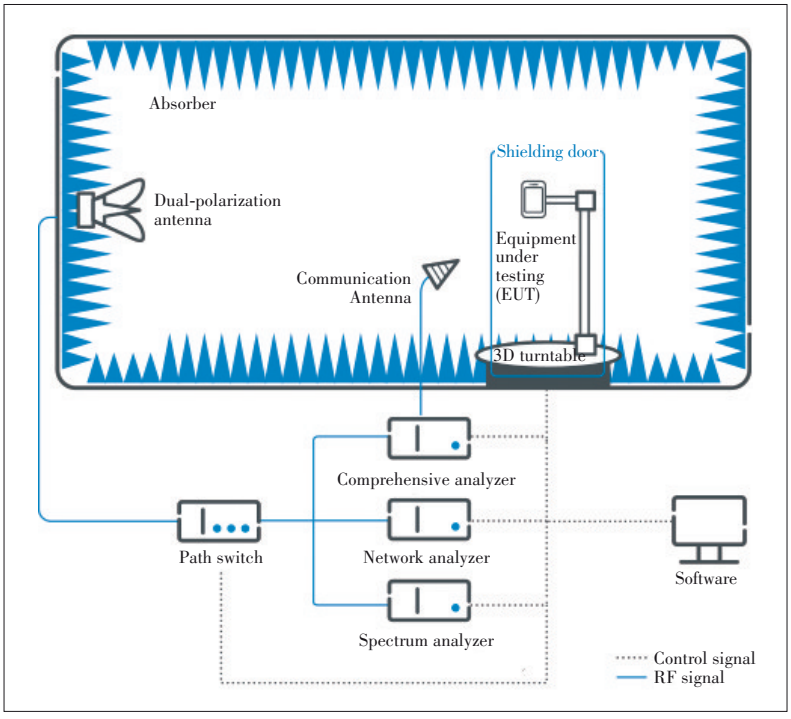

▲**Figure 5. Traditional Over-the-Air (OTA) chamber system.**

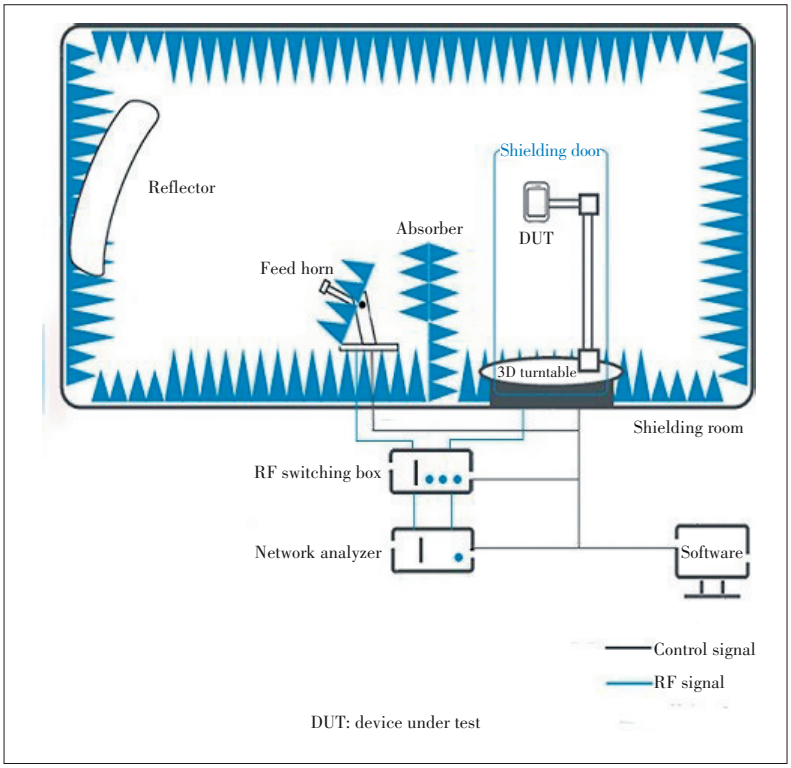

▲**Figure 6. Compact antenna test range (CATR) chamber system.**

3 Design Example

TMYTEK cooperated with NTK Technologies, Inc.[12], a Japanese LTCC technology company. A 4 × 4 LTCC unit AiP module for the 5G FR2 n261 band (27.5 – 28.35 GHz) has been designed by TMYTEK and manufactured by NTK. A larger 8×8 array is also demonstrated by tiling up to four-unit modules on one single motherboard. For the design of 5G NR millimeter wave beamforming antenna array, the size of the antenna array could be very different, i.e. 4 × 4, 8 × 8, 16 × 16, even larger, for different applications. Therefore, the modularization meth-

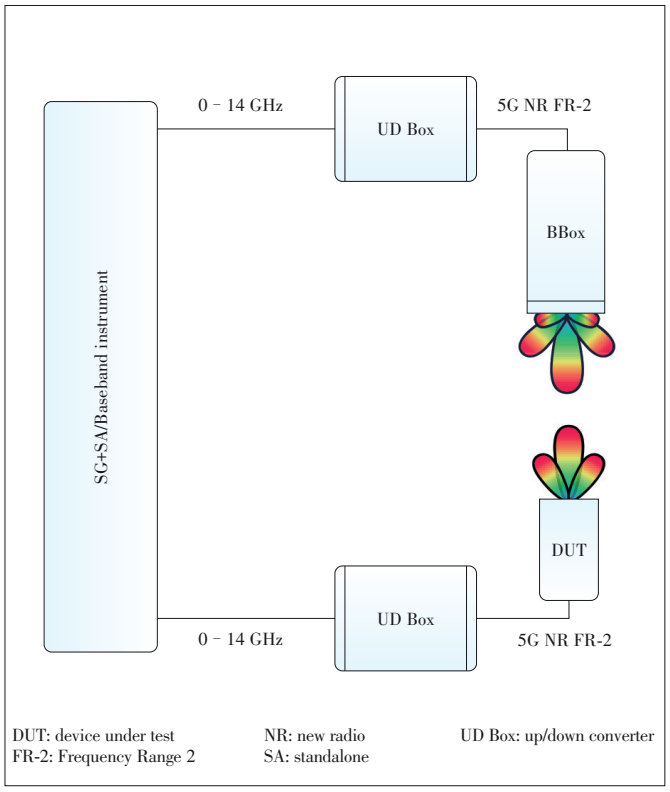

▲Figure 7. New over-the-air (OTA) system.

od provides a better way to configure a phased array system for adapting different dimensions of antenna arrays.

A 4 × 4 LTCC antenna-in-package front-end module (AiP FEM) is presented in this paper, along with the 28 GHz 8 × 8 phased array system which is fully integrated with four 4×4 AiP FEMs, an up/down converter and a phase-locked oscillator. The AiP FEM is fabricated with a 26-layer LTCC process by NTK. It is integrated with four 4-channel beamformer chipsets, power combiner, filter, mixer, frequency doubler and sixteen substrate integrated waveguide (SIW) antennas. **Fig. 8** shows three layers of the 26-layer LTCC AiP FEM. The input and output ports are the transmitting/receiving IF signals, LO source, digital control signals and DC power supply. The phase and amplitude of each antenna channel can be controlled independently for beam steering and beam shaping capabilities. The serial peripheral interface (SPI) control interface is used for fast control of beamforming characteristics, and the highest SPI clock rate has reached 50 MHz. The dimension of AiP FEM is 29.3 × 22.1 × 4.1 mm^3 (**Fig. 9**). The cavity shown on the backside is designed for easy mounting of devices to form a different size of the phased array using these modularized AiP FEMs.

The 8 × 8 phased array system was integrated using four AiP FEMs mounted on the motherboard. For obtaining better phase noise, the local oscillator source was not embedded in the AiP FEMs; instead, they are integrated into the motherboard. **Fig. 10** shows the integrated system photo. There are

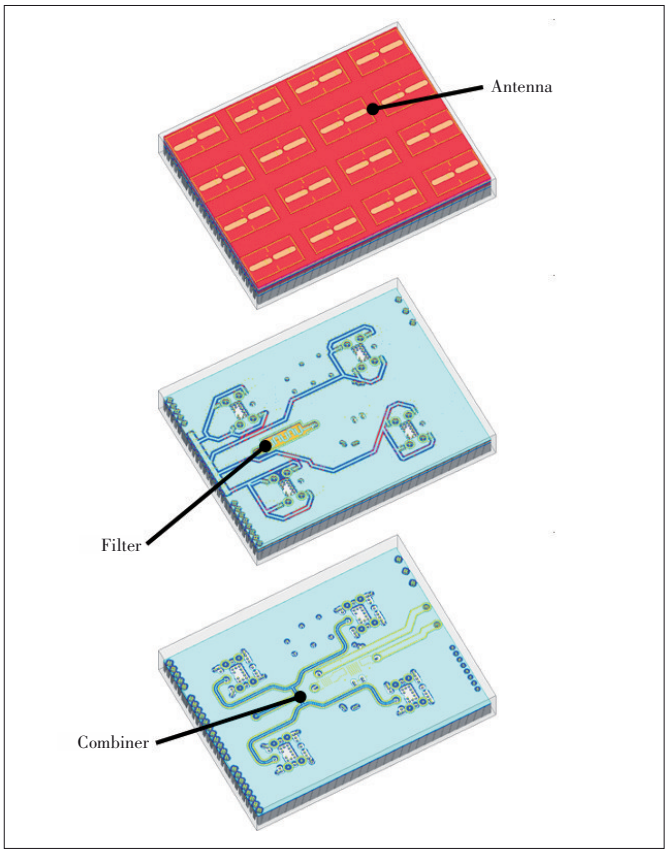

▲Figure 8. Three layers of the 26-layer low temperature cofired ceramic (LTCC) antenna-in-package front-end module: antenna, filter and combiner.

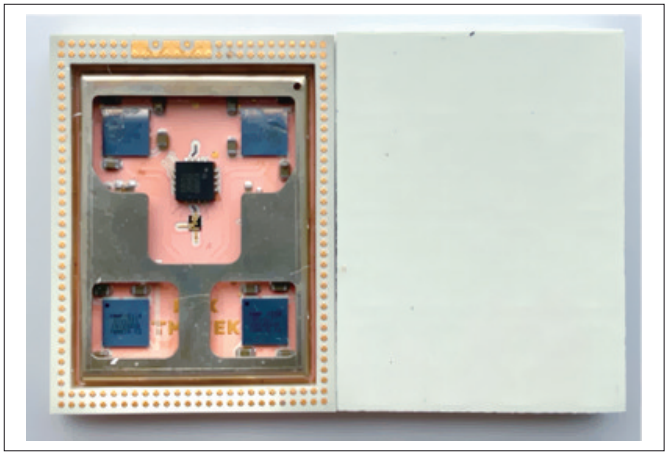

▲Figure 9. Top and bottom view of the 26-layer low temperature cofired ceramic (LTCC) 4 × 4 antenna-in-package front-end module for 28 GHz band.

two fans placed beside the AiP FEMs, which are not shown on the photo, to have better heat dissipation.

4 Conclusions

The design of millimeter-wave antenna-in-package is discussed and an example from TMYTEK is presented in this paper. The millimeter-wave technology has become more and

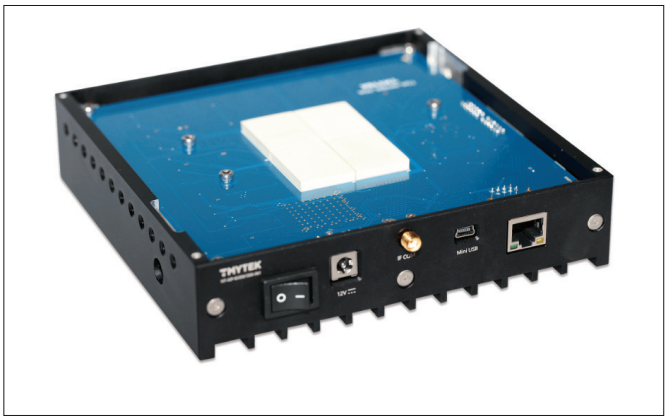

▲ **Figure 10. 8 × 8 phased array system integrated with four antenna-in-package front-end modules.**

more important for communications and radar applications. Thus, the considerations for AiP mass production are very critical for having better system performance and lower cost. This paper has discussed the manufacturing technologies and materials. Moreover, the importance of the OTA measurement solution is highlighted. TMYTEK has developed the best OTA solution for AiP mass production to accelerate the development of 5G millimeter-wave industries.

Acknowledgment

We would like to acknowledge the contributions and cooperation of the LTCC leading manufacture company, NGK, for the manufacturing of the 4 × 4 LTCC AiP substrate.

References

[1] ZHANG Y P. A review of the development of antenna-in-package technology [J]. ZTE technology journal, 2017, 23(6): 41 – 49. DOI: 10.3969/ j.issn.1009-6868.2017.06.010
[2] ZHANG Y P, LIU D X. Antenna-on-chip and antenna-in-package solutions to highly integrated millimeter-wave devices for wireless communications [J]. IEEE transactions on antennas and propagation, 2009, 57(10): 2830 – 2841. DOI: 10.1109/tap.2009.2029295
[3] DJERAFI T, WU K. Multilayer integration and packaging on substrate integrated waveguide for next generation wireless applications [C]//46th European Microwave Conference (EuMC), London, UK: IEEE, 2016: 858 – 861. DOI: 10.1109/eumc.2016.7824479
[4] ZHANG Y P. Recent advances in antenna-in-package technology [J]. ZTE technology journal, 2018, 24(5): 47 – 53. DOI: 10.19729/j.cnki.1009-6868.2018.05.010
[5] HUSBY H. High density interconnect [EB/OL]. [2020-05-01]. https://www.datarespons.com/high-density-interconnect
[6] JAWORSKI G, KROZER V. A design of feeding network for a dual-linear polarization, stacked, probe-fed microstrip patch antenna array [C]//15th International Conference on Microwaves, Radar and Wireless Communications, Warsaw, Poland: IEEE, 2004: 473 – 476. DOI: 10.1109/mikon.2004.1357069
[7] ATENLAB. OTA [EB/OL]. [2020-05-01]. https://www.atenlab.com.tw/article-OTA.html
[8] ATENLAB. CATR [EB/OL]. [2020-05-01]. https://www.atenlab.com.tw/article-CATR.html
[9] CHANG S.W. New method of OTA measurement for 5G mmWave beamforming antenna array [C]//Asia-Pacific Microwave Conference. Singapore, Singapore, 2019
[10] TMYTEK. Bbox [EB/OL]. [2020-05-01]. https://www.tmytek.com/product/bbox
[11] TSUTOMU Tokuke. 5G test challenges [EB/OL]. [2020-05-01]. https://www.tele.soumu.go.jp/resource/j/equ/mra/pdf/30/e/11.pdf
[12] NTK. TMYTEK cooperated with NTK Technologies [EB/OL]. [2020-04-20]. http://www.ntktech.com

Biographies

CHANG Su-Wei (swchang@tmytek.com) received the M.S. degree in electrical and computer engineering from the University of Massachusetts Amherst, USA in 2018. He worked in Academia Sinica Institute of Astronomy & Astrophysics (ASIAA) in Taiwan, China as a microwave/sub-mmWave receiver engineer, where he was involved in developing the mmWave and sub-mmWave receiver system for international radio telescopes. In 2014, he founded TMYTEK and is currently the president and CEO. His research interests include noise, cryogenic circuits and applications, silicon-based RFIC and MMIC up to mmWave bands. He has 45 SCI publications with more than 500 citations.

LIN Chueh-Jen is a serial entrepreneur who has founded three companies since 2007. He is the VP and co-founder of TMYTEK, a start-up company that focuses on 5G mmWave solutions. He leads the software technology and marketing teams and helped the company successfully raise pre-A and A funds. Before TMYTEK, he founded Scarlet Tech, a successful IoT company still running today. He ever worked for the smartphone maker HTC and cooperated with Microsoft and Qualcomm closely in software and wireless communications. He built the world's largest infrared telescope (WIRCam) for CFHT in Hawaii in the first job. He received the master's degree in electronics engineering on Quantum dots IR detectors from Chiao-Tung University, Taiwan, China.

TSAI Wen-Tsai received the B.S. degree in electrical engineering from Kaohsiung Marine University, Taiwan, China in 2002, and the M.S. degree in electrical engineering from Feng Chia University, Taiwan, China in 2004. He has five years of experience in the antenna-related design, including the wireless local-area network (WLAN) antenna, global position system (GPS) antenna, mmWave circuit, 5G small cell, 5G AiP module, mobile antenna and antenna diversity. Moreover, he set up the far-field antenna pattern measurement systems (in anechoic chamber) and control program and has nine-to-ten years of experience in the design of Ku and Ka bands circuits, as well as the design, fabrication and measurement of low-noise amplifiers, mixers, filters, phase-lock loop (PLL) and dielectric resonant oscillator (DRO) circuits, integrated the horn antennas. He also has rich experience in HSpice simulation of active circuits.

HUNG Tzu-Chieh received the B.S. degree in electrical engineering from Feng Chia University, Taiwan, China in 2006, and the M.S. degree in electrical engineering from Central University, Taiwan, China in 2008. During college, he participated in ASIAA student program and joined the Yuan-Tseh Lee Array (YTLA, formerly AMiBA) project. He started his professional career at Lite-On technology Inc. in 2009, where he was an antenna designer. From 2013 – 2015, he was an RF engineer with Ubiqconn technology Inc. In March 2015, he joined TMYTEK Inc. as a RF/mmWave system designer and has become an R&D manager in February 2020. His research interests include mmWave circuit design and system integration.

HUANG Po-Chia has rich experience in embedded system software development and digital signal processing and now focuses on software system and architecture design with TMYTEK. Before TMYTEK, he joined Scarlet Tech at the end of 2014 for building up IoT solutions in safety industry. His expertise is in MCU programming and a variety of protocol stacks for wireless technologies, such as BLE and LoRa. In 2011, he worked at HTC and took responsibility of mobile graphic framework and relevant BSP for a customized mobile OS on Qualcomm Snapdragon 600. He received the master's degree in electrical and control engineering on DSP and embedded system development from Chia-Tung University, Taiwan, China.

Integrated 3D Fan-out Package of RF Microsystem and Antenna for 5G Communications

XIA Chenhui, WANG Gang, WANG Bo, MING Xuefei
(The 58th Research Institute of China Electronics Technology Group Corporation, Wuxi 214000, China)

Abstract: A 3D fan-out packaging method for the integration of 5G communication RF microsystem and antenna is studied. First of all, through the double-sided wiring technology on the glass wafer, the fabrication of 5G antenna array is realized. Then the low power devices such as through silicon via (TSV) transfer chips, filters and antenna tuners are flip-welded on the glass wafer, and the glass wafer is reformed into a wafer permanently bonded with glass and resin by the injection molding process with resin material. Finally, the thinning resin surface leaks out of the TSV transfer chip, the rewiring is carried out on the resin surface, and then the power amplifier, low-noise amplifier, power management and other devices are flip-welded on the resin wafer surface. A ball grid array (BGA) is implanted to form the final package. The loss of the RF transmission line is measured by using the RF millimeter wave probe table. The results show that the RF transmission loss from the chip end to the antenna end in the fan-out package is very small, and it is only 0.26 dB/mm when working in 60 GHz. A slot coupling antenna is designed on the glass wafer. The antenna can operate at 60 GHz and the maximum gain can reach 6 dB within the working bandwidth. This demonstration successfully provides a feasible solution for the 3D fan-out integration of RF microsystem and antenna in 5G communications.

Keywords: AiP; fan-out package; RF microsystem; 3D integration; 5G communications

DOI: 10.12142/ZTECOM.202003006

https://kns.cnki.net/kcms/detail/34.1294.TN.20200908.1443.006.html, published online September 10, 2020

Manuscript received: 2020-07-27

Citation (IEEE Format): C. H. Xia, G. Wang, B. Wang, et al., "Integrated 3D fan-out package of RF microsystem and antenna for 5G communication," *ZTE Communications*, vol. 18, no. 3, pp. 33 – 41, Sept. 2020. doi: 10.12142/ZTECOM.202003006.

1 Introduction

Owing to the growing operating frequency up to hundreds of gigahertz, minimized size and power consumption, as well as the requirement of better performance of RF system, the novel communication and sensing applications such as 5G and automotive applications are urged to integrate every section part of RF system chain, so as to establish the "everything in one" module with minisize and multi-functions. As the wave length of microwave shrinks with the growing of its frequency, the characteristically electrical length of antennas and transmitting lines can be reduced to millimeter or even micron level, which calls for higher fabrication accuracy of interconnection process. Besides, packaging process with heterogeneous integration ability offers an opportunity for novel package architecture with chips of different materials and fab features[1]. The antenna-in-package (AiP) based on wafer level fabrication process can fabricate tremendous modules simultaneously with semiconductor process, which offers compact and low cost solution and paves a possible way for RF modules with high perfor-

mance and low cost[2].

In order to meet the needs of 5G miniaturized communication systems, new packaging technologies in the millimeter wave frequency range are needed to solve the basic technical challenges of millimeter wave, such as low loss and ultra wideband interconnection, high wiring density, thin packaging substrate, high performance integrated passive devices (IPD) and reducing shape factors[3]. Dozens of papers are reported on AiP and its applications[4]. The cutting edge system corporations and outsourced semiconductor assembly and tests (OSATs) have offered numbers of AiP solutions, many of which are based on wafer level fan-out (WLFO) process, and the substrate options focus on silicon, organic compound, glass and more[5 - 6]. The glass substrate with low epsilon and coefficient of thermal expansion (CTE) is an ideal choice for high frequency application, and the compound substrate allows process flows with low price and agile combination, which is convenient for heterogeneous integration[7 - 8]. By combing glass and compound substrates in AiP module, the advantages of performance and cost can be taken together. The encapsulated antenna in 60 GHz band is a research hotspot. The traditional printed circuit board (PCB) technology is very convenient to realize multi-layer structure and antenna array[9]. The low temperature co-fired ceramic (LTCC) technology has the advantages of light and thin structure, many wiring layers and narrow line width, but its lamination temperature is higher than 850 ℃, which is much higher than that of destroying active devices. Therefore, although it is possible to create sealed multilayer substrates with integrated passive components and antennas, active devices must be packaged and connected separately because of the high temperature process of LTCC[10 - 11].

A 3D fan-out integrated packaging method for 5G communications RF microsystem and antenna is presented in this paper. Based on a new 3D fan-out wafer-level packaging architecture, the permanent bonding process of glass wafer and resin reconstructed wafer is designed. Based on glass and resin composite materials, the high density integrated interconnection of heterogeneous chip and antenna array is realized. Finally, the process manufacturing of antenna and packaging module is completed, and the high quality 5G communications AiP module manufacturing is realized. It can provide 64 antenna channels and 7 RF chips. The volume is only 18 mm × 18 mm × 1 mm, which can meet the application requirements of miniaturized 5G communications equipment.

2 Measurement of Transmission Loss

In order to obtain the RF transmission performance of the 3D fan-out integrated package, a planar coplanar waveguide (CPW) transmission line and a 3D stacked CPW transmission structure are fabricated. Because the connection between the RF microsystem and the antenna usually uses CPW, it is very important to obtain the RF transmission loss of CPW[12]. The CPW transmission line is realized by redistribution layer (RDL) process in 3D fan-out wafer level packaging. The structure of CPW transmission line is distributed on both sides of the signal line, so it is very suitable for millimeter wave probe station, and more convenient for testing. The structure of CPW is shown in **Fig. 1**.

Firstly, the CPW transmission line structure is fabricated on the glass wafer. The picture of the CPW transmission line is shown in **Fig. 2**. The dielectric constant of the glass wafer is 6.3 and the dielectric loss tangent is 0.01, and the thickness of the glass substrate is 300 μm. The transmission line is made of copper and is 5 μm thick. The surface of the transmis-

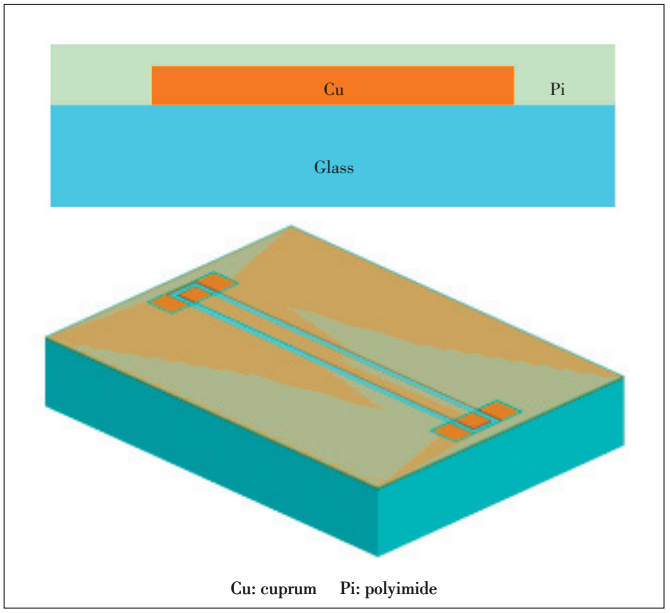

▲**Figure 1. Structure of coplanar waveguide (CPW).**

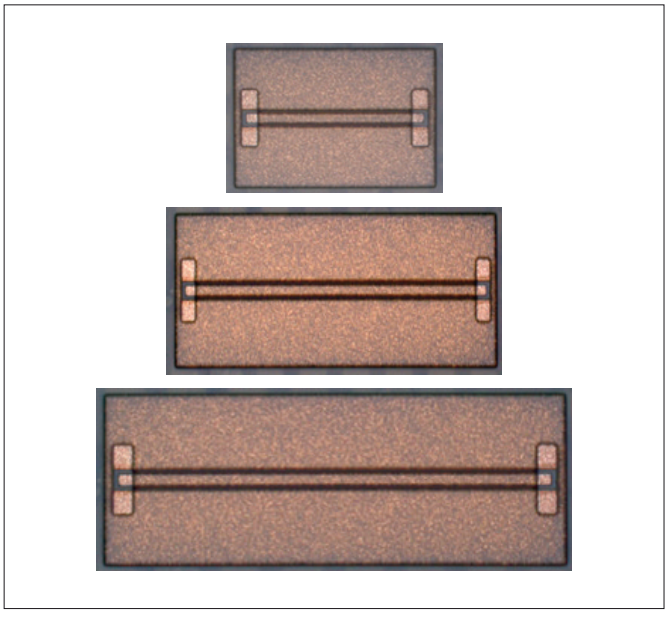

▲**Figure 2. Coplanar waveguide (CPW) with 3 different lengths.**

sion line is covered with a 10 μm thick polyimide to protect the copper wiring layer from oxidation. The width of the CPW transmission line is 70 μm and the spacing is 25 μm. CPW transmission lines with lengths of 1.00 mm, 1.60 mm and 2.20 mm are fabricated respectively. A rectangular test window of 100 μm × 300 μm is opened in the polyimide layer at both ends of the transmission line.

The transmission line is measured on a high frequency probe test bench, using a ground-signal-ground (GSG) probe with a distance of 100 μm and a phasor network analyzer (PNA) network analyzer for 67 GHz performance. The test results are shown in **Fig. 3**, and it can be found that the radio frequency transmission loss of the CPW transmission line on the glass wafer is very small. It can be seen from the figure that there are some differences between the test results and the simulation results. This is because wafer manufacturers can only give the dielectric constant and loss tangent angle of glass below 5 GHz, which makes the simulation results in the high frequency part above 5 GHz inaccurate. In addition, the test joint of the high frequency probe table will also lead to part of the insertion loss.

The transmission loss of CPW working in 60 GHz is calculated. When the CPW transmission line works in 60 GHz, the insertion loss is 0.26 dB/mm, as shown in **Table 1**, where the RF transmission loss of glass wafers is very small, and it is a good choice for 3D fan-out integration of RF microsystems and antennas.

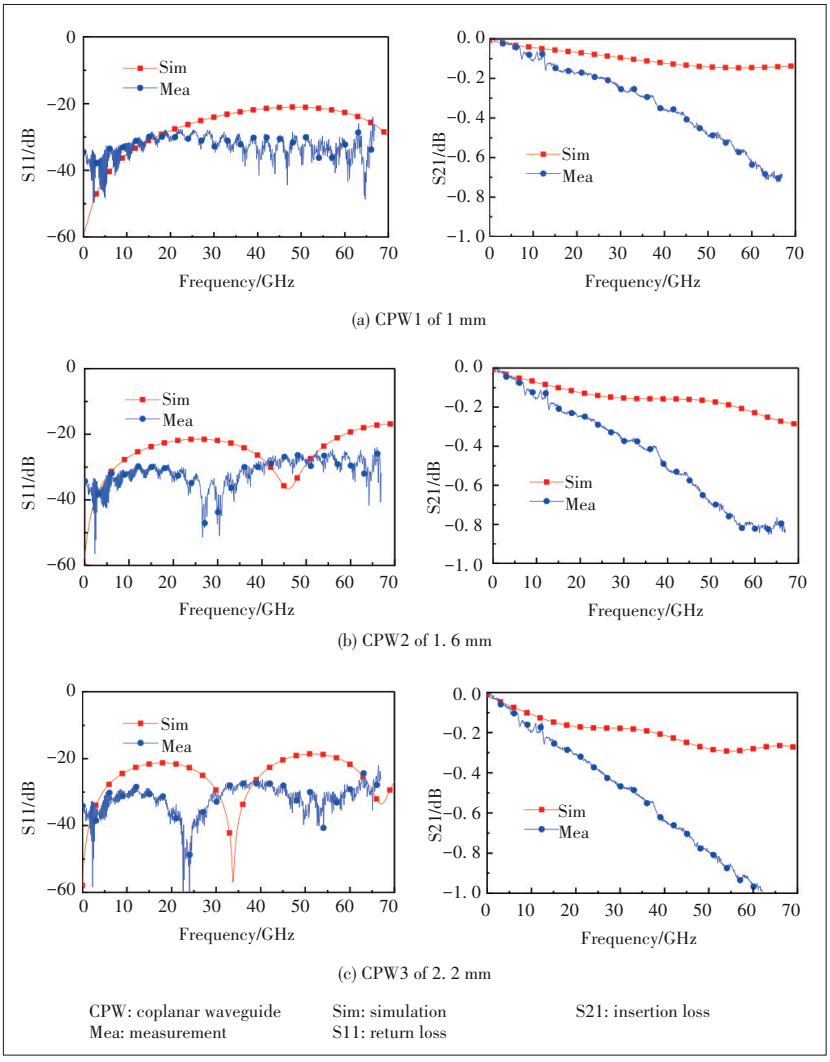

▲**Figure 3. Comparison of test and simulation results of CPW.**

Then the glass-based CPW transmission line is packaged through the fan-out type to form a fan-out package to simulate the fan-out package structure of the RF chip. Solder balls are planted at the leading end of the package and flip-flopped on the glass-based CPW substrate to test a completed transmission link from the chip end to the package. The photos of the process structure and processing are shown in **Fig. 4**. **Fig. 5** shows the complete signal path, and the processing size of the stack interconnected package is 5 mm × 6 mm × 0.92 mm.

The 3D stacked transmission structure is finally measured in the high-frequency probe table, and the test results are shown in **Fig. 6**. It can be seen that the RF transmission loss of the 3D stacked CPW transmission structure is very small, which indicates that the 3D fan-out package structure will not bring about too much loss. Fig.6 shows that there are some differences between the test results and the simulation results. This is because the wafer manufacturer cannot give the material electrical parameters in the high frequency stage, which will affect the simulation results in the high frequency band. But the test results are basically consistent with the simulation results, which shows that the early simulation has a certain guiding significance.

▼**Table 1. CPW transmission loss operating in 60 GHz**

Serial Number	Length/mm	Insertion Loss/dB (in 60 GHz)	Unit Length Loss (dB/mm)
CPW1	1.00	0.61	0.3
CPW2	1.60	0.79	0.23
CPW3	2.20	0.93	0.26

CPW: coplanar waveguide

3 Design and Measurement of AiP

The patch antenna is very suitable for wafer-level processing[13]. The wiring process is carried out on the positive and negative sides of the glass wafer (300 μm thick, dielectric constant is 6.3, and dielectric loss tangent is 0.01) to form a slot

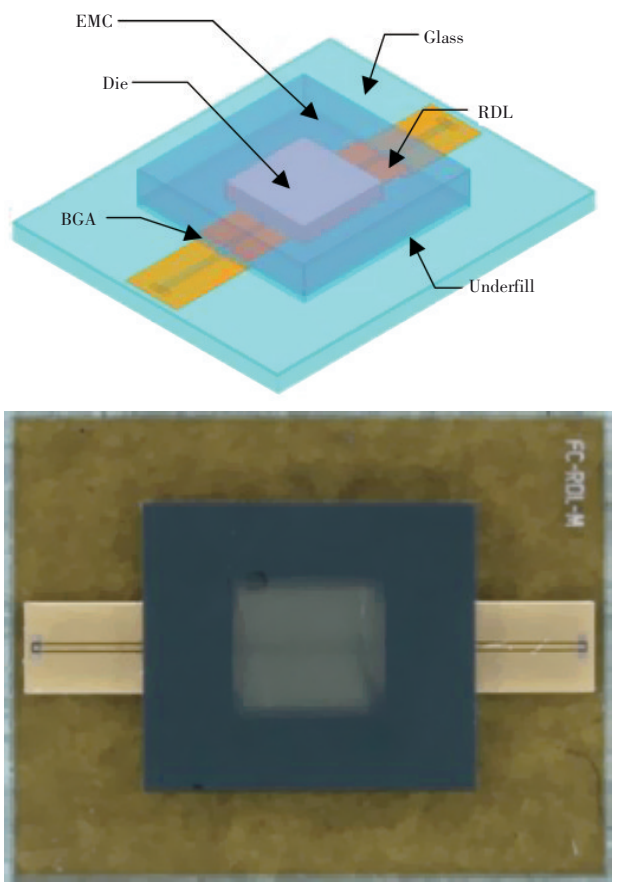

▲ **Figure 4. 3D stacked coplanar waveguide (CPW) transfer structure and photos.**

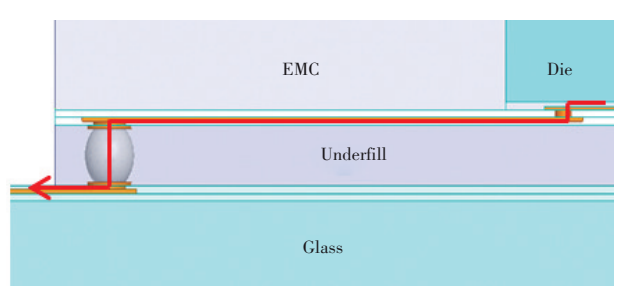

▲ **Figure 5. Transmission path of the RF signal through the package.**

coupling antenna. The glass wafer is used as the radiation patch of the antenna, and the radiation patch is realized by two semicircular patches. The back of the wafer is used as the feed and reflection ground plane of the antenna, and the coupling gap is located directly below the radiation patch, which is used to stimulate the radiation patch. The patch antenna is fed by CPW with terminal open circuit and slot coupling, and the size of CPW is adjusted to make its characteristic impedance 50 Ω, and the function of the coupling gap is to excite the whole patch without an additional gap coupling layer, which makes it easier to integrate with the circuit. It is precisely because of the existence of the coupling gap that the current which originally flows along both sides of the CPW gap on the floor will flow along the edge of the coupling gap, so that the electromagnetic coupling between the CPW and the radiation patch is enhanced. **Fig. 7** is a structural diagram of the slot coupling antenna.

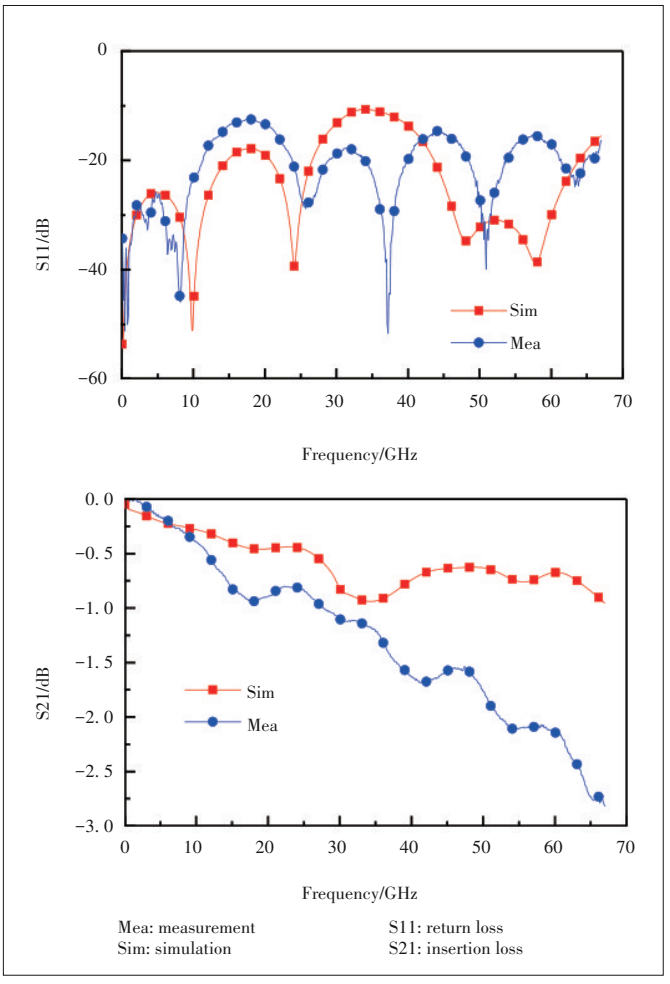

▲ **Figure 6. Comparison between test and simulation results of 3D stacking coplanar waveguide (CPW).**

The electromagnetic simulation software high frequency structure simulator (HFSS) is used to simulate and optimize the slot coupling antenna. After analysis and optimization, the size of the antenna element is 5 mm × 5 mm, the diameter of the two semicircular radiation patches is 1.43 mm, the gap of the two semicircular radiation patches is g=0.196 mm, and the size of the feeder and coupling gap is W=2.8 mm, $W1$=0.2 mm, $L1$=0.07 mm, $L2$=0.615 mm, $g1$=0.025 mm. **Fig. 8** shows the specific structure of the antenna.

The slot coupling antenna is fabricated by wiring the front and back sides of the glass wafer. First, the radiation surface

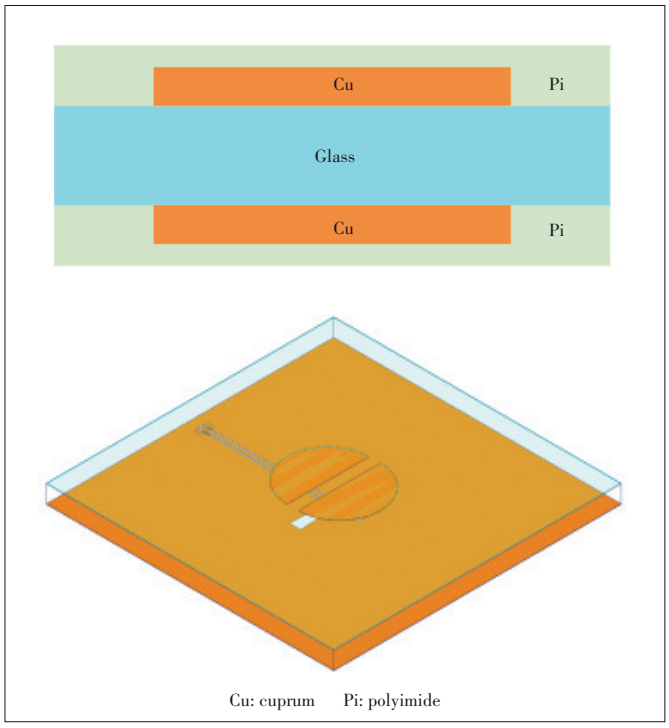

▲Figure 7. Antenna structure and geometry.

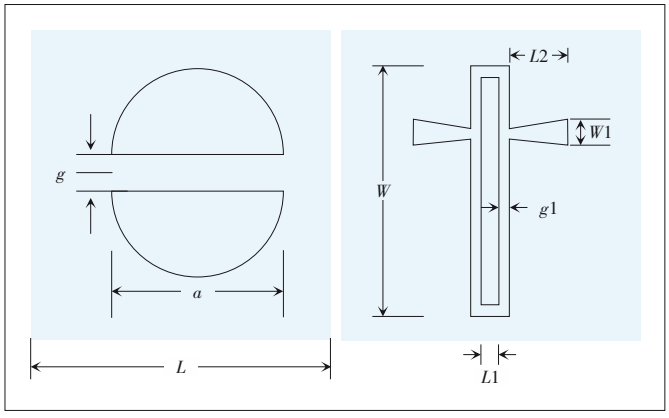

▲Figure 8. Specific structure of the antenna.

of the antenna with 5 μm thick copper is made on the front of the glass wafer, and then it is protected with 10 μm thick polyimide. The CPW feeder and coupling gap are made on the back of the glass wafer, also protected by polyimide, and a rectangular test port is opened on the polyimide layer to leak the copper CPW transmission line.

The structure of the antenna is measured by the high frequency probe table. **Fig. 9** shows the slot coupled antenna photos and test photos. From the measurement results, it can be found that the working frequency of the antenna whose reflection coefficient is less than −10 dB is 56.2 – 63.8 GHz. The difference between the simulation results and the measurement results is mainly attributed to the deviation of the process in the manufacturing process, but the antenna still has the working bandwidth of 7 GHz, which meets the design requirements very well. **Fig. 10** shows the emission coefficient of the antenna.

Fig. 11 shows the radiation pattern of the antenna. We can see that the radiation direction of the antenna is directly above the radiation patch, which is very suitable for the stacking integration of RF microsystem and antenna. The top of the 3D stack integration is used for the manufacture of transceiver an-

▲Figure 9. Slot coupled antenna photo and test photo.

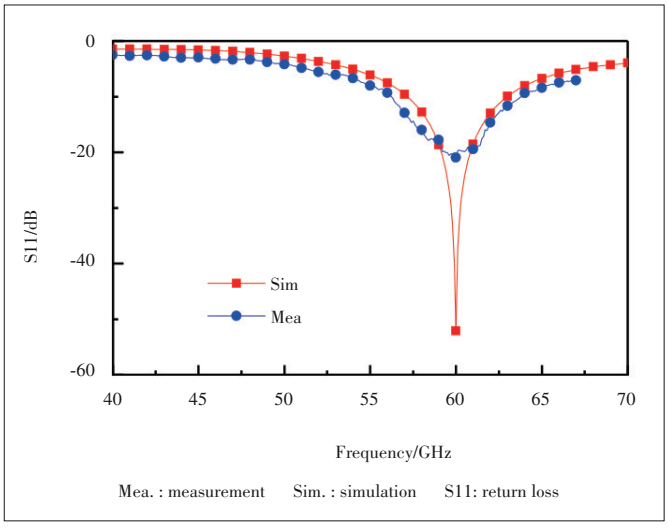

▲Figure 10. Reflection coefficient of antenna.

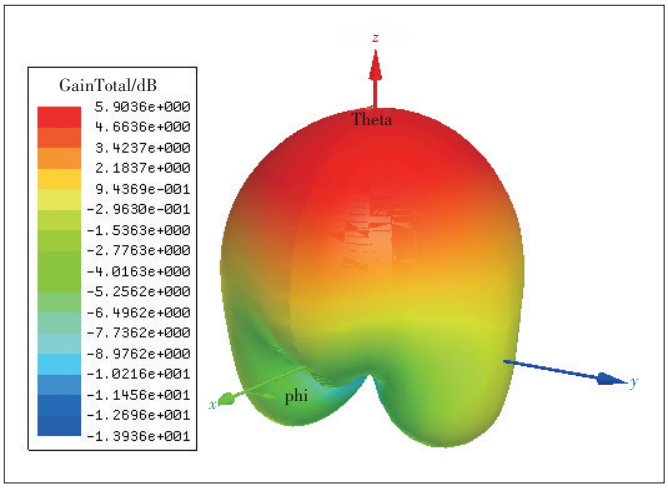

▲Figure 11. Radiation pattern of antenna.

tennas and the bottom is used for the integration of RF chips.

The gain of the antenna is higher than 5.5 dB in the whole working bandwidth and has the maximum gain of 6 dB in 59.8 GHz. And it has a good directionality. **Fig. 12** shows the simulation results of antenna gain in the working bandwidth.

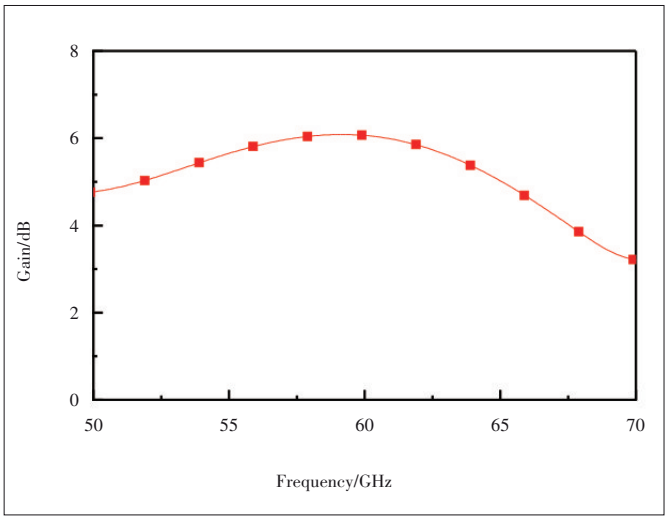

▲**Figure 12. Simulation results of antenna gain in working bandwidth.**

4 Integration of RF Microsystem and Antenna

4.1 Architecture of AiP

In this paper, a specific packaging prototype is made for a 5G communications equipment. It consists of 9 chips and a 64-unit antenna array, including 3 low power RF chips, 2 through silicon via (TSV) transfer chips and 4 high-power chips. The TSV transfer chip is used to realize vertical signal transmission. **Fig. 13** is a schematic diagram of the structure of a 3D fan-out RF microsystem and antenna integrated prototype.

The architecture of AiP is depicted in **Fig. 14.** The RF module demonstrates a multi-layer structure, with antenna and chip layers stacked vertically, and at the very top of the module, the antenna patch array as well as the feeding structure is fabricated on the glass substrate for Tx/Rx channels. As the kernel part, high power chips are embedded in the fan-out (FO) module and interconnected with RDL and TSV structures to establish the transceiver sections; additionally the lower power chips are attached beneath as the signal processing section, thus the solder balls can be arranged on the bottom side as in/out ports. The whole module can be soldered on the system board as an RF transceiver.

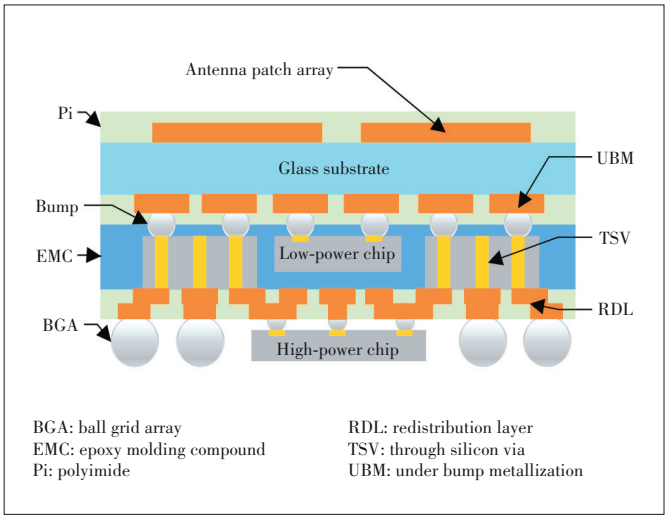

▲**Figure 13. Architecture of integrated prototype of 3D fan-out RF microsystem and antenna.**

4.2 Fabrication Process of AiP

The integration of RF microsystem and antenna is realized by a new wafer-level 3D fan-out packaging process, different from the traditional 3D stacking packaging. In this paper, a permanent bonding process of resin wafer and glass wafer is adopted, and the BGA welding process is avoided between the two-layer wafers, which is very important for the requirement of low loss of RF devices. The interconnection system of RF devices and antennas is directly realized by RDL process. The wafer-level packaging technology takes the wafer as the processing object and carries out the packaging process directly on the wafer, which has high machining accuracy and consistency, and its wiring accuracy can reach 1 μm. The RF transmission loss of wafer-level packaging verified in the first section above shows that the transmission loss of RF interconnection is very small, which will be very conducive to the integration of RF microsystems and antennas. **Fig. 15** shows the packaging process of the 3D fan-out RF microsystem used in this paper.

The specific fabrication process of the RF micro-system and antenna integrated process prototype is as follows. First, a

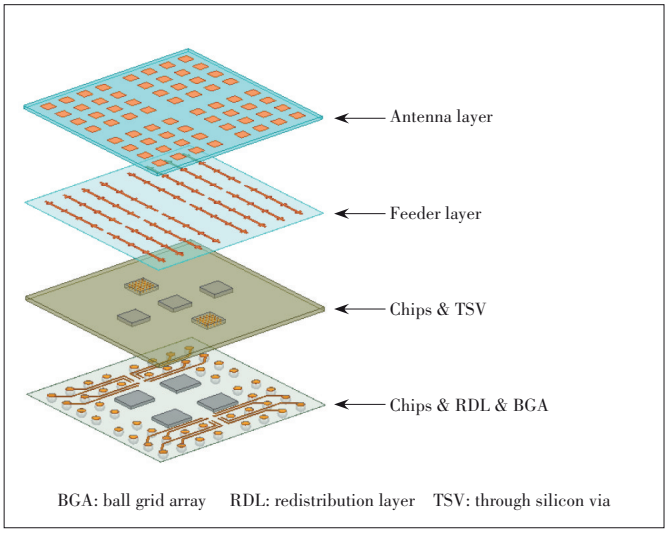

▲**Figure 14. 3D fan-out RF microsystem.**

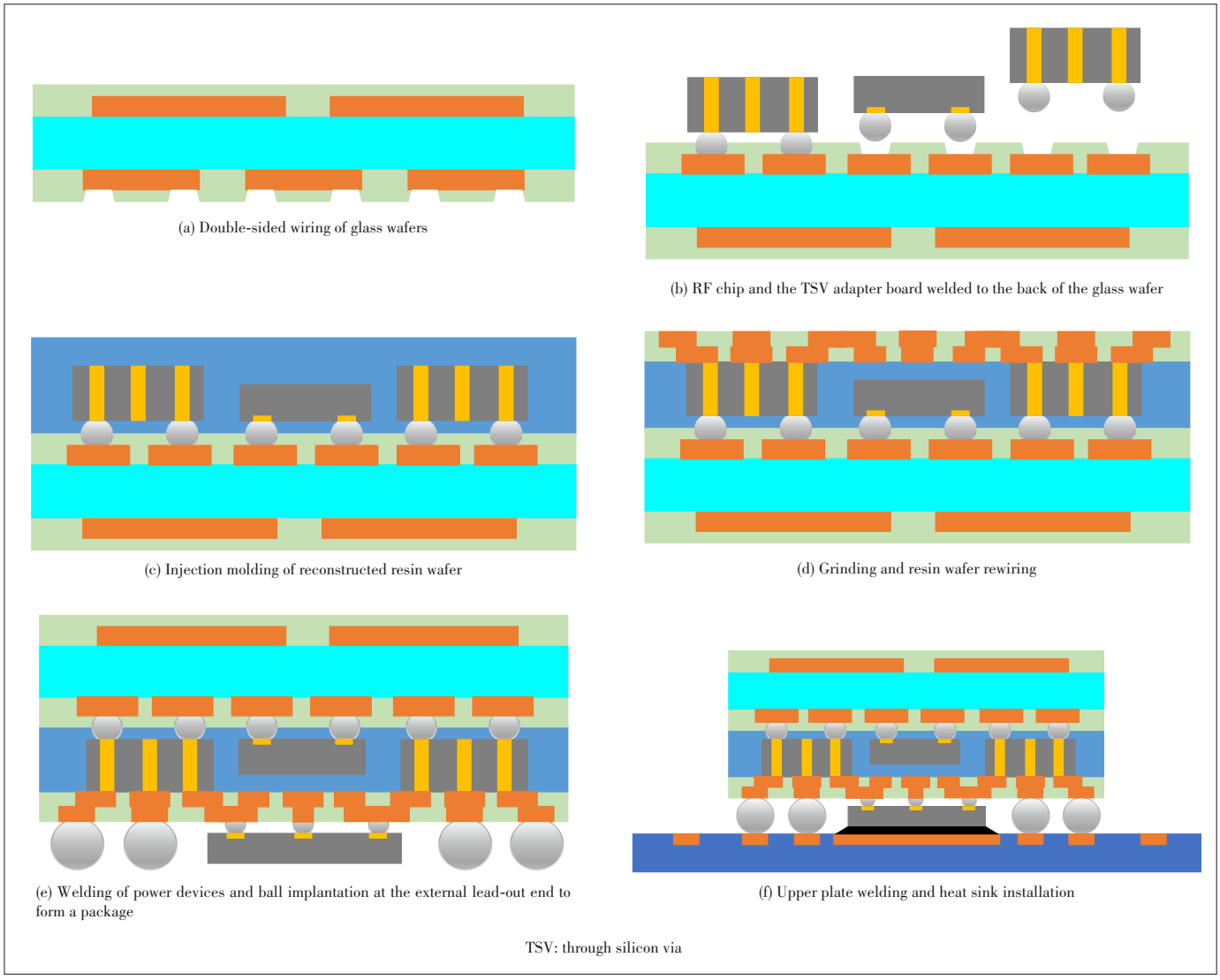

▲**Figure 15. RF microsystem integration process.**

wiring layer and a passivation layer are formed successively on the front and the back of the glass wafer, and the passivation layer is opened on the back of the glass wafer. The TSV transfer chip, the filter and the antenna tuner chip with bump are flip-welded to the opening of the passivation layer on the back of the glass wafer. **Fig. 16** shows a process photo of five chips flip-flopped to the back of the glass wafer.

And then the components such as the TSV transfer chip, the filter and the antenna tuner are coated with coating material to form a reconstructed new wafer carrier, the back of which is thinned to expose the copper column welding disc surface of the TSV adapter plate, and a wiring layer, a passivation layer and a UBM layer are formed on its back. Then the power amplifier, low noise amplifier, transceiver control chip, power management chip and other components are soldered to the UBM layer on the back of the reconstructed new wafer. Solder ball bumps are grown at the UBM layer on the back of the reconstructed wafer carrier to form the final package. The process prototype of the integration of 3D fan-out RF microsystem and antenna is shown in **Fig. 17**.

The integrated packaging process scheme of RF microsystem and antenna has the following advantages:

(1) The glass wafer and the resin wafer are bonded together, and there is no need to untie them in subsequent processing and use, which effectively solves the warping problem of the reconstructed wafer and improves the reliability of the product. At the same time, the integration of this process is also promoted.

(2) The processing technology of welding the chip assembly to the glass wafer and then wrapping it with coating material can effectively avoid the chip offset problem caused by the liquefaction flow of coating material and curing process in the traditional coating forming process, and the processing precision is higher. Radio frequency signal transmission loss is lower.

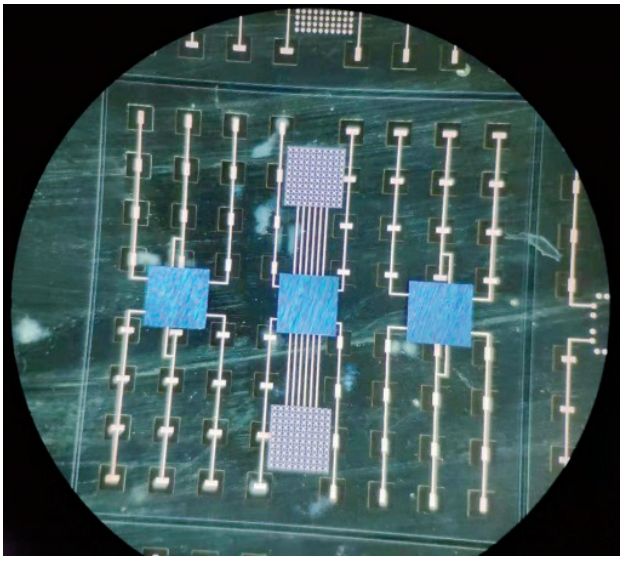

▲Figure 16. Chips welded to the back of the glass wafer.

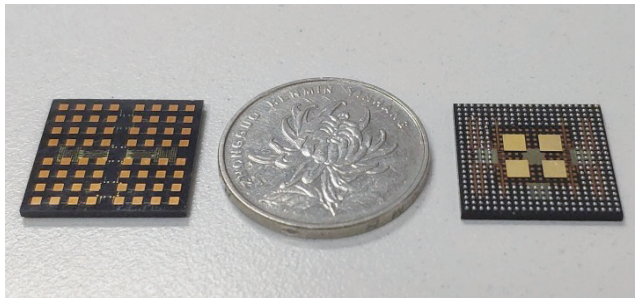

▲Figure 17. Process prototype of 3D fan-out RF microsystem.

(3) With the technology of wiring on the back of the glass wafer and then reconstructing the wafer with cladding, the double-sided wiring of the reconstructed wafer can be effectively realized, the complex temporary bonding process can be avoided, and the yield and reliability of the product can be improved, thus reducing the difficulty of product processing.

(4) In the final package, the low-power chip assembly is embedded in the coating material, and the high-power chip assembly is welded outside the coating material, which can effectively solve the heat dissipation problem of the high-power chip, and when finally on the board, the back of the high-power chip is coated with a thermal conductive material to connect the chip to the heat dissipation metal surface of the substrate to further improve the heat dissipation performance of the package.

5 Conclusions

In this paper, with 3D fan-out wafer-level rewiring technology, CPW planar transmission lines and stacked CPW transmission structures are fabricated, and the RF transmission performance of CPW is verified. Through the test of CPW transmission line by RF millimeter wave probe, the RF transmission loss of glass wafer in the range of 0 – 67 GHz is obtained. The results show that the RF transmission loss of the glass wafer is only 0.26 dB/mm in 60 GHz, and the loss introduced by the fan-out package is also very small, which indicates that the glass wafer can be used as the packaging substrate of RF devices. Then a slot coupling antenna for 5G communications is fabricated on a 12-inch glass wafer. The antenna works at 56.2 GHz and 63.8 GHz, and the maximum gain of the antenna can reach 6 dB within the working bandwidth. On this basis, an integrated prototype of 3D fan-out RF microsystem and antenna for 5G communications is designed and manufactured, and the prototype is fabricated through the wafer-level fan-out packaging process platform. The process of permanent bonding between the glass wafer and the resin wafer is adopted, and the stacking process of the glass wafer and the resin wafer is avoided in the implementation process. In this way, the package has higher structural strength, higher reliability, less warping and lower process complexity, and shortens the processing cycle. Through the above conclusions, the effectiveness of glass wafer as RF device packaging is verified, and a feasible integrated solution of 3D fan-out micro-system and antenna is provided for 5G communications.

References

[1] ALHENAWY M, SCHNEIDER M. Antenna-in-package (AiP) in mm-wave band [J]. International journal of microwave and wireless technologies, 2013, 5(1): 55 – 64. DOI:10.1017/s1759078712000815

[2] JIN C, SEKHAR V N, BAO X Y, et al. Antenna-in-package design based on wafer-level packaging with through silicon via technology[J]. IEEE transactions on components, packaging and manufacturing technology, 2013, 3(9): 1498 – 1505. DOI:10.1109/tcpmt.2013.2261855

[3] WATANABE A, LIN T H, RAJ P M, et al. Leading-edge and ultra-thin 3D glass-polymer 5G modules with seamless antenna-to-transceiver signal transmissions [C]//IEEE 68th Electronic Components and Technology Conference (ECTC). San Diego, USA: IEEE, 2018. DOI:10.1109/ectc.2018.00304

[4] ZHANG Y P, MAO J F. An overview of the development of antenna-in-package technology for highly integrated wireless devices [J]. Proceedings of the IEEE, 2019, 107(11): 2265 – 2280. DOI:10.1109/jproc.2019.2933267

[5] FISCHER A, TONG Z Q, HAMIDIPOUR A, et al. A 77 GHz antenna in package [EB/OL]. (2011-06-22)[2020-12-12]. https://ieeexplore.ieee.org/document/6101048

[6] TSAI C H, HSIEH J S, LIU M, et al. Array antenna integrated fan-out wafer level packaging for millimeter wave system applications [C]//IEEE International Electron Devices Meeting. Washington, USA: IEEE, 2013. DOI: 10.1109/iedm.2013.6724687

[7] CHANG C C, CHENG W K, LIN C C. Fully integrated 60 GHz switched-beam phased antenna array in glass-IPD technology [J]. Electronics Letters, 2015, 51 (11): 804 – 806. DOI: 10.1049/el.2015.0891

[8] LIU D X, GU X X, BAKS C W, et al. Antenna-in-package design considerations for ka-band 5G communication applications[J]. IEEE transactions on antennas and propagation, 2017, 65(12): 6372 – 6379. DOI: 10.1109/tap.2017.2722873

[9] ZHANG T, LI L M, XIE M, et al. Low-cost aperture-coupled 60-GHz-Phased array antenna package with compact matching network [J]. IEEE Transactions on

Antennas and Propagation, 2017, 65(12): 6355 – 6362. DOI: 10.1109/tap.2017.2722867
[10] LIU D X, ZHANG Y P. Integration of array antennas in chip package for 60-GHz radios [J]. Proceedings of the IEEE, 2012, 100(7): 2364 – 2371. DOI: 10.1109/jproc.2012.2186101
[11] ZHANG Y P, LIU D X. Antenna-on-chip and antenna-in-package solutions to highly integrated millimeter-wave devices for wireless communications [J]. IEEE transactions on antennas and propagation, 2009, 57(10): 2830 – 2841. DOI: 10.1109/tap.2009.2029295
[12] ZHU L, MELDE K L, PRINCE J L. A broadband CPW-to-microstrip via-less transition for on wafer package probing applications. [C]//IEEE Electrical Performance of Electrical Packaging. Princeton, USA: IEEE, 2003: 75 – 78. DOI: 10.1109/epep.2003.1250003
[13] ISHIBASHI D, NAKATA Y. Planar antenna for terahertz application in fan out wafer level package [J]. International symposium on microelectronics, 2017, 2017(1): 599 – 603. DOI: 10.4071/isom-2017-tha43_115

Biographies

XIA Chenhui (smartxvip@163.com) received the master's degree from Nanjing University of Science and Technology, China. He joined China Electronics Technology Group Corporation (CETC) 58 in 2018 and has been engaged in the research of RF micro-electro-mechanical system and RF advanced packaging technology, among which the project group of "flexible Micro/Nano Reconfigurable Manufacturing Technology" won the second prize for scientific and technological progress. At present, his main interests focus on the integration of RF antennas and the integrated packaging technology of heterogeneous chip microsystems. He has published four papers.

WANG Gang received the doctor's degree from Beijing Institute of Technology, China. He joined CETC 58 in 2019 and has been engaged in RF MEMS and micro-system technology research. His current interests include sensor integration and 3D heterogeneous integration technology research. He has published 7 EI and SCI papers.

WANG Bo received the master's degree from University of Electronic Science and Technology of China in 2008. He joined CETC 58 in 2017 and has been engaged in the research and development of wafer-level packaging and fan-out integration technology.

MING Xuefei received the master's degree from The Hong Kong University of Science and Technology, China. Since 2010, he has joined CETC 58, mainly engaged in advanced packaging research work. Ten papers were published, two of which were searched by EI, and won the Science and Technology Progress Award of the Group and the State Administration of Science, Technology and Industry for National Defense for three times.

From Page 11

JIANG Jiachun received his bachelor degree in electronics science and technology from Donghua University of Technology, China in 2018. He is pursuing his master degree in electronics and information engineering at Shenzhen University, China.

ZHANG Long received the B.S. and M.S. degrees in electrical engineering from Huazhong University of Science and Technology, China in 2009 and 2012, respectively and the Ph.D. degree in electronic engineering from the University of Kent, UK in 2017. He is currently an assistant professor with the College of Electronics and Information Engineering, Shenzhen University, China. His current research interests include circularly polarized antennas and arrays, mm-wave antennas and arrays, phased arrays, tightly coupled arrays, and reflect arrays. He is a recipient of the Shenzhen Overseas High-Caliber Personnel Level C ("Peacock Plan Award" C).

LI Wenting received the B.S. degree in electronic information engineering and the M.S. degree in electromagnetic field and microwave technology from Northwestern Polytechnical University, China in 2011 and 2014, respectively, and the Ph.D. degree in electronic engineering from the University of Kent, UK in 2019. He is currently an assistant professor with the College of Electronics and Information Engineering, Shenzhen University, China. His current research interests include reflectarray antennas, reconfigurable antennas, circularly polarized antennas, and multibeam antennas.

WONG Sai-Wai received the B.S. degree in electronic engineering from the Hong Kong University of Science and Technology, China in 2003, and the M.Sc. and Ph.D. degrees in communication engineering from Nanyang Technological University, Singapore in 2006 and 2009, respectively. In 2016, he was a visiting professor with the City University of Hong Kong, China. Since 2017, he is a full professor with College of Electronics and Information Engineering, Shenzhen University, China. His current research interests include RF/microwave circuit and antennas design. Dr. WONG was a recipient of the New Century Excellent Talents in University (NCET) Award and the Shenzhen Overseas High-Caliber Personnel Level C ("Peacock Plan Award" C).

DENG Wei received the B.S. and M.S. degrees in electronic engineering from the University of Electronic Science and Technology of China in 2006 and 2009, respectively, and the Ph.D. degree in electronic engineering from the Tokyo Institute of Technology, Japan in 2013. From 2013 to 2014, he was a post-doctoral researcher with the Tokyo Institute of Technology. From 2015 to 2019, he was with Apple Inc., Cupertino, USA, working on RF, mm-wave, and mixed-signal IC design for wireless transceivers and Apple A-series processors. Since 2019, he has been a faculty member with the Department of Microelectronics and Nano Electronics, Institute of Microelectronics, Tsinghua University, China. He has authored or coauthored over 80 IEEE journal and conference articles. His research interests include RF, mm-wave, terahertz, and mixed-signal integrated circuits and system for wireless communications, radars, and imaging systems.

CHI Baoyong received the B.S. degree in microelectronics from Peking University, China in 1998, and the Ph.D. degree from Tsinghua University, China in 2003. From 2006 to 2007, he was a visiting assistant professor with Stanford University, USA. He is currently a full professor and the deputy director with the Institute of Microelectronics, Tsinghua University. He has authored over 140 academic articles and two books, and holds more than 20 patents. His current research interests include RF/mm-wave integrated circuit design, analog integrated circuit design, and monolithic wireless transceiver chips for radar and communications. Dr. CHI has been a TPC Member of A-SSCC since 2005.

Electromagnetic Simulation with 3D FEM for Design Automation in 5G Era

Lukasz BALEWSKI[1], Michal BARANOWSKI[2], Maciej JASINSKI[2], Adam LAMECKI[1,2], Michal MROZOWSKI[2]

(1. EM Invent, Gdansk 80-172, Poland;
2. Faculty of Electronics, Telecommunications, and Informatics, Gdansk University of Technology, Gdansk 80-233, Poland)

Abstract: Electromagnetic simulation and electronic design automation (EDA) play an important role in the design of 5G antennas and radio chips. The simulation challenges include electromagnetic effects and long simulation time and this paper focuses on simulation software based on finite-element method (FEM). The state-of-the-art EDA software using novel computational techniques based on FEM can not only accelerate numerical analysis, but also enable optimization, sensitivity analysis and interactive design tuning based on rigorous electromagnetic model of a device. Several new techniques that help to mitigate the most challenging issues related to FEM based simulation are highlighted. In particular, methods for fast frequency sweep, mesh morphing and surrogate models for efficient optimization and manual design tuning are briefly described, and their efficiency is illustrated on examples involving a 5G multiple-input multiple-output (MIMO) antenna and filter. It is demonstrated that these new computational techniques enable significant reduction of time needed for design closure with the acceleration rates as large as tens or even over one hundred.

Keywords: design by optimization; electronic design automation; fast frequency sweep; interactive design tuning; mesh morphing

DOI: 10.12142/ZTECOM.202003007

https://kns.cnki.net/kcms/detail/34.1294.TN.20200916.1051.002.html, published online September 16, 2020

Manuscript received: 2020-06-02

Citation (IEEE Format): L. Balewski, M. Baranowski, M. Jasinski, et al., "Electromagnetic simulation with 3D FEM for design automation in 5G era," *ZTE Communications*, vol. 18, no. 3, pp. 42 - 48, Sept. 2020. doi: 10.12142/ZTECOM.202003007.

1 Introduction

5G technology is going to revolutionize the next decade, allowing wireless connectivity to penetrate the industrial world and society. Huge new markets will open for business, which are expected to play an important role in economy recovery and growth, offering new business opportunities and changing our lives. Smart cities, factories, autonomous vehicles, intelligent infrastructure, electric grids, massive machine-to-machine communications are just a few examples of the 5G application scenarios where billions of devices will be connected in radio networks. With 5G infrastructure and technology, companies will provide new mobile services and offer new wireless products with unprecedented capabilities. To meet the demands for high data throughput, low latency, low power consumption, quality of service and safety simultaneously, wireless devices will have to fulfill stringent system and regulatory requirements that can only be satisfied by carefully engineered hardware. Engineers will have to overcome enormous technical challenges and this will not be possible without new generation of electronic design automation (EDA) software that is capable of addressing these challenges with accuracy and speed not seen before. The core of 5G is wireless

This work was supported in part by the Electromagnetic Design of Flexible Sensors Project under Grant No. POIR.04.04.00-00-1DC3/16-00, which is carried out within the Team-Tech Program of the Foundation for Polish Science co-financed by the European Union under the European Regional Development Fund, Smart Growth Operational Program 2014 - 2020.

connectivity, so EDA software for fast electromagnetic analysis, which is necessary for accurately simulating 5G antennas and radio chips, will be essential for timely delivery of 5G innovations to market.

2 Simulation Challenges and Solutions

RF circuits cannot be designed easily by using lumped element models. The size of each element and wavelength and electromagnetic effects, such as dispersion, radiation, conductor and dielectric loss, and parasitic coupling have to be considered. EDA simulates the behavior of a circuit by numerically solving Maxwell's equations and facilitate accurate results with these effects are taken into account. This is not a trivial task and often requires substantial computer resources. To address the challenges related to electromagnetic design, software tools have to use state-of-the-art numerical algorithms[1-7] that speed up simulations and allow designers to find the solution that meet stringent specifications.

2.1 Frequency Sweeps

To get an idea of challenges associated with computer aided design of RF circuits for the fifth generation (5G) mobile communications, let us consider an antenna, which is a basic element of any handheld wireless device. To meet the requirements for higher data transfer rate, 5G communications systems have to use multiple-input multiple-output (MIMO) technology. Because a high throughput is essential in 5G, massive MIMO antenna systems are necessary and designed for any handheld devices. On the other hand, different countries have allocated different parts of the spectrum for 5G service. As a result, MIMO antennas for consumer applications have to cover more than one band. Therefore, numerical simulation of a broadband or multi-band MIMO antenna can be very lengthy. To illustrate this, let us consider modelling of a 4 × 2 broadband antenna for a smartphone proposed in Ref. [8]. As shown in **Fig. 1**, the antenna array consists of eight radiating elements, each fed by a microstrip line with a tuning stub. The antenna array operates in 3.3 GHz to 6 GHz and provides high isolation between elements.

To analyze the antenna, we will use the finite-element method (FEM), which is amongst the most powerful numerical modelling techniques, for solving partial differential equations often used in computational electromagnetics software for high-frequency electromagnetic field simulations (**Table 1**).

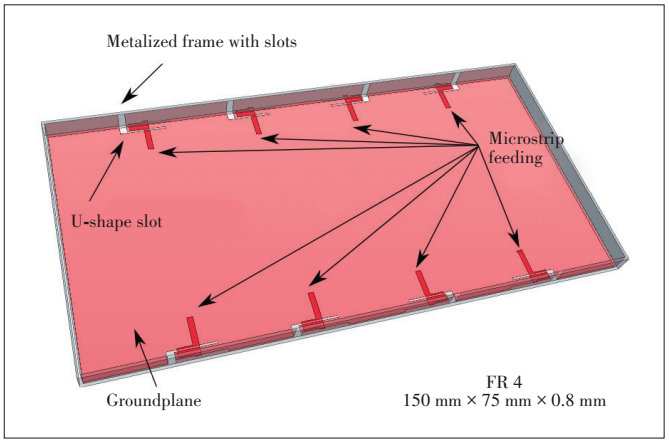

▲ **Figure 1. Simulation of an 8-element multiple-input multiple-output (MIMO) antenna for a 5G terminal[8].**

▼**Table 1. Examples of commercial software or modules in software packages for electromagnetic EDA with a computational kernel based on FEM**

Software/FEM Module (Company)	Features
Feko (Altair HyperWorks)	· Several solvers (including FEM) integrated in one software package · Fast frequency sweep (interpolating) · Scripting · Several optimization procedures
HFSS (Ansys)	· Optimization (separate module) · Fast frequency sweep (interpolating or model order reduction) · Interactive design tuning (separate module)
COMSOL Multiphysics/RF Module (COMSOL)	· Several optimization techniques (separate module) · Fast frequency sweep using Padé interpolation (asymptotic wave evaluation method)
SIMULIA/CST Studio Suite/Frequency Domain Solver (Dassault Systèmes)	· Several solvers (including FEM) integrated in one software package · Optimization with movable mesh · Fast frequency sweep (adaptive sampling or model order reduction) · 3D filter CAD (separate module)
InventSim (EM Invent)	· Fast frequency sweep (MOR or interpolating) · Optimization with deformable mesh and MOR · Filter synthesis and 3D shape optimization – integrated · Mixed precision solver · Interactive design tuning (integrated)
PathWave EM Design (EMPro) (Keysight Technologies)	· Adaptive fast frequency sweep (interpolating) · Integration with ADS

ADS: Advanced Design System
CAD: computer aided design
EDA: electronic design automation
FEM: finite-element method
HFSS: High Frequency Structure Simulator
MOR: model order reduction

FEM uses a volumetric mesh where the 3D space is divided into small tetrahedral sub-regions (elements). Field in each tetrahedron is represented by a sum of simple (linear, quadratic or cubic) local functions. Field equations are enforced within each element and across all elements. This results in a large system of linear equations that is then numerically solved at the desired frequency. The number of equations is very large (often in the order of millions) so the solution is time consuming. **Fig. 2** shows the results of the simulation of the antenna using InventSIM EDA software[9] for the frequency band from 2 GHz to 7 GHz. The plot shows selected scattering parameters, computed characteristics and the results of measurements reported in Ref. [8]. It is seen that the agreement is good.

Let us now have a closer look at the simulation runtime. In the basic simulation scenario, called discrete sweep, a certain number of frequency points (N_f), uniformly distributed in the band of interest, are selected, and FEM equations are solved at these points. The runtime needed to complete the simulations depends on the number of frequency points,

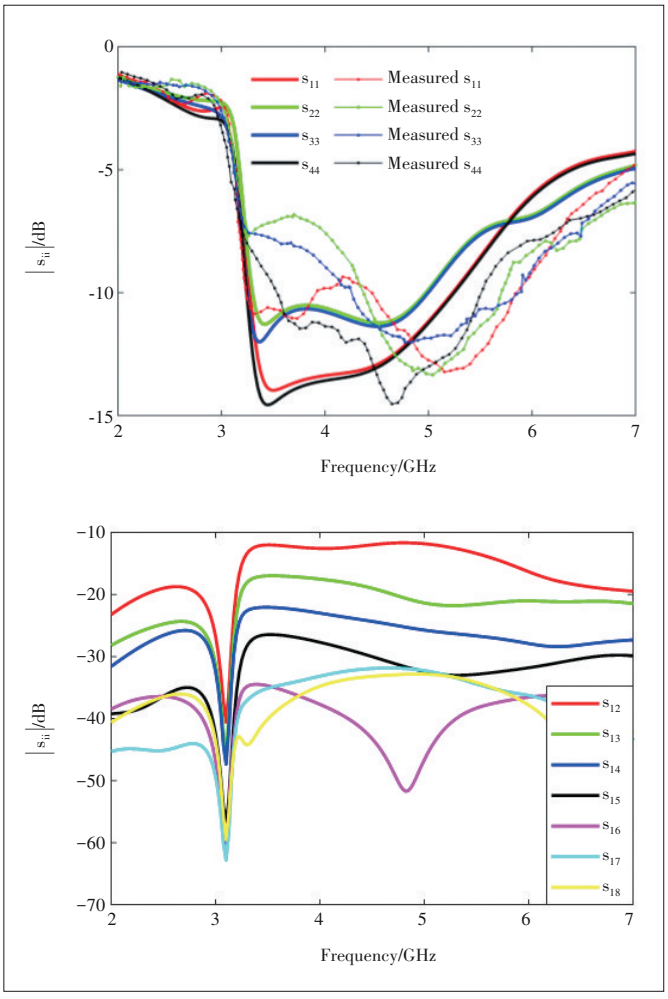

▲Figure 2. Selected scattering parameters (S_{ij}) of multiple-input multiple-output (MIMO) antenna.

mesh density and the order of local functions for tetrahedra. In the case of our MIMO antenna, we selected N_f =201 and the second order interpolation within each tetrahedron. The runtime for a coarse mesh (118 thousand tetrahedra) was 20 minutes, while for the mesh approximately 3.3 times finer (390 thousand tetrahedra), it was 3 hours and 25 minutes. The runtimes are given for a server with two Intel Xeon Gold 6136 processors and 576 GB RAM installed. This is certainly not attractive for a designer to wait for almost 3.5 hours to see the results. If the mesh is further refined, by a factor of three, which may sometimes be needed for getting very accurate results, the number of tetrahedra grows to 1.185 million and the runtime for 201 frequency points increases to over 16 hours. Such long computing time would make FEM simulations unattractive. This is why all EDA tools presented in Table 1 offer a feature called a fast frequency sweep, which enables much faster broadband response. With the interpolating sweep, one of the two most common used sweep approaches, the solution is found at a small number of frequency points and the response between these points is interpolated from them. The points for interpolation are selected automatically. One disadvantage of this approach is that while the scattering characteristics can be calculated between the sampling frequencies, the electromagnetic field can be computed only for the nodes. This disadvantage can be avoided in the fast frequency sweeps using model order reduction algorithms[4-5], [7]. In a nutshell, the reduced order model is a mathematical technique that constructs a cheap to evaluate model of a dynamical system by finding a compact set of vectors that allow to represent the electromagnetic field at any frequency within a limited frequency band. This is possible since the electromagnetic field does not change very rapidly from one frequency point to another, so in fact it can be represented as a linear combination of frequency-independent field patterns defined in the entire computational space, called basis vectors. What change with frequency are the amplitudes of basis vectors and these amplitudes can be computed very fast. The acceleration is impressive; for instance, it took InventSIM 13 minutes to compute the response of the same 4 × 2 MIMO antenna at the 201 frequency points using wideband model order reduction algorithm for the moderately dense mesh consisting of 390 thousand tetrahedra, which is 15 times faster than the original discrete sweep. For the finest mesh of 1.185 million tetrahedra, the speedup is even larger. For this case the computations are completed in 44 minutes rather than 16 hours (21 times faster). **Table 2** provides detailed data for the simulations and the runtimes for the interpolating sweep.

It is evident that a good fast frequency sweep technique in an EDA software is crucial for enabling engineers to design and validate the performance of antennas and RF and microwave components. An optimal design is hard to achieve without fast frequency sweep.

▼Table 2. Runtime for wideband simulation of a 4×2 MIMO antenna for 5G and three mesh densities

Number of Tetrahedra	Matrix Size	Direct Sweep Time/s (201 freq. points)	Interpolating Sweep Time/s	Fast Frequency Sweep (MOR) Time/s
118 367	727 514	1 095	181	247
390 136	2 444 052	12 296	2 062	822
1 185 523	7 337 304	58 385.4	8 647	2 692

MIMO: multiple-input multiple-output MOR: model order reduction

2.2 Optimization

Often the simulation shows that the designed structure does not fulfil the desired specification. The way electromagnetic waves interact with objects, which determines the response of the circuits, depends on their shape. To ensure that the specifications are met, the geometry of antennas and microwave components in RF chips has to be altered. To achieve good performance, optimization algorithms will be applied. This requires a number of electromagnetic simulations that are performed in the optimization loop with design parameters as optimization variables. In each iteration the geometry is altered (dimensions change) and numerical analysis is then carried out from scratch. Simulations are repeated many times until the response meets the specifications. The number of iterations depends on the optimization method used and on the quality of the initial design. It is evident that the challenge related to long computing time becomes much more severe when it comes to optimization.

A new generation of FEM EDA tools can address the challenges not only via fast frequency sweeps, but also by treating iterations as a part of the entire design process in which the geometry gradually evolves rather than as a set of independent simulations for different geometries. In this framework, iterations are connected via the mesh and the workflow is arranged so that the same mesh is used throughout optimization rather than being generated anew each time a geometry is modified. To enable this, the coordinates of each mesh node change continuously as the values of the design variables are modified in an optimization process. This technique is known as mesh deformation or mesh morphing[10 - 12] and has been found to greatly improve the efficiency of optimization[4].

A four-pole microwave filter is optimized to illustrate the implementation of FEM-based optimization and the significance of a fast frequency sweep using reduced order model and mesh morphing. The geometry of the filter is shown in **Fig. 3**. The goal is to achieve an equiripple response in a certain bandwidth, and five geometrical variables could be modified to reach this goal. The design variables are the heights of posts in the coupling windows and the heights of the posts in the resonant cavities. Full details related to the geometry and specifications are provided in Ref. [3], where several gradient-based optimization techniques were discussed using FEM and the runtime for simulations was provided. The approaches considered in Ref. [3] are the direct EM optimization using sequential nonlinear programming (SNLP), which is one of the optimization techniques available in a commercial tool for electromagnetic design High Frequency Structure Simulator (HFSS), direct EM optimization using MATLAB's fminimax procedure with the quasi-Newton method for mesh deformation, and the new formulation of Newton's method with constraints (the Lagrangian method) with mesh deformation developed specifically for EM optimization. The number of iterations and runtime used for these three approaches with two starting points are compared in **Table 3**. Besides, in the last two rows of Table 3, we add the results obtained by InventSIM and its implementation of mesh deformation and fast frequency sweep using reduced order modelling, with MATLAB's

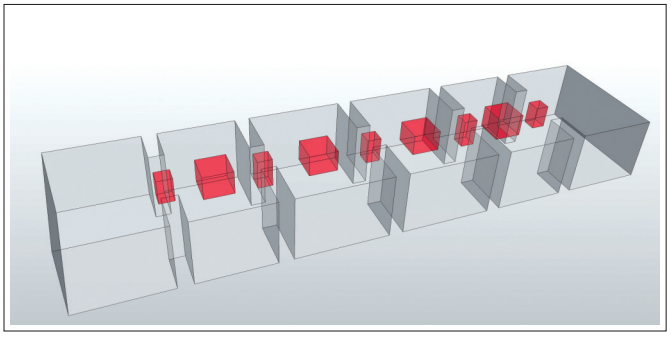

▲Figure 3. Structure of the four-pole waveguide filter[3] with five geometrical variables used for direct EM design optimization.

▼Table 3. Comparison of the number of iterations and runtime of different methods for FEM-based optimization of a four-pole waveguide filter

Method	Good Starting Point		Bad Starting Point	
	No. of Iterations	Total Runtime	No. of Iterations	Total Runtime
HFSS's SNLP without mesh deformation[3]	71	17.8 h	135	33.8 h
Quasi-Newton with mesh deformation[3]	31	8.2 h	65	17.1 h
Quasi-Newton with Lagrangian method and mesh deformation[3]	9	2.7 h	24	7.2 h
Quasi-Newton using InventSim FEM solver and mesh deformation	17	39 min 16 s	30	1.5 h
InventSim generalized Chebyshev filter optimizer with mesh deformation	9	11 min 13 s	14	18 min 43 s

FEM: finite-element method SNLP: sequential nonlinear programming HFSS: High Frequency Structure Simulator

fminimax and a built-in optimizer for general Chebyshev filters. An important observation that can be made from the data given in the table is that there can be huge differences both in the convergence rate and the total time taken by optimization. As seen from the results, mesh deformation has a significant impact on the convergence rate. The number of iterations is much higher for the HFSS that does not offer mesh morphing, than for any other case presented in the paper, where mesh morphing is employed. For a bad starting point, one EDA software tool results in the time needed for the design closure 100 times shorter than another EDA tool.

The optimization of the filter in Ref. [3], even though considered as a challenge for direct EM optimization for most EDA tools based on FEM, is still relatively simple in terms of the number of optimizable parameters; the example considered above involved just five design variables. In practice, the number of geometry variables that have to be considered by an engineer is much larger. In the next example, we consider an interdigital combine filter with 18 design variables. The geometry of the filter is shown in **Fig. 4**. The design variables include 7 tuning screws, 8 lengths between posts, input and output height, and the height of resonators (common for all). No symmetry was assumed and optimization was performed in InventSIM with both mesh morphing and fast frequency sweep enabled. For this example, the FEM matrix had 350 thousand rows and columns, and the optimizer needed 18 iterations and less than 56 minutes to converge from the initial design shown by the red curve in **Fig. 5** to the passband response shown by the blue one in the same figure.

2.3 Interactive Design Tuning

The optimization algorithm is a powerful tool for EDA, but it is time consuming. Moreover, an optimization algorithm itself has no knowledge of the physics governing the operation of a device. It just executes a sequence of steps based on the data provided by a simulator. However, the knowledge-based design is likely to enable an acceptable result much quicker, by which the decisions of what parameters should be adjusted come from the understanding of the operating principle of a circuit or a role of a particular component in shaping the response. A skilled engineer can use his experience to modify certain parameters to improve the performance of the circuit. A very efficient way to do these adjustments is interactive design tuning. The idea is to allow an engineer to continuously change one or more design parameters while monitoring the effect of the changes. In order to realize interactive design tuning, the result of any change should be reflected in the response instantaneously. At first glance it seems impossible for EDA of RF circuits; as we showed in the previous sections, the simulations using full-wave FEM take long time and one has to wait for minutes or even hours before the response can be evaluated and displayed. However, this seemingly impossible real-time interactive tuning can be achieved if a parametric surrogate model is used instead of full-wave simulations to quickly evaluate the response and display the results on the fly each time any design parameter is changed. The surrogate model is constructed from the data computed by the FEM solver at the initial design point. Obviously, the accuracy of the surrogate model is limited and this model is valid only in the neighborhood of the point in the design space where the FEM model was computed. Nevertheless, this accuracy is often sufficient, and what is more, once an engineer is satisfied with the response obtained while manually adjusting the design variables, FEM simulations can be run and the surrogate model updated. As an example, we show the results of interactive tuning of a dielectric resonator filter proposed in Ref. [13] for use in 2 × 2 Doherty power amplifier for a 5G massive MIMO system application. The geometry of the filter is shown in **Fig. 6**.

Following classical synthesis, the filter was simulated in InventSIM and then manually tuned by adjusting seven geometry parameters. Regular FEM simulation for this filter using a fast frequency sweep takes about 150 s. If one runs the interactive tuning, the solver needs additional 21 seconds to set up a surrogate model, so manual tuning with on the fly response

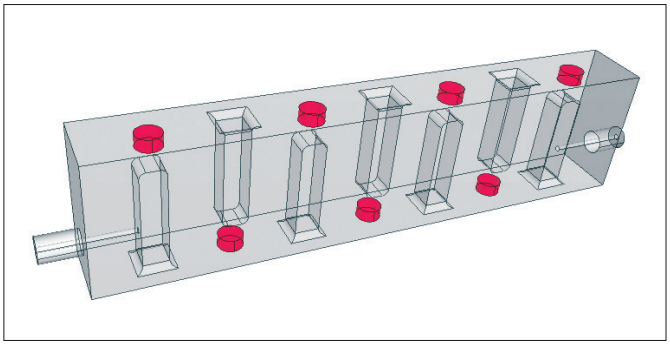

▲**Figure 4. Inline 7th order interdigital filter operating in 5G band 3.4 – 3.6 GHz.**

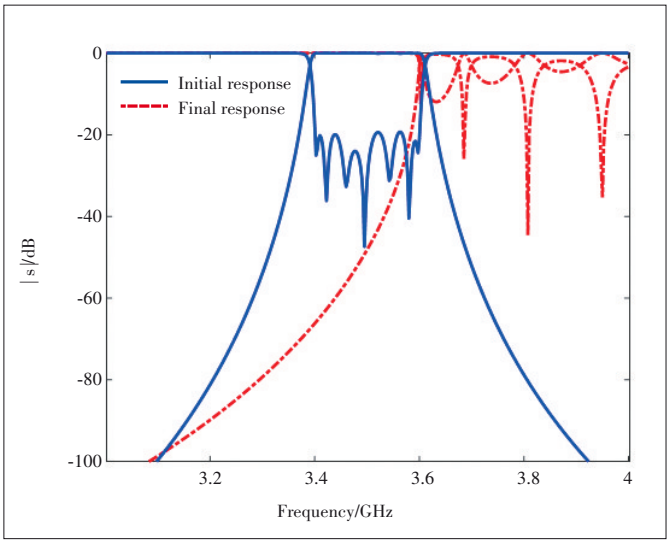

▲**Figure 5. Initial and final response of optimized interdigital filer.**

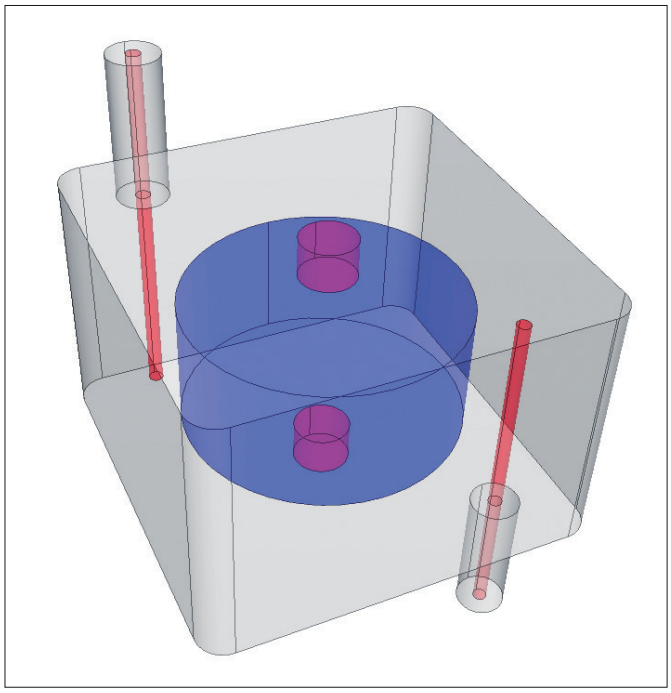

▲ **Figure 6. Single-channel of two-pole dielectric resonator (DR) filter for 5G applications[13].**

display for this example needs less than three minutes of preprocessing.

Table 4 gives the values of the design variables before and after manual tuning. During the interactive tuning, the variables were modified one by one and the characteristics were updated on the fly using the surrogate model. All design variables were altered, most of which were changed by less than 1% – 2% but some changed quite significantly (e.g. the tuning screw). **Fig. 7** shows the initial response computed with FEM (dashed blue curve) while the solid lines shows filter characteristics for final values of design variables, after interactive tuning. The black curve shows the characteristics predicted by surrogate model prediction while the red curve corresponds to the results recomputed with the full-wave FEM solver. It is evident that there is a very good match.

3 Conclusions

Major challenges for electronic design automation tools for 5G solutions have been discussed. Various approaches to address these challenges and speed up the computation time of FEM-based simulation problems have been presented. Fast frequency sweeps, model order reduction, and using mesh morphing in optimization have been shown to give significant reduction of the time needed by EDA software tools to simulate and optimize the performance of antennas and RF passive circuits. The concept of interactive design tuning based on a surrogate model has also been discussed as a good alternative to the optimization process.

▼ **Table 4. Interactive tuning of dual-channel dielectric resonator filter for use in a Doherty power amplifier for 5G massive MIMO system application**

Parameter	Description	Initial Value/mm	Final Value/mm
a	Cavity width, length	25.85	25.94
c	Cavity height	18.44	18.0
D	DR diameter	19.32	19.3
H	DR height	9.47	9.38
X	Distance of coax from cavity wall	4.2	4.18
L	Coax probe length	16.0	16.1
Lp	Tuning screw length	0.28	0.88

DR: dielectric resonator MIMO: multiple-input multiple-output

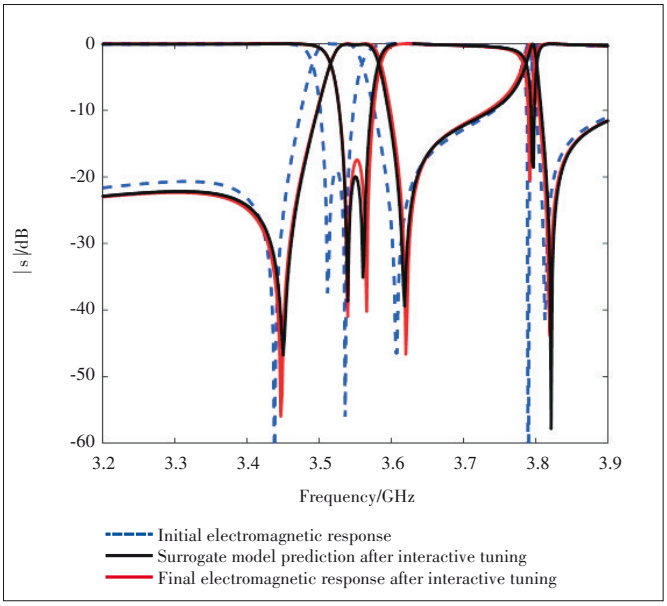

▲ **Figure 7. Example of interactive tuning technique.**

References

[1] ZHANG C, FENG F, GONGAL-REDDY V M, et al. Cognition-driven formulation of space mapping for equal-ripple optimization of microwave filters [J]. IEEE transactions on microwave theory and techniques, 2015, 63(7): 2154 – 2165. DOI: 10.1109/TMTT.2015.2431675

[2] ZHOU B, JIAO D. Direct finite-element solver of linear complexity for large-scale 3-D electromagnetic analysis and circuit extraction [J]. IEEE transactions on microwave theory and techniques, 2015, 63(10): 3066 – 3080. DOI: 10.1109/TMTT.2015.2472003

[3] FENG F, ZHANG J, JIN J, et al. Efficient FEM-based EM optimization technique using combined lagrangian method with Newton's method [J]. IEEE transactions on microwave theory and techniques, 2020, 68(6): 2194 – 2205. DOI: 10.1109/TMTT.2020.2979982

[4] BALEWSKI L, FOTYGA G, MROZOWSKI M, et al. Step on it! Bringing full-wave finite-element microwave filter design up to speed [J]. IEEE microwave magazine, 2020, 21(3): 34 – 49. DOI: 10.1109/MMM.2019.2958165

[5] BALTES R, SCHULTSCHIK A, FARLE O, et al. A finite-element-based fast frequency sweep framework including excitation by frequency-dependent waveguide mode patterns [J]. IEEE transactions on microwave theory and techniques, 2017, 65(7): 2249 – 2260. DOI: 10.1109/TMTT.2017.2679181

[6] CZARNIEWSKA M, FOTYGA G, LAMECKI A, et al. Parametrized local re-

duced-order models with compressed projection basis for fast parameter-dependent finite-element analysis [J]. IEEE transactions on microwave theory and techniques, 2018, 66(8): 3656 – 3667. DOI: 10.1109/TMTT.2018.2842744
[7] FOTYGA G, CZARNIEWSKA M, LAMECKI A, et al. Reliable greedy multipoint model-order reduction techniques for finite-element analysis [J]. IEEE antennas and wireless propagation letters, 2018, 17(5): 821 – 824. DOI: 10.1109/LAWP.2018.2817391
[8] ZHANG X, LI Y, WANG W, et al. Ultra-wideband 8-port mimo antenna array for 5G metal-frame smartphones [J]. IEEE access, 2019, 7: 72273 – 72282. DOI: 10.1109/ACCESS.2019.2919622
[9] LAMECKI A, BALEWSKI L, MROZOWSKI M. An efficient framework for fast computer aided design of microwave circuits based on the higher-order 3D finite-element method [J]. Radioengineering, 2014, 23(4): 970 – 978.
[10] MAHANFAR A, BILA S, AUBOURG M, et al. Mesh deformation techniques for geometrical optimization of microwave devices [C]//IEEE Antennas and Propagation Society International Symposium, Columbus, USA, 2003: 56 – 59. DOI: 10.1109/APS.2003.1219178
[11] LAMECKI A. A mesh deformation technique based on solid mechanics for parametric analysis of high-frequency devices with 3-D FEM [J]. IEEE transactions on microwave theory and techniques, 2016, 64(11): 3400 – 3408. DOI: 10.1109/TMTT.2016.2605672
[12] SELIM M, KOOMULLIL R. Mesh deformation approaches: a survey [J]. Journal of mathematical physics, 2016, 7(2). DOI: 10.4172/2090-0902.1000181
[13] XU J, ZHANG X Y. Dual-channel dielectric resonator filter and its application to doherty power amplifier for 5G massive MIMO system [J]. IEEE transactions on microwave theory and techniques, 2018, 66(7): 3297 – 3305. DOI: 10.1109/TMTT.2018.2829197

Biographies

Lukasz BALEWSKI received his M.Sc. and Ph.D. (with honors) degrees in microwave engineering from Gdansk University of Technology (GUT), Poland in 2003 and 2008, respectively. He works with EM Invent, Poland. His research interests include CAD of microwave devices, filter design, and optimization techniques. He is the co-author of several software tools for microwave filter design.

Michal BARANOWSKI received the B.Sc. degree in electronics and telecommunications from Gdansk University of Technology, Poland in 2020. He is currently pursuing his M.Sc. degree at the Faculty of Electronics, Telecommunications and Informatics at Gdansk University of Technology. His research interests include computational electromagnetics and optimization techniques.

Maciej JASINSKI (maciej.jasinski@pg.edu.pl) received the M.Sc. degree in microwave engineering from Gdansk University of Technology, Poland in 2019, where he is currently a Ph.D. student. His main research interests include numerical electromagnetics, microwave filters and phasers. He was a recipient of a scholarship granted by Foundation for Polish Science.

Adam LAMECKI received the M.Sc., Ph.D. and D.Sc. degrees in electronics and electrical engineering from Gdansk University of Technology (GUT), Poland in 2002, 2007 and 2019, respectively. In 2006 he joined the Department of Microwave and Antenna Engineering, Faculty of Electronics, Telecommunications and Informatics at GUT, where he is an associate professor. His research interests include surrogate models and their application in the CAD of microwave components, computational electromagnetics, mainly focused on the finite element method, filter design and optimization techniques. He was a recipient of the Young Scientist Grant awarded by the Foundation for Polish Science, the Prime Minister of Poland Award for outstanding Ph.D. thesis, and the Scholarship for outstanding young researchers from the Polish Ministry of Science and Higher Education. He has been a principal investigator on several research projects funded by the Polish Ministry of Science and Higher Education, the Polish National Science Centre, and the Polish National Centre for Science and Development. He has co-authored over 35 papers in peer reviewed journals, including IEEE Transactions on Microwave Theory and Techniques, IEEE Microwave and Wireless Components Letters, and IEEE Antennas and Wireless Propagation Letters.

Michal MROZOWSKI received the M.Sc. and Ph.D. degrees, both with honors, from Gdansk University of Technology in 1983 and 1990, respectively. In 1986, he joined the Faculty of Electronics, Gdansk University of Technology, where he is now a full professor and the head of the Department of Microwave and Antenna Engineering. He is a member of Polish Academy of Sciences, Fellow of IEEE and Fellow of Electromagnetics Academy. He currently serves as an associate editor for the *Proceedings of IEEE*. He published more than 150 papers, mostly in IEEE journals. His current research interests include computational electromagnetics, the EDA of microwave devices, filter and sensor design, and optimization techniques.

Robust Digital Predistortion for LTE/5G Power Amplifiers Utilizing Negative Feedback Iteration

LIU Xin[1], CHEN Wenhua[1], WANG Dehan[1], NING Dongfang[2]

(1. Tsinghua University, Beijing 100084, China;
2. RHP System Department, ZTE Corporation, Xi'an 710114, China)

Abstract: A robust digital predistortion (DPD) technique utilizing negative feedback iteration is introduced for linearizing power amplifiers (PAs) in long term evolution (LTE)/5G systems. Different from the conventional direct learning and indirect learning structure, the proposed DPD suggests a two-step method to identify the predistortion. Firstly, a negative feedback based iteration is used to estimate the optimal DPD signal. Then the corresponding DPD parameters are extracted by forward modeling with the input signal and optimal DPD signal. The iteration can be applied to both single-band and dual-band PAs, which will achieve superior linear performance than the conventional direct learning DPD while having a relatively low computational complexity. The measurement is carried out on a broadband Doherty PA (DPA) with a 200 MHz bandwidth LTE signal at 2.1 GHz, and on a 5G DPA with two 10 MHz LTE signals at 3.4/3.6 GHz for validation in dual-band scenarios.

Keywords: 5G; digital predistortion; power amplifiers; negative feedback iteration

DOI: 10.12142/ZTECOM.202003008

http://kns.cnki.net/kcms/detail/34.1294.tn.20200831.1745.002.html, published online September 1, 2020

Manuscript received: 2019-12-12

Citation (IEEE Format): X. Liu, W. H. Chen, D. H.Wang, et al., "Robust digital predistortion for LTE/5G power amplifiers utilizing negative feedback iteration," *ZTE Communications*, vol. 18, no. 3, pp. 49-56, Sept. 2020. doi: 10.12142/ZTECOM. 202003008.

1 Introduction

In order to accommodate the growing demands of massive applications, modern wireless communication systems must evolve to provide higher data capacity and bit rate, and support multiple subscribers simultaneously. These requirements motivate the application of broadband modulated signals and concurrent multi-band transmission. In the forthcoming 5G era, the bandwidth requirements for transmission signals in sub-6 GHz frequency band and millimeter wave band are up to 200 MHz and 800 MHz, respectively.

As one of the key devices in radio frequency (RF) transmitters, the power amplifiers (PAs) are characterized as the most power-hungry components and their performance will directly affect the efficiency of RF transmitters. In modern communication system, high efficiency and linearity are two basic requirements for PAs. In order to acquire higher efficiency, the PA should be operated close to the saturation region, inevitably leading to strong nonlinear distortion. In the 5G communication system, the linearity requirements for the highly efficient PAs operated near the saturation region become even more stringent due to the application of broadband modulated bandwidth or concurrent multi-band transmission. Effective PA linearization techniques must be employed.

Digital predistortion (DPD) is the most popular PA linear-

This work was supported in part by National Key R&D Program of China under Grant No. 2018YFB1801603 and No. 2017YFF0206201, National Science and Technology Major Project under Grant 2017ZX03001024, NSFC under Grant No.61801259 and Beijing National Research Center for Information Science and Technology (BNRist).

ization technique in the current 4G system. Based on accurate behavioral modeling, DPD can predict PA's nonlinear behavior and eliminate them by adding a proper correction signal[1-6]. Due to the significant linearization performance and moderate hardware cost, the DPD technique is still one of the promising linearization solutions in 5G applications.

There are two common adaptive learning structures for DPD parameter extraction, that is, the direct learning (DL) architecture and the indirect learning (IDL) architecture[7-8]. **Fig. 1** depicts the block diagrams of DL and IDL structures. The IDL estimates the post-inverse model of PA and copies it as the predistorter, thus, the linear performance is limited since the noise at PA's output will be inevitably introduced in the parameter identification[9]. Moreover, the IDL provides compromised linearization performance when the PA is highly compressed, and generates DPD signals with high peak-to-average power ratio (PAPR) which might cause damage to the PAs. The DL algorithm, which is based on the pre-inverse model of PA, is more robust and provides more precise parameter identification than IDL[10]. However, since several iterations are needed before the DL algorithm converges to the optimal parameters, the DL estimation is more computationally expensive and complex in structure. In the broadband application scenario, the number of DPD parameters will be further increased in order to compensate the stronger nonlinear distortion, leading to the lower convergence speed and considerable calculation.

In Ref. [5], the concept of iterative learning control for the linearization of PAs is introduced, which provides a new perspective for DPD parameter extraction. Ref. [11] proposes a negative feedback iteration based digital predistortion to linearize the broadband PAs. In this paper, we present a more explicit investigation of the methodology and experimental results of the negative feedback iteration based DPD, and extend the technique to the multi-band scenario. The proposed DPD can realize superior linear performance in broadband application scenarios than conventional DL DPD while having a relatively low computational complexity. Furthermore, the proposed DPD can be prompted to the dual-band scenario. The measurements are performed on a broadband Doherty PA (DPA) with a 200 MHz bandwidth long term evolution (LTE) signal at 2.1 GHz, and on a DPA for 5G application with two 10 MHz LTE signals at 3.4/3.6 GHz carrier frequency to validate the performance of the proposed DPD technique.

2 Proposed DPD Technique Utilizing Negative Feedback Iteration

The block diagram of negative feedback iteration based DPD technique in single band scenario is presented in **Fig. 2**, where the proposed DPD method can be divided into two major steps. Firstly constructing a negative feedback iteration to obtain the optimal input signal of PA, which can be regarded as DPD signal, and then calculating the parameters of DPD module utilizing the original input signal and the optimal input signal obtained in the first step.

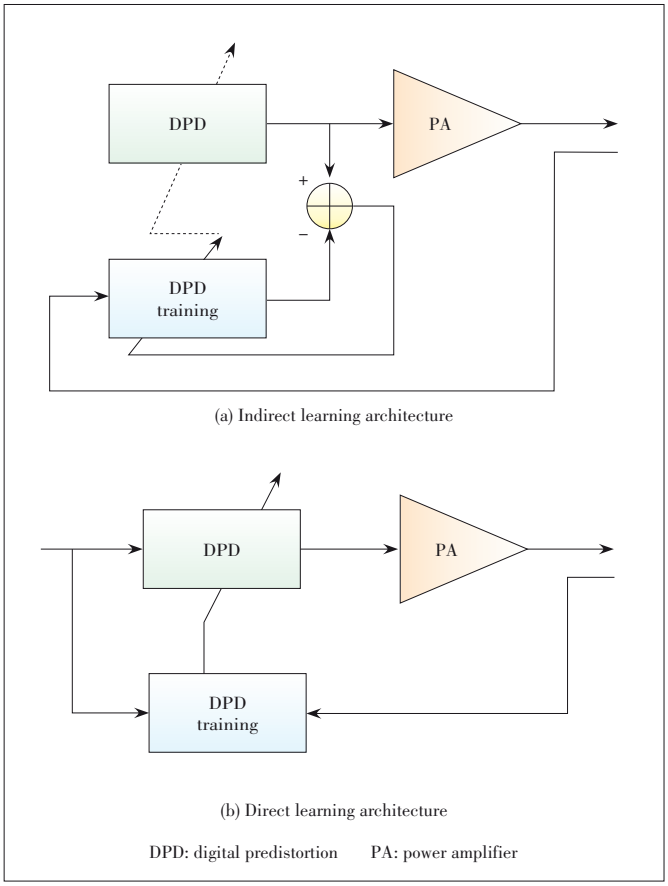

▲**Figure 1. Indirect learning (IDL) and direct learning (DL) architectures.**

2.1 Negative Feedback Iteration

According to the changes of output, the feedback can be divided into two categories: the positive feedback (which increases the output changes) and the negative feedback (which decreases the output changes). It is obvious that the output of PA will be more stable utilizing the negative feedback.

One of the simplest negative feedback structure is injecting the error between normalized output and input to the system as the new input. In the proposed method, the input signal in the previous iteration is considered, as presented in **Fig. 3**, which indicates that the input in the k-th iteration as:

$$x_k(n) = x_{k-1}(n) + w_0\left(u(n) - \lambda\tilde{y}_k(n)\right), \tag{1}$$

where $x_k(n)$ and $\tilde{y}_k(n)$ denote the normalized input and output of PA in the k-th iteration, and $u(n)$ is the original input signal. λ denotes the feedback depth, and w_0 is a control factor used to adjust the convergence of negative feedback iteration.

According to Eq. (1), the input signal of PA will be modified after each iteration. Since it is a negative feedback sys-

tem, the changes of output signal will decrease during the iteration and eventually tend to zero. However, due to the nonlinear behavior of PA, the output tends to be unchanged when the error between original input and output tends to be zero, that is, $u(n) - \lambda\tilde{y}_{k-1}(n) \approx 0$, which indicates that a linearized output will be obtained from the iteration format as in Eq. (1). At that time, the input signal of PA will also tend to be stable and have nonlinear relationship with the original input to produce the linear output.

2.2 DPD Parameter Extraction

The principle of DPD is to construct a nonlinear module cascaded before PA to linearize the output signal of PA. Therefore, the optimal input signal obtained in the negative feedback iteration can be regarded as the DPD signal. The input and output signal of DPD module can be expressed utilizing generalized memory polynomial (GMP) model[5], as shown in Eq. (2).

$$\begin{aligned} x_{DPD}(n) = & \sum_{k=1}^{K_a}\sum_{m=0}^{M_a} a_{km}u(n-m)\left|u(n-m)\right|^{k-1} + \\ & \sum_{k=1}^{K_b}\sum_{m=0}^{M_b}\sum_{l=1}^{L_b} b_{kml}u(n-m)\left|u(n-m-l)\right|^{k-1} + \\ & \sum_{k=1}^{K_c}\sum_{m=0}^{M_c}\sum_{l=1}^{L_c} c_{kml}u(n-m)\left|u(n-m+l)\right|^{k-1}, \end{aligned} \tag{2}$$

where $K_{a,b,c}$ and $M_{a,b,c}$ denote the nonlinear order and memory depth, and L_a and L_b are the lagging and leading depth, respectively.

In DL DPD, the iteration format of DPD parameters $\mathbf{b}$ with least square (LS) algorithm can be written as:

$$\mathbf{b}^{k+1} = \mathbf{b}^{k} + \mu\left(\mathbf{A}^{H}\mathbf{A}\right)^{-1}\mathbf{A}^{H}\left(\boldsymbol{u} - \boldsymbol{y}^{k}\right), \tag{3}$$

where $\mathbf{A}$ is the basis function matrix composed of original input; $\boldsymbol{u}$ and $\boldsymbol{y}$ denote original input and PA output signal column vector. Therefore, the DPD signal at k-th iteration has the form as:

$$\begin{aligned} \mathbf{x}_{DPD\_DL}^{k} &= \mathbf{A}\mathbf{b}^{k} \\ &= \mathbf{x}_{DPD\_DL}^{k-1} + \mu\mathbf{A}\left(\mathbf{A}^{H}\mathbf{A}\right)^{-1}\mathbf{A}^{H}\left(\mathbf{u} - \mathbf{y}^{k}\right). \end{aligned} \tag{4}$$

Let $\lambda = 1$, which indicates that the whole information of output signal is applied to the input, and the k-th DPD signal of proposed DPD can be written as:

$$\mathbf{x}_{DPD\_NF}^{k} = \mathbf{x}_{DPD\_NF}^{k-1} + w_0\left(\mathbf{u} - \mathbf{y}^{k}\right). \tag{5}$$

It appears that Eqs. (4) and (5) have the same iteration form under the case that the precise inverse matrix of $\mathbf{A}$ can be obtained. However, since the condition number of basis function matrix $\mathbf{A}$ increases dramatically with the increasing of parameters[12], the calculated inverse matrix is inaccurate which could enlarge the iteration error and the parameter accuracy would deteriorate in the next iteration. Therefore, the DPD signal obtained in the negative feedback iteration, which has eliminated the numerical error, can be regarded as the optimal DPD signal.

Once the optimal DPD signal is identified, the parameters

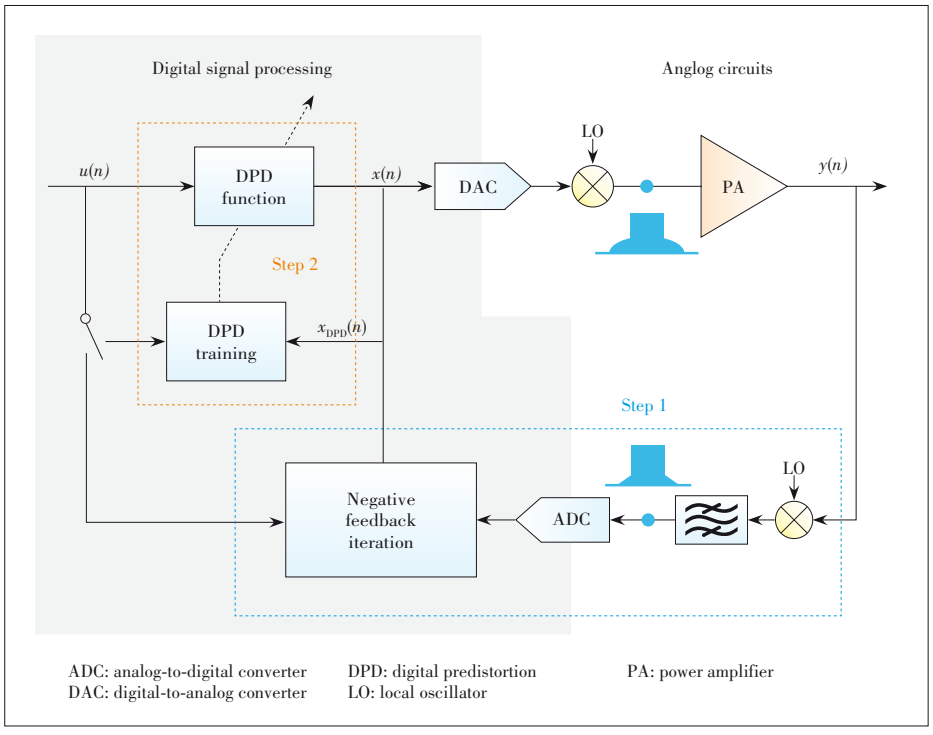

▲Figure 2. Structure of the negative feedback iteration based DPD technique in single-band scenario.

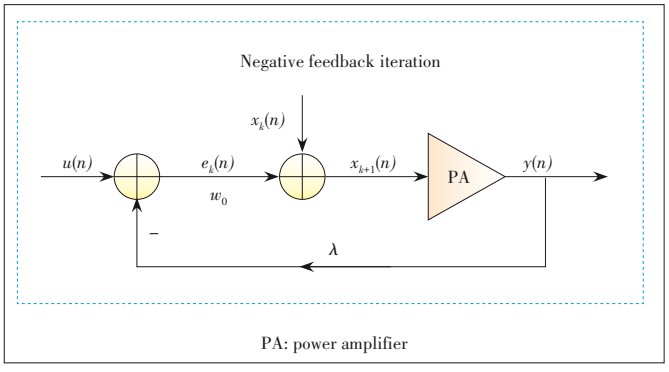

▲Figure 3. Proposed negative feedback loop for iteration.

of DPD module can be estimated using LS algorithm with the original input and DPD signal, as in Eq. (6).

$$\mathbf{b}_p = \left(\mathbf{A}^H\mathbf{A}\right)^{-1}\mathbf{A}^H\mathbf{x}_{DPD}, \tag{6}$$

where $\mathbf{b}_p$ denotes the coefficients of the predistorter, and $\mathbf{A}$ is composed of the basis functions in Eq. (2) with the original input signal $u(n)$.

Furthermore, another merit of the proposed DPD is the relatively low computational complexity. As it can be seen in Eq. (6), only once the parameter calculation is needed with the proposed DPD, while in the DL DPD the parameter calculation is needed in each iteration. Therefore, if the iteration times of both DPD schemes are equivalent, the computational complexity of the proposed DPD is less than the DL DPD.

2.3 Proposed DPD for Multi-Band PAs

In order to accommodate the growing demands of massive applications, the 5G and beyond 5G communication systems must evolve to support multiple standards at the same time. A diversity of wireless standards, along with the application of carrier aggregation (CA), present rigorous requirements for wireless transmitters. The increasing system complexity and fabrication cost are unaffordable and practically impossible. The concurrent multi-band transmitter is one of the most promising solutions to this problem. Since multiple signals in different frequency bands are combined and transmitted in the same nonlinear transmit path, the interaction of concurrent signals will produce complicated nonlinear distortions. In this case, numerous DPD techniques have been developed for multi-band transmitters[13 - 15].

The proposed digital predistortion can also be applied in multi-band scenarios. Take dual-band transmitter as an example. The input waveform is composed of dual-band signals, as in Eq. (7).

$$x(n) = x_1(n)e^{-j\omega mT_s} + x_2(n)e^{j\omega mT_s}, \tag{7}$$

where ω is the angular frequency, T_s is the sampling interval of base band signal, and $x_1(n)$ and $x_2(n)$ are the baseband envelop signals at the lower band and upper band respectively. The nonlinear behavior of dual-band PA can still be expressed as:

$$y(n) = \sum_{k=1}^{K}\sum_{m=0}^{M-1}\alpha_{km}x(n-m)\left|x(n-m)\right|^{k-1}. \tag{8}$$

By substituting Eq. (7) into Eq. (8), it is obviously that the output signals at lower band and upper band are related to the input information in each band, and the input signal from the other band also contributes to the distortion. This behavior can be described using 2D-DPD model [13], as in Eq. (9).

$$\begin{aligned} y_1(n) &= \sum_{m=0}^{M-1}\sum_{k=0}^{K}\sum_{l=0}^{k}\beta_{klm}^1 x_1(n-m)\left|x_1(n-m)\right|^{k-l}\left|x_2(n-m)\right|^{l} \\ y_2(n) &= \sum_{m=0}^{M-1}\sum_{k=0}^{K}\sum_{l=0}^{k}\beta_{klm}^2 x_2(n-m)\left|x_2(n-m)\right|^{k-l}\left|x_1(n-m)\right|^{l}, \end{aligned} \tag{9}$$

where $y_1(n)$ and $y_2(n)$ are the output signals at the lower band and upper band respectively. β_{klm}^1 and β_{klm}^2 denote the model coefficients.

The ideal output signals at lower and upper bands are linearized versions which only contain the input information in each band. Therefore, the negative feedback iteration format for dual-band PA has the similar form with that for single band scenario, as in Eq. (10).

$$\begin{aligned} \mathbf{x}_1^{DPD(k)} &= \mathbf{x}_1^{DPD(k-1)} + w_1\left(\mathbf{u}_1 - \lambda_1\mathbf{y}_1^{(k)}\right) \\ \mathbf{x}_2^{DPD(k)} &= \mathbf{x}_2^{DPD(k-1)} + w_2\left(\mathbf{u}_2 - \lambda_2\mathbf{y}_2^{(k)}\right). \end{aligned} \tag{10}$$

Generally, in order to save the fabrication cost, the shared feedback path is adopted to observe the output information in both frequency bands. In this case, the negative feedback iteration is performed on the lower band and upper band by turns. For instance, when identifying the optimal DPD signal for the upper band, the input signal in the upper band is modified in each iteration while the input signal in the lower band remains the same. **Fig. 4** shows the block diagram of the proposed DPD applied in dual-band transmitters.

After estimating the optimal DPD signal in both transmit bands, the predistorters can be identified by forward modeling using the 2D-DPD model in Eq. (9). In this case, the optimal DPD signals $x_1^{DPD}(n)$ and $x_2^{DPD}(n)$ in each band are regarded as the model output, and the original input signals $u_1(n)$ and $u_2(n)$ are the model input. Eq. (11) describes the coefficients extraction using LS algorithm.

$$\begin{aligned} \boldsymbol{\beta}_1 &= \left(\mathbf{A}_1^H\mathbf{A}_1\right)^{-1}\mathbf{A}_1^H\mathbf{x}_1^{DPD} \\ \boldsymbol{\beta}_2 &= \left(\mathbf{A}_2^H\mathbf{A}_2\right)^{-1}\mathbf{A}_2^H\mathbf{x}_2^{DPD}, \end{aligned} \tag{11}$$

where $\boldsymbol{\beta}_1$ and $\boldsymbol{\beta}_2$ are the coefficients of predistorters in upper and lower frequency band; $\mathbf{A}_1$ and $\mathbf{A}_2$ are the basis function matrixes composed of $u_1(n)$ and $u_2(n)$, as in Eq. (9).

3 Experimental Results

In this section, we present experimental results on two broadband DPAs to validate the proposed DPD technique in both single-band and dual-band scenarios. Both PAs are driven in high-efficiency points near the saturation region in order to validate the proposed method's performance and robustness under deep compression.

The experimental setups are depicted in **Fig. 5a**. Within the transmitting chain, a two-channel-synchronized vector sig-

nal generator (R&S SMW200A) was used to generate the broadband and dual-band RF signals from baseband samples. In the dual-band test, a wideband RF power combiner was responsible for combining the multiple signals before feeding them to the driver amplifier and the PA. In the single-band test, an LTE signal stream with a 200 MHz bandwidth (2-carrier) at 2.1 GHz and a 7.5 dB PAPR after crest factor reduction (CFR) were used as inputs in the experimental evaluations. The measurements were applied to a broadband (1.7 GHz – 2.8 GHz) Lab-made Cree CGH40010p DPA. In the dual-band scenario, the evaluations were performed on a Lab-made Cree CGH40010p DPA which was designed for 5G applications with a bandwidth of 3.3 – 3.8 GHz. The test signals were two 7.5 dB PAPR uncorrelated LTE signals of 10 MHz bandwidth at carrier frequencies of 3.4 GHz and 3.6 GHz. Both the DPAs were operated in the saturation region to acquire high efficiency and obvious nonlinearity for the validation of the proposed DPD. **Figs. 5b** and **5c** show the schematic of Lab-made DPAs.

On the feedback side, the broad and dual-band signals were coupled out from the PA output and thereafter converted to baseband samples by a spectrum analyzer (R&S FSW26). In the dual-band test, the upper band and lower band signals were captured by the wideband feedback path in each time slot, by turns. All algorithms and instrument control operations were performed on the host personal computer (PC) running Matlab. Adjacent channel power ratio (ACPR) was used to evaluate the nonlinear distortions performance.

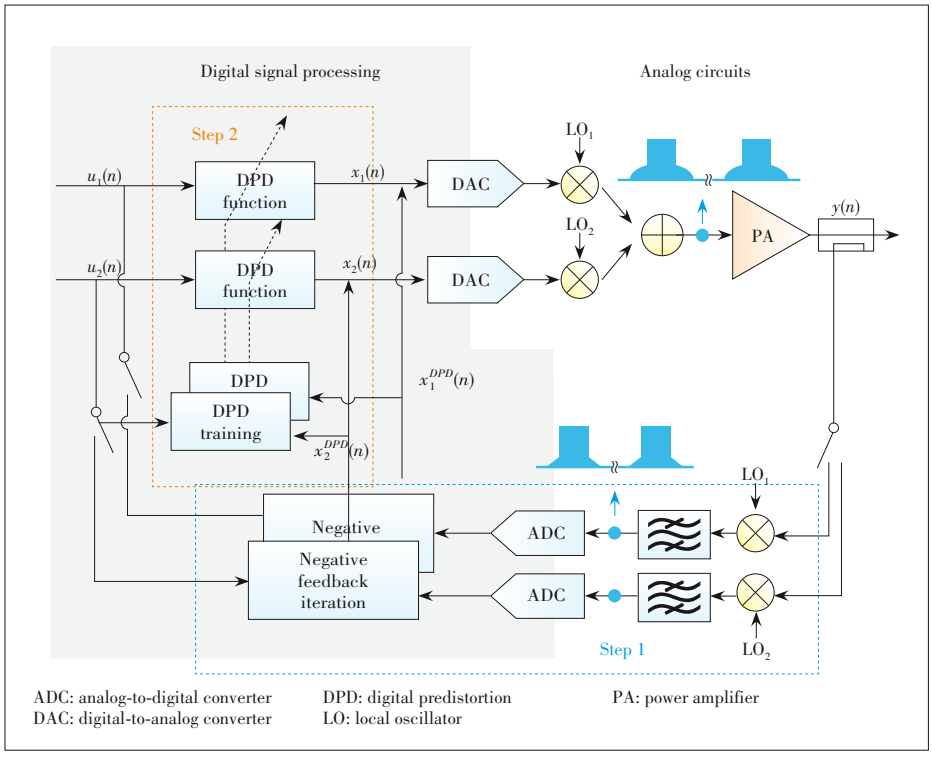

▲**Figure 4. Structure of the negative feedback iteration based DPD technique in dual-band scenario.**

3.1 Evaluations on Broadband PA

In the DPD test, the conventional DL DPD and IDL DPD were performed as well as the proposed DPD for comparison. The feedback depth λ and iteration step w were equal to 1 and 0.3 respectively. When the negative feedback iteration is converged, the output signal of PA is greatly linearized, presenting with the ACPRs of the first adjacent channel approaching −49 dBc.

The parameters of DPD module were estimated utilizing GMP model with $K_a = K_b = K_c = 11$, $M_a = M_b = M_c = 8$ and $L_a = L_b = 6$. **Fig. 6a** shows the AM/AM and AM/PM curve with/without the proposed DPD. The nonlinear distortion, especially the

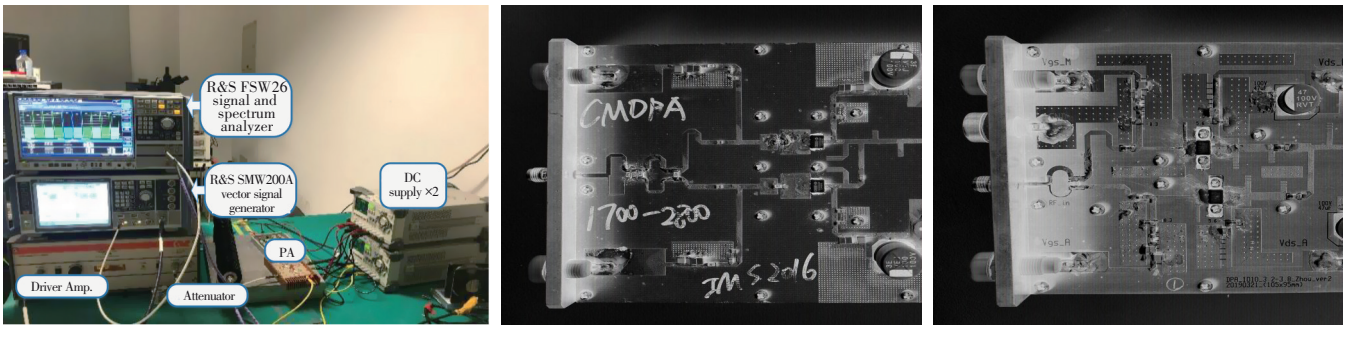

(a) System schematic (b) Lab-made 1. 7 – 2. 8 GHz DPA (c) Lab-made 3. 3 – 3. 8 GHz DPA

DC: digital converter DPA: doherty power amplifier PA: power amplifier

▲**Figure 5. Robust digital predistortion (DPD) test bench.**

memory effect, is obvious in the 200 MHz DPD test; however, the nonlinear characteristic has been improved significantly when applying the proposed DPD. **Fig. 6b** presents the power spectrum density (PSD) with/without DPDs at the output of PA. With the proposed DPD, the output signal can achieve –45 dBc ACPR, which outperforms the DL DPD and IDL DPD by 1 dB and 4 dB respectively. **Table 1** summarizes the linear performance of the PA's output signals.

Fig. 7a compares the converging speed between the negative feedback iteration and DL DPD by calculating the normalized mean square error (NMSE) between the PA input and output signals after each iteration. Both the negative feedback iteration and DL DPD converge after 5 – 6 iterations, while the negative feedback method shows a better NMSE performance.

Fig. 7b shows the iteration speed and accuracy with different iteration steps. The converging speed increases with the larger steps, however, the optimal linear performance is getting poorer with the increasing of iteration steps. Furthermore, the linearity of the output signal even becomes worse after the NMSE in the iteration reaches the optimum. The measured results indicate that the iteration step should be appropriately selected to balance the convergence speed and the linear performance.

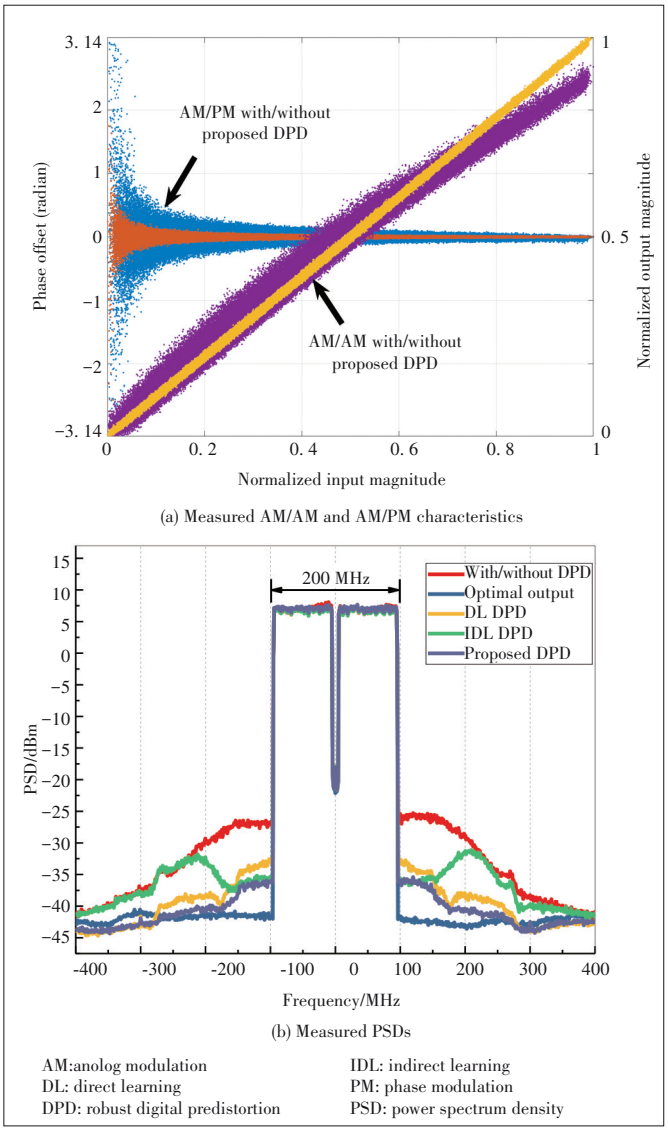

▲**Figure 6. Measured AM/AM and AM/PM characteristics and PSDs.**

▼**Table 1. Measured performance in single band scenario**

Scenario	Without DPD	Proposed DPD	DL DPD	IDL DPD
ACPR/dBc (±100 MHz)	–33.31/–34.42	–45.26/–45.25	–44.06/–44.37	–41.48/–42.41

ACPR: adjacent channel power ratio
DPD: digital predistortion
DL: direct learning
IDL: indirect learning

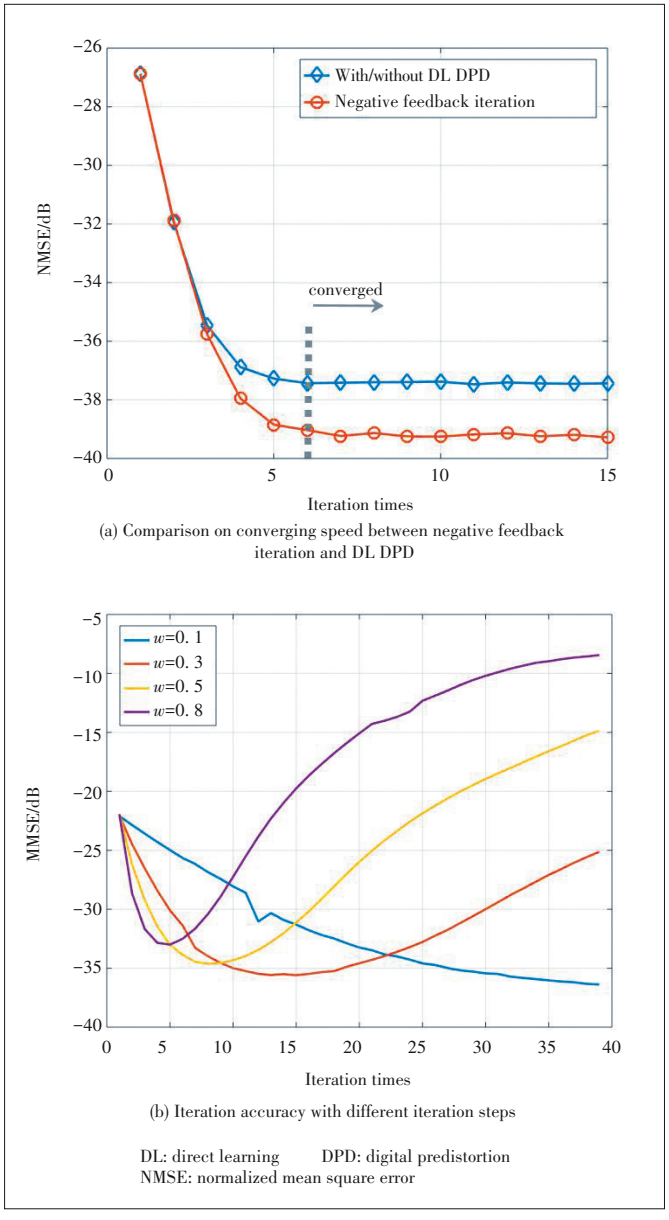

▲**Figure 7. Iterative convergence trend.**

3.2 Evaluations on Dual-Band PA

The proposed DPD is validated on a broadband (3.3 GHz – 3.8 GHz) DPA with the dual-band input signal. The dual-band signal is separated by 200 MHz at the carrier frequencies of 3.4 GHz and 3.6 GHz. Two uncorrelated 10 MHz LTE signals are applied in the dual-band measurements. The feedback depth λ_1, λ_2 and literation steps w_1, w_2 are the same for both frequency bands, which are equal to 1 and 0.3 respectively. Similar with the single band test, the negative feedback iterations converge quickly after 5 – 6 times modification. When the iteration converges, the optimal DPD signals which improve the ACPRs of PA output signals at both bands to about –55 dBc are obtained.

The parameters of predistorters in lower and upper frequency bands are extracted utilizing 2D-DPD model with K = 7, and M = 4. **Fig. 8** shows the AM/AM and AM/PM characteristics with/without the proposed DPD. The AM/AM and AM/PM curves in Fig. 8 show notable dispersion, which can be attributed to the intermodulation of the two uncorrelated signals at each frequency band. The nonlinear distortions and inter modulations are compensated significantly with the proposed DPD, showing a more than 20 dB ACPR improvement at both frequency bands. Fig. 8 depicts the observed PSDs of PA output signals at the lower band and upper band. **Table 2** summarizes the above linear performance.

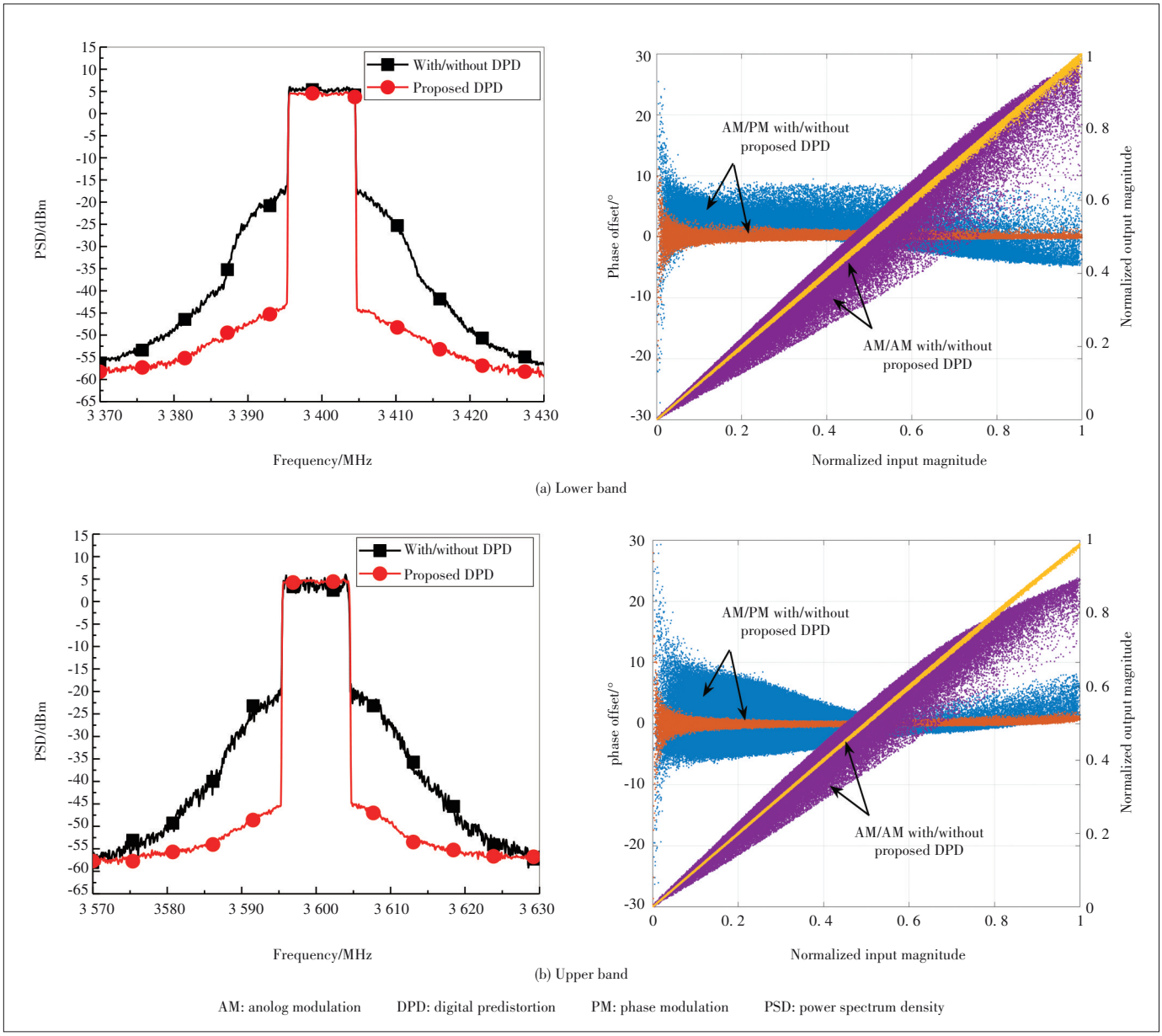

▲**Figure 8. Measured PSDs and AM/AM, AM/PM characteristics at power amplifier (PA)'s output with/without the proposed DPD.**

▼Table 2. Measured performance in dual-band scenario

Scenario	Lower Band		Upper Band	
	Without DPD	Proposed DPD	Without DPD	Proposed DPD
ACPR/dBc (±10 MHz)	−28.28/−28.81	−51.71/−51.45	−30.26/−29.43	−54.04/−53.33

ACPR: Adjacent channel power ratio DPD: digital predistortion

4 Conclusions

In this paper, a negative feedback iteration based DPD technique is proposed for linearizing power amplifiers in LTE/5G broadband and multi-band applications. The proposed DPD technique divides the conventional DPD process into two steps, which estimate the optimal DPD signal by negative feedback iteration and then identify the predistorter by forward modeling. Benefited from the iteration, the proposed DPD can achieve a better linearization performance than conventional DL DPD while having a lower computational complexity. The validations are carried on a broadband DPA with a 2-carrier 200 MHz bandwidth LTE signal at 2.1 GHz, and on a dual-band scenario with two 10 MHz LTE signals at 3.4 GHz and 3.6 GHz. The measurements provide potential application value of the proposed DPD in LTE/5G systems.

References

[1] DING L, ZHOU G T, MORGAN D R, et al. A robust digital baseband predistorter constructed using memory polynomials [J]. IEEE transactions on communications, 2004, 52(1): 159 – 165. DOI:10.1109/tcomm.2003.822188
[2] KIM J, KONSTANTINOU K. Digital predistortion of wideband signals based on power amplifier model with memory [J]. Electronics Letters, 2001, 37(23): 1417. DOI:10.1049/el:20010940
[3] ZHU A D, PEDRO J C, BRAZIL T J. Dynamic deviation reduction-based Volterra behavioral modeling of RF power amplifiers [J]. IEEE transactions on microwave theory and techniques, 2006, 54(12): 4323 – 4332. DOI: 10.1109/tmtt.2006.883243
[4] HAMMI O, GHANNOUCHI F M, VASSILAKIS B. A compact envelope-memory polynomial for RF transmitters modeling with application to baseband and RF-digital predistortion [J]. IEEE Microwave and wireless components letters, 2008, 18(5): 359 – 361. DOI:10.1109/lmwc.2008.922132
[5] MORGAN D R, MA Z, KIM J, et al. A generalized memory polynomial model for digital predistortion of RF power amplifiers [J]. IEEE transactions on signal processing, 2006, 54(10): 3852 – 3860. DOI:10.1109/tsp.2006.879264
[6] GHANNOUCHI F M, HAMMI O. Behavioral modeling and predistortion [J]. IEEE microwave magazine, 2009, 10(7): 52 – 64. DOI: 10.1109/mmm.2009.934516
[7] ZHOU D Y, DEBRUNNER V E. Novel Adaptive nonlinear predistorters based on the direct learning algorithm [J]. IEEE transactions on signal processing, 2007, 55(1): 120 – 133. DOI:10.1109/tsp.2006.882058
[8] PAASO H, MAMMELA A. Comparison of direct learning and indirect learning predistortion architectures [C]//IEEE International Symposium on Wireless Communication Systems. Reykjavik, Iceland: IEEE, 2008: 309 – 313. DOI: 10.1109/iswcs.2008.4726067
[9] AMIN S, ZENTENO E, LANDIN P N, et al. Noise impact on the identification of digital predistorter parameters in the indirect learning architecture [C]//Swedish Communication Technologies Workshop. Lund, Sweden: IEEE, 2012: 36 – 39. DOI:10.1109/swe-ctw.2012.6376285
[10] DING L, MUJICA F, YANG Z G. Digital predistortion using direct learning with reduced bandwidth feedback [C]//IEEE MTT-S International Microwave Symposium Digest. Seattle, USA: IEEE, 2013: 1 – 3. DOI: 10.1109/mwsym.2013.6697388
[11] LIU X, CHEN W H, CHEN L, et al. A robust and broadband digital predistortion utilizing negative feedback iteration [C]//IEEE MTT-S International Wireless Symposium (IWS). Chengdu, China: IEEE, 2018: 1 – 4. DOI:10.1109/ieee-iws.2018.8400950
[12] WU X F, SHI J H, CHEN H H. On the numerical stability of RF power amplifier's digital predistortion [C]//15th Asia-Pacific Conference on Communications. Shanghai, China: IEEE, 2009: 430 – 433. DOI:10.1109/apcc.2009.5375601
[13] BASSAM S A, HELAOUI M, GHANNOUCHI F M. 2-D digital predistortion architecture for concurrent dual-band transmitters [J]. IEEE transactions on microwave theory and techniques, 2011, 59(10): 2547 – 2553. DOI:10.1109/tmtt.2011.2163802
[14] LIU Y J, CHEN W H, ZHOU J, et al. Digital predistortion for concurrent dual-band transmitters using 2D modified memory polynomials [J]. IEEE transactions on microwave theory and techniques, 2013, 61(1): 281 – 290. DOI: 10.1109/tmtt.2012.2228216
[15] CHEN W H, BASSAM S A, LI X, et al. Design and linearization of concurrent dual-band doherty power amplifier with frequency-dependent power ranges [J]. IEEE transactions on microwave theory and techniques, 2011, 59(10): 2537 – 2546. DOI:10.1109/tmtt.2011.2164089

Biographies

LIU Xin received the B.S. degree in electronic information science and technology from Xidian University, China in 2017. She is currently pursuing the Ph. D. degree at Department of Electronic Engineering, Tsinghua University, China. Her current research interests include the behavioral modeling and digital predistortion for RF power amplifiers.

CHEN Wenhua (chenwh@tsinghua.edu.cn) received the B.S. degree in microwave engineering from the University of Electronic Science and Technology of China (UESTC) in 2001, and the Ph.D. degree in electronic engineering from Tsinghua University, China in 2006. From 2010 to 2011, he was a postdoctoral fellow with the Intelligent RF Radio Laboratory (iRadio Lab), University of Calgary, Canada. He is currently a professor with the Department of Electronic Engineering, Tsinghua University. His main research interests include power-efficiency enhancement for wireless transmitters, PA predistortion, and smart antennas. He has authored or coauthored over 120 journal and conference papers. Dr. CHEN is as an associate editor for the *IEEE Transaction on Microwave Theory and Techniques*, and the *International Journal of Microwave and Wireless Technology*. He was the recipient of the 2015 Outstanding Youth Science Foundation of NSFC, the 2014 URSI Young Scientist Award and the Student Paper Award of the 2010 Asia – Pacific Microwave Conference (APMC).

WANG Dehan received the B.S. degree in integrated circuit design and integration system from the University of Electronic Science and Technology of China (UESTC) in 2016. He is currently pursuing the Ph.D. degree at the Department of Electronic Engineering, Tsinghua University, China. His current research interests include the design of RF power amplifiers and RF integrated circuits.

NING Dongfang received the Ph.D. degree in control theory and control engineering from Northwestern Polytechnical University, China in 2009. He has been a wireless communication system expert of ZTE Corporation with over 10 years' experience in algorithm architecture and design. His research interest focuses on RF technology.

A Survey of Wi-Fi Sensing Techniques with Channel State Information

CHEN Liangqin[1], TIAN Liping[1], XU Zhimeng[1], CHEN Zhizhang[1,2]

(1. College of Physics and Information Engineering, Fuzhou University, Fuzhou 350108, China;
2. Department of Electrical and Computer Engineering, Dalhousie University, Halifax B3H 4R2, Canada)

DOI: 10.12142/ZTECOM.202003009

http://kns.cnki.net/kcms/detail/34.1294.TN.20200909.1100.002.html, published online September 10, 2020

Manuscript received: 2020-07-14

Abstract: A review of signal processing algorithms employing Wi-Fi signals for positioning and recognition of human activities is presented. The principles of how channel state information (CSI) is used and how the Wi-Fi sensing systems operate are reviewed. It provides a brief introduction to the algorithms that perform signal processing, feature extraction and recognitions, including location, activity recognition, physiological signal detection and personal identification. Challenges and future trends of Wi-Fi sensing are also discussed in the end.

Keywords: Wi-Fi sensing; channel state information; signal processing; classifications; feature extraction; positioning; location; recognitions

Citation (IEEE Format): L. Q. Chen, L. P. Tian, Z. M. Xu, et al., "A survey of Wi-Fi sensing techniques with channel state information," *ZTE Communications*, vol. 18, no. 3, pp. 57 – 63, Sept. 2020. doi: 10.12142/ZTECOM.202003009.

1 Introduction

With the fast progress and development of artificial intelligence, smart environment sensing and detection has attracted much attention recently, since it provides indispensable information and data for artificial intelligence. Sensing and detecting humans and their activities is an important branch and a vital component of many artificial intelligence applications[1].

Device-free wireless sensing using electromagnetic signals is an emerging technology with its advantages over other wired or non-electromagnetic sensing technologies, such as good penetration ability, relatively unrestricted availability and accessibility in space and time. With the increasing popularity and prevalent uses of Wi-Fi devices, Wi-Fi signals, occupying a part of the electromagnetic spectrum, are available in almost any place where humans live and work. As a result, it can be used for sensing and detecting humans and their activities, such as positioning, activity detection, gesture recognition and personal identification[2].

Recent developments have shown that the use of the channel state information (CSI) of Wi-Fi signals can be a viable method for human sensing and detection, in addition to the well-known received signal strength indication (RSSI) method. A time series of CSI contains the information of how wireless signals travel through and around objects and humans, and the information is embedded in time, frequency and space[3]. In other words, different human beings and their different activities can be sensed, detected, and recognized through analyzing the amplitude and phase of CSI. As a result, various signal processing and recognition algorithms have been developed to process CSI and relate it to human activities. This paper presents an overview of the algorithms and applications of human sensing with Wi-Fi signals that have been reported so far.

The outline of this paper is as follows. In section 2, the principle and the basic architecture of a Wi-Fi sensing system are introduced. In section 3, Wi-Fi sensing applications and the relevant technologies are presented. In section 4, the challenge and future trend of Wi-Fi sensing are discussed. In section 5, we conclude the paper.

2 Background

2.1 Channel State Information

A Wi-Fi channel with multiple-input multiple-output (MI-

This work was supported in part by National Natural Science Foundation of China (NSFC) under Grant No.61401100, Natural Science Foundation of Fujian Province under Grant No.2018J01805, Youth Research Project of Fujian Provincial Department of Education under Grant No. JAT190011, and Fuzhou University Scientific Research Fund Project under Grant No. GXRC-18074.

MO) usually employs the orthogonal frequency division multiplexing (OFDM) scheme that uses multiple subcarriers to form multiple links between transmitters and receivers. It can provide CSI for each transmission link with its carrier frequency. CSI characterizes how wireless signals propagate from the transmitter to the receiver along multiple paths. When a person appears in a channel and acts, such as walking, drinking, waving or even just breathing, CSI will change accordingly, which presents how wireless signals travel through and how they are affected by the body shape or the movement of a person. As a result, information about a person may be extracted and captured from the CSI.

To detect the CSI and its changes, the IEEE 802.11n CSI Tool[4] has been developed and widely used through Intel 5 300 Wi-Fi cards. One set of CSI can be obtained from each received data packet, and it represents the amplitude and the phase of each OFDM subcarrier, as shown in Eq. (1).

$$H(k) = \left\| H(k) \right\| e^{j\angle H(k)}, \tag{1}$$

where $\left\| H(k) \right\|$ and $\angle H(k)$ are, respectively, the amplitude and the phase of the k-th subcarrier. Both amplitude $\left\| H(k) \right\|$ and phase $\angle H(k)$ are affected by the body shape or the movement of a person. The CSI can be measured and therefore processed for information extraction, forming the basic principle of the Wi-Fi sensing and detection.

2.2 Wi-Fi CSI Processing System

A general processing flowchart of a Wi-Fi CSI sensing system is depicted in **Fig. 1**. CSI measurements are first collected by the receivers and then sent to a processor or a computer for extracting the CSI amplitude, phase and Doppler frequency shift (DFS) that are related to the environments. First, signal segmentation and noise elimination are applied to obtain clean and usable signals, which are conducted with Hampel filter, wavelet transformation, moving averaging and median filters. Differential techniques and linear regression are also used to remove raw CSI phase offsets. Next, the signals are processed to obtain key features and classifications in either one of the following two manners: (1) statistical and spectrum feature extractions first and then classifications with machine learning algorithms such as support vector machines (SVM)[5], k-nearest neighbors (KNN)[6] or Bayes[7]; (2) simultaneous feature extractions and classifications directly with all-inclusive machine learning algorithms such as the convolutional neural network (CNN)[8], recurrent neural network (RNN)[9], and long short-term memory (LSTM)[10]. They are based on deep learning and have been developed in recent years.

3 Algorithms and Applications

3.1 Wi-Fi Positioning (or Locating)

Wi-Fi sensing technology was first used for positioning applications in 2000[11]. It can be categorized into two types: the fingerprint-based method and the model-based method. With the fingerprint-based method, target locations are determined with radio signal fingerprints constructed by RSSI or CSI. The position of an object is estimated with the fingerprint database which is acquired beforehand. Developing and updating the fingerprint database is, however, time-consuming and labor-intensive. In the model based methods, Wi-Fi signal propagation models are developed and used to estimate distances between the target and the known access points, and triangula-

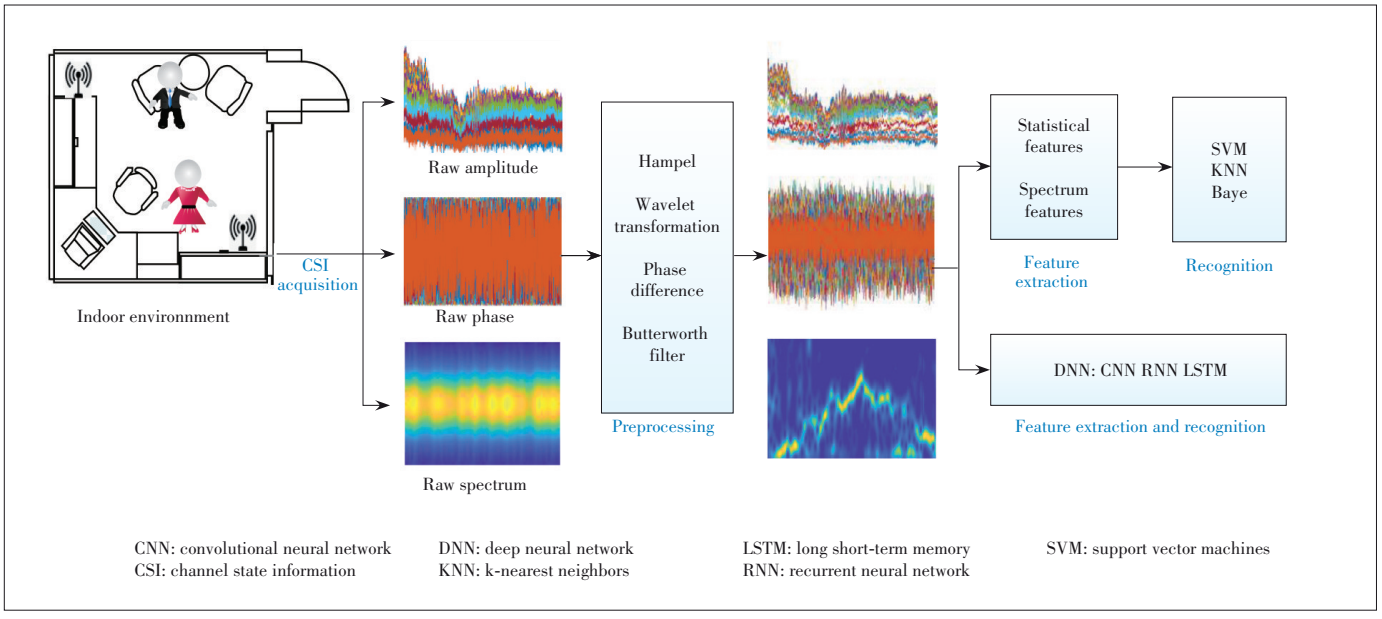

▲**Figure 1. Processing flow chart of a Wi-Fi sensing system.**

tion is applied for positioning. The accuracy of the propagation model parameters directly affects positioning accuracy.

The propagation models include angle of arrival (AoA), time of flight (ToF) and DFS. However, the accuracy still needs to be improved, especially in complex indoor multi-path environment, in spite that some work has been claimed to achieve decimeter-level or even centimetre-level positioning accuracy. To increase the accuracy and resolution of AoA estimation, SpotFi[12] utilizes OFDM subcarriers as sensors and applies the standard multiple signal classification (MUSIC) algorithm[13] to the constructed measurement matrix to estimate both the AoA and ToF parameters of multiple signal paths. The joint AoA and ToF estimations are made from the same signal path but in different data packets. Gaussian mean clustering algorithm is used to process clustered signals and associated parameters first, and then the highest likelihood metric is used to identify the direct path. The target location is determined based on the best match of the estimated AoA value of the direct path and its RSSI. SpotFi achieves a median location accuracy of 40 cm in a multipath-rich indoor environment. In general, AoA just provides the arrival direction of the signal, not the distance of a target. Therefore, AOAs measured from multiple access points are used, and interactions of their projection lines give the locations of a target. Three to four access points are used in SpotFi for a home environment.

In Ref. [14], a system that uses a single Wi-Fi access point, is proposed to locate targets to within tens of centimetres. By eliminating packet detection delay, resolving phase offsets, and mitigating multi-path, it can compute the absolute ToF using commodity Wi-Fi cards at sub-nanosecond accuracy. In Ref. [15], by quantifying the relationships between CSI and a target's location and velocity, a theoretical model is developed and has achieved the decimeter-level passive tracking. It extracts the path length change rate (PLCR) from noisy CSI measurements and derives moving velocity from PLCR through at least two links, as shown in **Fig. 2**. At least two links are required to determine the moving direction of a target, and the distance between the receivers needs to be separated by a certain distance. In Ref. [16], joint estimations of AoA, ToF and DFS are exploited to achieve passive human location and tracking using a single link of Wi-Fi devices. Recent research efforts focused more on the use of multi-model sensing data such as computer vision to achieve positioning and tracking of multiple people at high accuracy[17].

3.2 Wi-Fi Recognitions of Human Activities

As mentioned before, the information on how wireless signals propagate from a transmitter to a receiver at carrier frequencies along multiple paths is contained in CSI. The CSI amplitude and phase vary differently with different human activities, and they can be used for human behavior recognition. Many activity recognition algorithms have been developed, and they usually include three parts: signal preprocessing, fea-

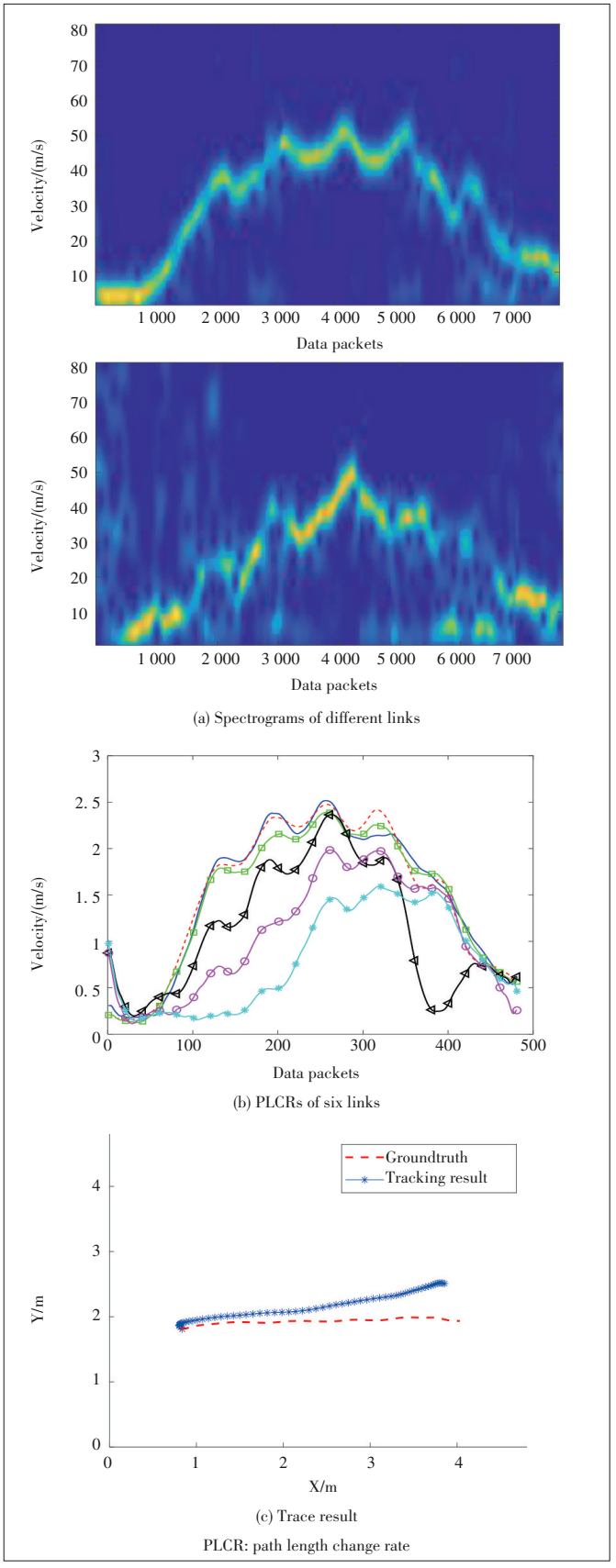

▲**Figure 2. Illustration of the Widar tracking results presented in Ref. [15].**

ture extraction and classification, as shown in Fig. 1.

Figs. 3a and **3b** show the typical signals before and after the signal preprocessing with Butterworth filter and wavelet transformation. As can be seen in Fig. 3b, noises are mitigated or even removed. After the noise mitigation, statistical features such as average, variance and energy are extracted for classification in activity recognition, as shown in **Figs. 3c** and **3d**[18]. Deep learning methods based on neural networks are also used in activity recognition in recent years[19-20]. In the field of image recognition, many deep learning models have already been developed. These models can be modified and used in Wi-Fi activity recognition by transforming 1D CSI signals to 2D images.

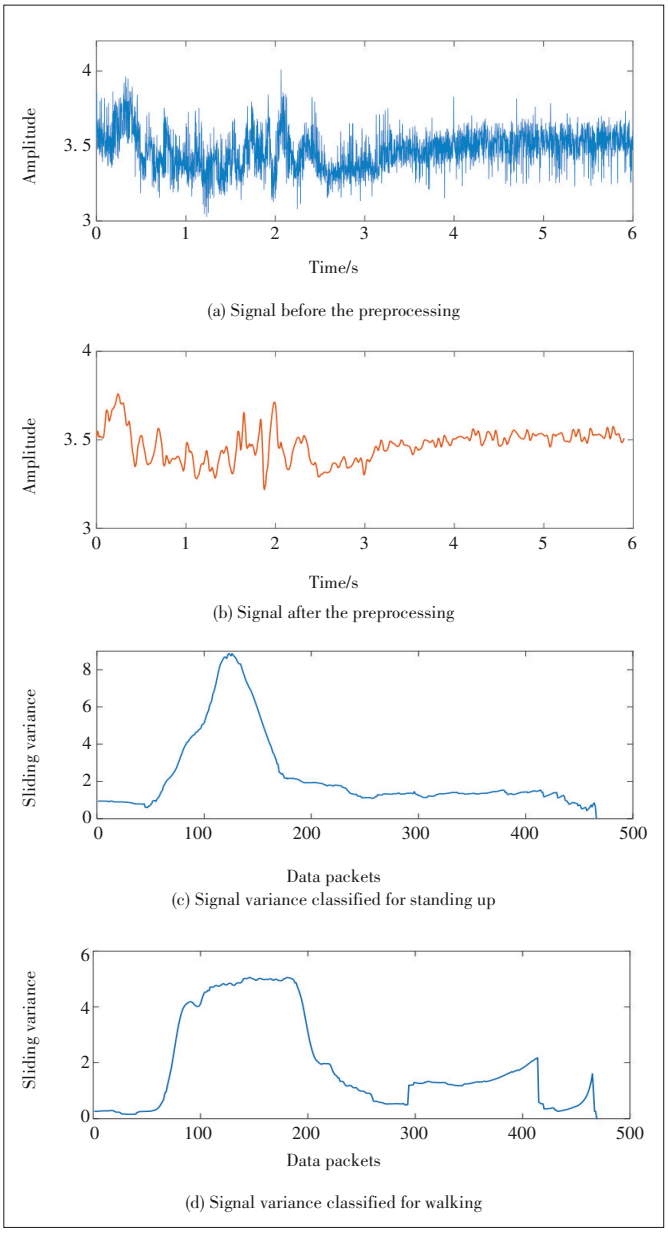

▲**Figure 3. Typical signal variations and features of activity recognitions.**

The main challenge in the activity recognition is that the accuracy of multiple-people recognition is not high enough. Recently, we have proposed a new algorithm to overcome the multiple-people recognition problem. A multi-dimensional feature configuration to make full use of CSI information, including spatial correlation and temporal correlation is developed. The experimental results verify the robustness of our algorithm in multiple scenarios.

3.3 Wi-Fi Extraction of Physiological Signals

When a person is stationary (such as standing, sitting and sleeping), a Wi-Fi sensing system can sense his respiration and heart rate through measurements of the CSI. In Ref. [21], the Fresnel model is introduced to investigate the impact of respiration on the wireless signals and the theoretical model is developed to relate respiration depth, heart rate and positions to signal patterns (or classifications). Using the Fresnel model, location-dependent processing algorithms can be applied, which in turn helps improve the sensing accuracy.

The existing respiration estimation techniques are mainly applicable to the condition that a person is not moving. When a person moves, information extractions from weak heart rate and breathing are challenging since signal variations due to the movements can overwhelm the signals desired. We have researched breathing estimation of a person in the standing or sitting positions with body swing. Since different subcarriers have different sensitivities to the movements in different directions, we select the subcarrier most sensitive to breathing. To do so, the recurrence plot (RP) method is used to analyze the periodicity of CSI measurements of each subcarrier, as shown in **Fig. 4**. A peak detection algorithm is developed in the frequency-time domain to extract the respiration rate. Our algorithm can eliminate the disturbance of walking to the CSI measurements and extract human respiration rate and heart rate during walking, as shown in **Fig. 5**.

3.4 Wi-Fi Personal Identification

Personal identification is one of the most convenient and important applications with Wi-Fi signals. Since gestures and gaits of a person are unique, they can be used to identify people. Many algorithms have been developed so far.

WiWho is developed to identify a person from a small group of people over a short walking distance of 2 – 3 meters on a straight-line path[22]. It extracts steps and walking gaits of a person from CSI. Step and walking segment features are combined to develop a complete gait pattern profile and a decision-tree-based machine learning classifier is then developed and used to complete the personal identification. However, WiWho can only be used in the single-person situation in corridors or hallways. In addition, it has been tested only for the age group of 25 – 30 years old, while gaits of different ages are different.

The WiFi-ID system proposed in Ref. [23] analyses CSI, ex-

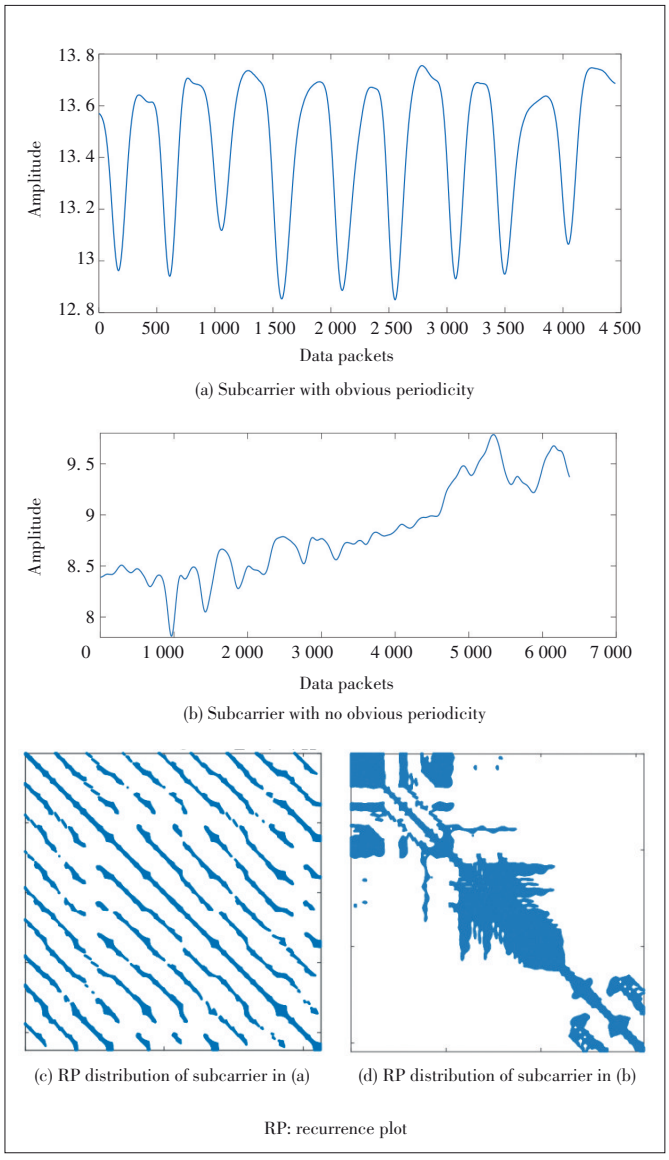

▲Figure 4. Recurrence plot of different subcarriers.

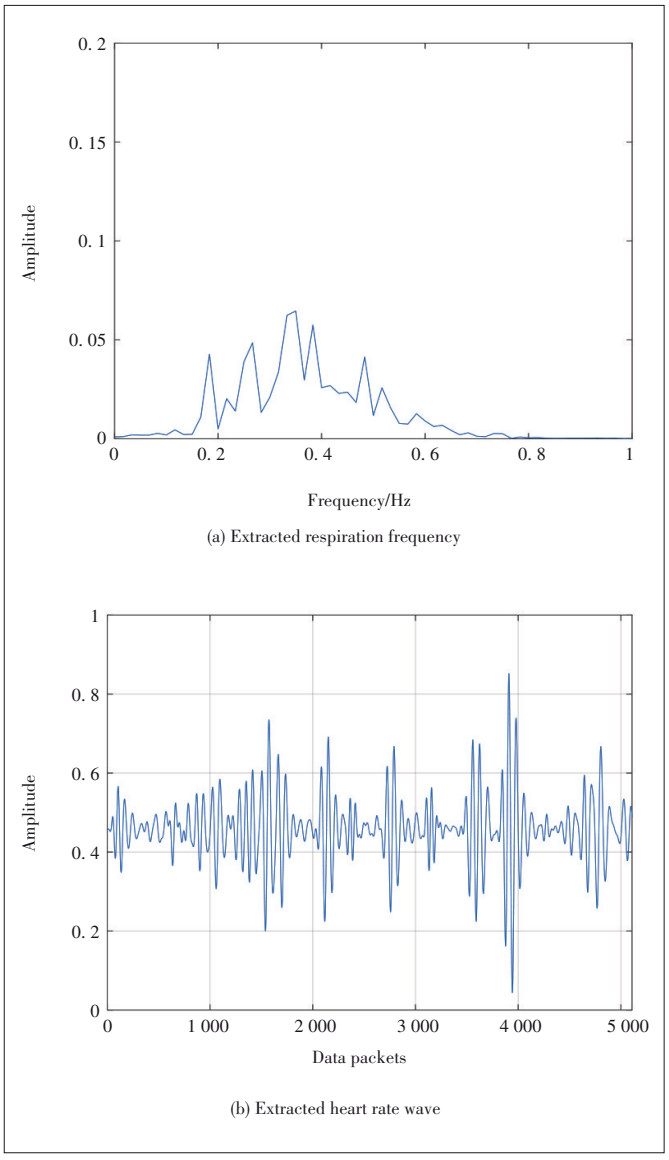

▲Figure 5. Respiration and heartbeat rate sensing of human in walking.

tracts unique features of walking gaits and achieves the identification of average accuracy of 93% to 77% for a group of 2 to 6 persons. In Ref. [24], the authors present a WFID system, propose a novel feature of subcarrier-amplitude frequency (SAF), and extract it from the subcarriers using the SVM algorithm, which achieves identification with the accuracies of 93.1% and 91.9% for the group of 6 and 9 people in two indoor scenarios, respectively.

Although WiFi-ID and WFID can recognize multiple persons, they are applicable to the situations where the walking trajectory passes through the line of sight (LOS) path between the transceivers or is in a straight line. Such a restriction makes the two algorithms not suitable for general home or office environments

In Ref. [25], a system called WifiU is developed to detect the gaits of a person. It exploits signal processing technology to make spectrograms from CSI measurements and extract gait patterns that include walking speed, gait cycle time and footstep lengths. An SVM classifier is developed and used to achieve identification. The limitation of WifiU is that the person must walk on a predefined path in a predefined walking direction. Training for a new classification model is needed for a different walking path and directions.

In addition to the above problems or limitations, many other factors may also affect recognition accuracies, such as clothes and shoes. Furthermore, temporary gait pattern changes of a person due to the carrying of a heavy backpack or a heavy object, or injury, may result in recognition failure. Therefore, it is necessary to develop robust means to achieve effective and accurate identification, including com-

binations of gait and physiological recognition. We are developing a system, named Wi-GAH, which uses gestures to achieve personal identification. Wi-GAH can not only identify persons based on gestures but also recognize the meanings of the gestures at the same time so that more sensing data are available for automatic system adaption to the varying home environments.

4 Challenges and Future Trends of Wi-Fi Sensing

Most of the Wi-Fi based sensing systems presented so far assume a single person scenario. Sensing in multi-people scenarios faces many challenges, such as how to determine the number of people in a group and how to distinguish among different people. New models and new algorithms need to be developed to mitigate the shadowing effects, especially when multiple people are close to each other[26]. The multi-path propagation models that can quantitatively correlate CSI dynamics and multi-person activities are also needed[27].

Furthermore, it is very challenging to deal with changes of the environments and to develop a universal Wi-Fi sensing system that can automatically adapt to the new environments. The CSI amplitude, CSI phase and DFS are very much affected by the environments[28]. When an environment changes, for example the distance and direction between the target and Wi-Fi transceiver alter, the accuracy of Wi-Fi sensing is affected. With the existing algorithms, new data are needed for training to ensure accuracy every time when an environment is changed. Along this line, body-coordinate velocity profile (BVP) is proposed for gesture recognition[29], which appears to be a potentially feasible solution. The emerging deep-learning-based methods, such as cross-domain methods and transfer learning techniques, show some potentials too. Deep similarity evaluation networks and deep generative adversarial networks (GAN) reduce training efforts significantly[30]. Cross-device and cross-sensor methods are also considered helpful. Finally, Wi-Fi based sensing can be integrated with 5G based mobile communication networks to provide more comprehensive data and services for the sensing processing in the industries such as smart museums, smart hospitals, smart shopping malls, and smart factories.

5 Conclusions

In this paper, we discuss Wi-Fi sensing technologies in indoor multi-path environments and present the principle and basic methods of Wi-Fi sensing. The Wi-Fi sensing applications and the relevant algorithms in location, activity recognition, physiological signal extraction and personal identification are briefly described. A few classic sensing algorithms are discussed and analyzed in detail. In the end, we present the challenges in multi-people sensing and cross-scenario sensing. Future trends of the research and development in the area are briefly discussed.

References

[1] LU Y, LV S H, WANG X D, et al. A survey on Wi-Fi based human behavior analysis technology [J]. Chinese journal of computers, 2019, 42(2): 1 – 21. DOI: 10.11897/SP.J.1016.2019.00231
[2] WANG J, ZHAO Y N, FAN X X, et al. Device-free identification using intrinsic CSI Features [J]. IEEE transactions on vehicular technology, 2018, 67(9): 8571 – 8581. DOI:10.1109/tvt.2018.2853185
[3] MA Y S, ZHOU G, WANG S Q. WiFi sensing with channel state information [J]. ACM computing surveys, 2019, 52(3): 1 – 36. DOI:10.1145/3310194
[4] HALPERIN D, HU W J, SHETH A, et al. Tool release [J]. ACM SIGCOMM computer communication review, 2011, 41(1): 53. DOI: 10.1145/1925861.1925870
[5] HE W F, WU K S, ZOU Y P, et al. WiG: WiFi-based gesture recognition system [C]//2015 24th International Conference on Computer Communication and Networks (ICCCN). Las Vegas, USA, 2015: 1 – 7. DOI:10.1109/icccn.2015.7288485
[6] LI H, YANG W, WANG J X, et al. WiFinger: talk to your smart devices with finger-grained gesture [C]//The 2016 ACM International Joint Conference on Pervasive and Ubiquitous Computing. New York, USA, 2016: 250 – 261. DOI: 10.1145/2971648.2971738
[7] WANG Y, YANG J, CHEN Y Y, et al. Tracking human queues using single-point signal monitoring [C]//Annual International Conference on Mobile Systems, Applications, and Services. New Hampshire, USA, 2014:42 – 54. DOI: 10.1145/2594368.2594382
[8] MA Y S, ZHOU G, WANG S Q, et al. SignFi: sign language recognition using Wi-Fi [J]. ACM on interactive, mobile, wearable and ubiquitous technologies, 2018, 2 (1): 1 – 21. DOI:10.1145/3191755
[9] OHARA K, MAEKAWA T, MATSUSHITA Y. Detecting state changes of indoor everyday objects using Wi-Fi channel state information [J]. Proceedings of the ACM on interactive, mobile, wearable and ubiquitous technologies, 2017, 1(3): 1 – 28. DOI:10.1145/3131898
[10] SINGH U, DETERME J F, HORLIN F, et al. Crowd forecasting based on wifi sensors and lstm neural networks [J]. IEEE transactions on instrumentation and measurement, 2020: 1. DOI:10.1109/tim.2020.2969588
[11] BAHL P, PADMANABHAN V N. Radar: an in-building RF-based user location and tracking system [C]//19th Annual Joint Conference of the IEEE Computer and Communications Societies. Tel Aviv, Israel, 2000:775 – 784. DOI: 10.1109/infcom.2000.832252
[12] KOTARU M, JOSHI K, BHARADIA D, et al. SpotFi: decimeter level localization using Wi-Fi [J]. ACM SIGCOMM Computer communication review, 2015, 45(4): 269 – 282. DOI:10.1145/2829988.2787487
[13] SCHMIDT R. Multiple emitter location and signal parameter estimation [J]. IEEE transactions on antennas and propagation, 1986, 34(3): 276 – 280. DOI: 10.1109/tap.1986.1143830
[14] VASISHT D, KUMAR S, KATABI D. Decimeter-level localization with a single Wi-Fi access point [C]//The 13th USENIX Symposium on Networked Systems Design and Implementation. Santa Clara, USA, 2016: 165 – 178
[15] QIAN K, WU C S, YANG Z, et al. Widar: decimeter-level passive tracking via velocity monitoring with commodity Wi-Fi [C]//ACM Mobihoc 2017. Chennai, India, 2017: 1 – 10. DOI: http://dx.doi.org/10.1145/3084041.3084067
[16] QIAN K, WU C S, ZHANG Y, et al. Widar 2.0: passive human tracking with a single Wi-Fi link [C]//The 16th Annual International Conference on Mobile Systems. Applications, and Services. New York, USA, 2018: 1 – 12. DOI: 10.1145/3210240.3210314
[17] LU G Y, SONG J K. 3D image-based indoor localization joint with WiFi positioning [C]// ACM on International Conference on Multimedia Retrieval. New York, USA, 2018: 1 – 8. DOI:10.1145/3206025.3206070
[18] GUO A Y, XU Z M, CHEN L Q. A human action recognition method based on

Wi-Fi channel state information [J]. Chinese journal of sensors and actuators, 2019, 32(11): 1688 – 1693. DOI: 10.3969 /j.issn.1004-1699.2019.11.015
[19] BU Q R, YANG G, MING X X, et al. Deep transfer learning for gesture recognition with WiFi signals [J]. Personal and ubiquitous computing, 2020. DOI: 10.1007/s00779-019-01360-8
[20] ARSHAD S, FENG C H, YU R Y, et al. Leveraging transfer learning in multiple human activity recognition using WiFi signal [C]//2019 IEEE 20th International Symposium on "A World of Wireless, Mobile and Multimedia Networks". Washington, USA, 2019: 1 – 10. DOI:10.1109/wowmom.2019.8793019
[21] WANG H, ZHANG D Q, MA J Y, et al. Human respiration detection with commodity Wi-Fi devices [C]//ACM International Joint Conference on Pervasive and Ubiquitous Computing. New York, USA, 2016: 25 – 36. DOI: 10.1145/2971648.2971744
[22] ZENG Y Z, PATHAK P H, MOHAPATRA P. WiWho: WiFi-based person identification in smart spaces [C]//15th ACM/IEEE International Conference on Information Processing in Sensor Networks. Vienna, Austria, 2016: 1 – 12. DOI: 10.1109/ipsn.2016.7460727
[23] ZHANG J, WEI B, HU W, et al. WiFi-ID: human identification using WiFi signal [C]//2016 International Conference on Distributed Computing in Sensor Systems. Washington, USA, 2016: 1 – 8. DOI:10.1109/dcoss.2016.30
[24] HONG F, WANG X, YANG Y N, et al. WFID: passive device-free human identification using Wi-Fi signal [C]//Mobiquitous'16. Hiroshima, Japan, 2016: 1-10. DOI: http://dx.doi.org/10.1145/2994374.2994377
[25] WANG W, LIU A X, SHAHZAD M. Gait recognition using Wi-Fi signals [C]//UbiComp '16. Heidelberg, Germany, 2016: 363 – 373. DOI: http://dx.doi.org/10.1145/2971648.2971670
[26] WANG J, GAO Q H, PAN M, et al. Device-free wireless sensing: challenges, opportunities, and applications [J]. IEEE network, 2018, 32(2): 132 – 137. DOI: 10.1109/MNET.2017.1700133
[27] WANG W, LIU A X, SHAHZAD M, et al. Understanding and modeling of Wi-Fi signal based human activity recognition [C]//MobiCom'15. Paris, France, 2015: 65 – 76. DOI: http://dx.doi.org/10.1145/2789168.2790093
[28] YANG Z, ZHENG Y, WU C S. Intelligent wireless sensing in the AIoT: features, algorithms, and data sets [J]. Communications of the CCF, 2020, 16(2): 50 – 56
[29] ZHENG Y, ZHANG Y, QIAN K, et al. Zero-effort cross-domain gesture recognition with Wi-Fi [C]//17th Annual International Conference on Mobile Systems, Applications, and Services. New York, USA: 2019. DOI: 10.1145/3307334.3326081
[30] WANG J, GAO Q H, MA X R, et al. Learning to sense: deep learning for wireless sensing with less training efforts [J]. IEEE wireless communications, 2020, 27(3): 156 – 162. DOI:10.1109/mwc.001.1900409

Biographies

CHEN Liangqin received the Ph.D. degree in communication and information systems from Fuzhou University, China in 2018. Since 2005, she has undertaken teaching and research work at Fuzhou University. Her research interests include wireless signal transmission, wireless sensing and detection.

TIAN Liping received the Master's degree in communication and information systems from Fuzhou University, China in 2013. She is currently pursuing the Ph.D. degree at Fuzhou University. Her research interests include wireless signal transmission and sensing.

XU Zhimeng received the B.Sc. degree in radio physics from Lanzhou University, China in 2002, the M.Sc. and Ph.D. degrees in information and communication engineering from Xidian University and Fuzhou University in 2005 and 2013, respectively. He was with the Department of Electrical and Computer Engineering at Dalhousie University, Canada as a postdoctoral fellow from 2016 to 2017 and was a visiting scholar with the Department of Technology at the University of Northern Iowa, USA from 2011 to 2012. His research interests include ultra-wideband technologies, wireless sensing technologies, and wireless information & power transfer technologies.

CHEN Zhizhang (chen@dal.ca) received the B. Eng. degree in radio engineering from Fuzhou University, China, the Master's degree in radio engineering from Southeast University, China, and the Ph.D. degree in electrical engineering from the University of Ottawa, Canada. He is a professor and the former Head of the Department of Electrical and Computer Engineering, Dalhousie University, Canada. He has authored and co-authored over 450 journal and conference papers in computational electromagnetics, RF/microwave electronics, antennas and wireless technologies. He is the Fellow of the IEEE, the Canadian Academy of Engineering and the Engineering Institute of Canada.

Non-Negligible Influences of Rain on 5G Millimeter Wave Terrestrial Communication System

Abstract: The impacts of rain on millimeter wave (mmW) terrestrial links, which are inevitably affected by ground-objects-induced multipath propagation, are presented based on the signal time series data measured at 35 GHz. We analyze the coupled influence mechanism of rain-induced and ground-objects-induced multipath propagation on mmW terrestrial links. It can be deduced that the rain-induced impacts on millimeter wave terrestrial links cannot be neglected. The results given in this paper are significant for developing 5G millimeter wave terrestrial mobile communication links.

Keywords: 5G communication; mmW; multipath; rain-caused effects; terrestrial links

GONG Shuhong[1], ZHANG Xingmin[1], DOU Jianwu[2], HUANG Weifang[2]

(1. School of Physics and Optoelectronic Engineering, Xidian University, Xi'an 710071, China;
2. Algorithm Department, ZTE Corporation, Shanghai 200240, China)

DOI: 10.12142/ZTECOM.202003010

http://kns.cnki.net/kcms/detail/34.1294.TN.20200317.1006.003.html, published online March 17, 2020

Manuscript received: 2019-01-15

Citation (IEEE Format): S. H. Gong, X. M. Zhang, J. W. Dou, et al., "Non-negligible influences of rain on 5G millimeter wave terrestrial communication system," *ZTE Communications*, vol. 18, no. 3, pp. 64 – 70, Sept. 2020. DOI: 10.12142/ZTECOM.202003010.

1 Introduction

Millimeter wave (mmW) technology is regarded as a key technology for 5G mobile communication system, because it is greatly helpful for solving the bottleneck problems, which are the main contradictions between the required traffic in the future and the current 2G, 3G and 4G communication systems[1 – 5]. Meanwhile, it is also necessary to face more complex propagation characteristics for fully taking advantage of millimeter wave technology[6 – 8].

One of the principal technical difficulties for mmW technology is to evaluate the impacts of the troposphere, such as rain-induced attenuation, depolarization and noise. The propagation characteristics of millimeter wave in the troposphere have been regarded as an important part of radio wave propagation field[9]. Many calculating models and measured data about the propagation properties are given, and ITU-R models may be the most authoritative and reliable[10 – 11]. In general, rain-induced impacts are the most severe impacts and the first aspect to consider. Therefore, rain-induced impacts are also presented in 5G plans. Some publications[12 – 15] think that the rain-induced impacts on the terrestrial cellular scale link with several hundred meters of path length do not cause significant additional influences and even can be ignored, which is concluded based on the calculating results using the ITU-R models.

However, 5G mobile communication system will be applied to complex terrain and ground objects environment[7 – 8]. Consequently, the multipath propagation caused by terrain or ground objects is inevitable. Recent studies have revealed that the multipath propagation is an important factor affecting the millimeter-wave propagation characteristics[9 – 10]. Hence, with the increasing complexity of terrain and ground objects, the multipath effect is a key factor to affect the propagation characteristics of radio waves in 5G ground mobile link[16].

When it rains, multipath signals caused by terrain or ground objects will interact with raindrop particles, which may lead to more complex multipath signals[17 – 19]. In other words, every path will be affected by raindrop-caused random absorption and scattering, so the multipath signal is randomly changing. As a result, received signals include the multipath signals caused by raindrops scattering and/or by terrain or ground objects. A possible special case is that the raindrop absorption effect may also remove some terrain or ground objects-caused direct wave signals from the received signals, which means that those terrain or ground objects-caused signal arrival direc-

This work was supported in part by ZTE Corporation Program under Grant No. 2017ZTE01-01-06.

tions are objectively exist but the signals from those directions just contain the multipath signals caused by raindrop scattering. In a word, when a rain event occurs, the received signals in a complex terrain and ground object environment are likely to include two different kinds of multipath signals. According to the theory of vector superposition, the two different multipath signals will couple together and finally modulate channel effects together. The two kinds of multipath signals may cause destructive or constructive interference and magnify the atmospheric transmission effects. Namely, the integrated impacts caused by rain are likely to be much more serious than the effects forecasted by the ITU-R models, which are suitable for the propagation situation free from the effects of terrain and ground objects. Therefore, it may not be reliable to determine if the rain-induced effects can be ignored just according to the calculation results with the ITU-R models, and it is necessary to estimate the impacts of rain on mmW terrestrial links.

In this paper, the receiving signal time series at 35 GHz are measured in a selected multipath environment. The equivalent attenuation is obtained by comparing the received signals in rain with those measured in clear air. The measured data imply that, under a certain rain rate condition, the measured equivalent attenuation is much greater than the rain-induced attenuation calculated by the ITU-R P.530-12 model. The reasons for the enormous difference are analyzed by theoretical and experimental methods. According to the analysis results, it can be concluded that the transmission effects on mmW terrestrial links, such as attenuation-induced fade, equivalent attenuation, phase-shift, and atmosphere noise, in rain environment cannot be estimated by the classical models, which are built for computing the impacts induced solely by rain on mmW line of sight (LOS) links. In other words, it is necessary to adopt a completely new method for evaluating the transmission effects on mmW terrestrial links in a rain environment, such as fading, depolarization, noise, and phase shift. The conclusions given in this paper are significant for developing 5G mmW terrestrial links.

2 Equivalent Attenuation Measured in Selected Multipath Environment Under Rain Condition

Rain-induced attenuation should be the first consideration for designing mmW terrestrial links that work in a multipath environment. In order to study rain-induced attenuation characteristics of such the mmW links, we conducted a testing experiment using a terrestrial link at 35 GHz. The testing experiment system includes two parts: meteorological parameter measurement system and equivalent attenuation measurement system. As shown in **Fig. 1a**, the meteorological parameter measurement system is composed of an OTT Parsivel laser particle spectrometer and a computer. The equivalent attenuation measurement system includes a transmitter, a receiver, a spectrum analyzer and a computer, which are shown in **Fig. 1b**. The technical parameters of the OTT Parsivel laser particle spectrometer can be found in any official specification, which will not be introduced in this paper. The main parameters of the transmitter and the receiver are listed in **Table 1**.

In order to investigate the influence of rain on mmW terrestrial links, the testing system was located at the 5th floor of the West Building of Xidian University, where the random-ground-objects-induced multipath propagation can be neglected with very high approximation, but the static-ground-objects-induced multipath propagation was taken into consideration. **Fig. 2** shows the testing scenario, where the receiving and transmitting antennas are on the same side, namely, the receiving antenna can receive the signals reflected from the ground and the opposite wall. It should be noted that the Fresnel main region cannot be used to estimate the occurrence or nonoccurrence of multipath propagation, because it is only valid for the incidence case of a plane wave from a transmitting antenna to a receiving antenna. It is obvious that the propagation scenario in Fig. 2 is not the plane wave incidence case.

Fig. 3 shows our testing flow, where a spectrum analyzer is connected with the output port of the receiver's downconverter, hence the spectrum analyzer monitors the power level of re-

(a) Meteorological parameter measurement system (b) Equivalent attenuation measurement system

▲ **Figure 1. Testing experiment system of meteorological parameter measurement.**

▼**Table 1. Main parameters of the transmitter and the receiver**

(a) Parameters of the transmitting antenna and the receiving antenn

Polarization	Circular Honor Diameter	Half Power Beam Width of E Plane or H Plane	Gain
Right-handed circular polarization	50 mm	6°	17 dB

(b) Parameters of the transmitter

Output Frequency	Bandwidth	Output Power
35 GHz	<100 MHz	10 dBm±0.1 dBm

(c) Parameters of the receiver

Thresholds Power	Power Resolution	Output Frequency from Downconverter
−105 dBm	0.1 dBm	1.2 GHz

ceived signals and saves them into the computer by every minute; at the same time, the atmospheric parameters are recorded. The rain-induced equivalent attenuation time sequence can be obtained by subtracting the power level time sequence in rain from the reference power level. Note that the reference power level is the average power level of the signals that are received within 20 minutes before every rain event occurs.

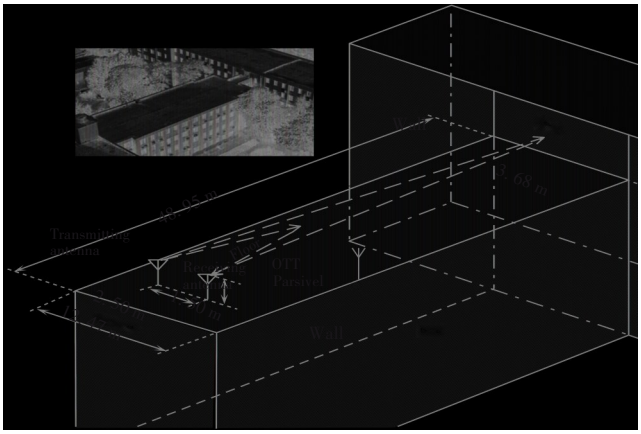

▲**Figure 2. Testing scenario in static-ground-objects-induced multipath propagation environment.**

During the measurement period from August 2017 to January 2018, about 3 500 minute time sequence of one-minute integration rain rate and the corresponding equivalent attenuation time series were recorded. In order to investigate the rain-induced influence on mmW terrestrial links, the rain-induced attenuation of 100 m path for the measured rain rate data is calculated by

$$A_{\text{calculation}} = (a_r R^{b_r}) \cdot 0.1, \tag{1}$$

$$a_r = \frac{1}{2}(a_h + a_v), \tag{2}$$

$$b_r = \frac{1}{2a_r}(a_h b_h + a_v b_v). \tag{3}$$

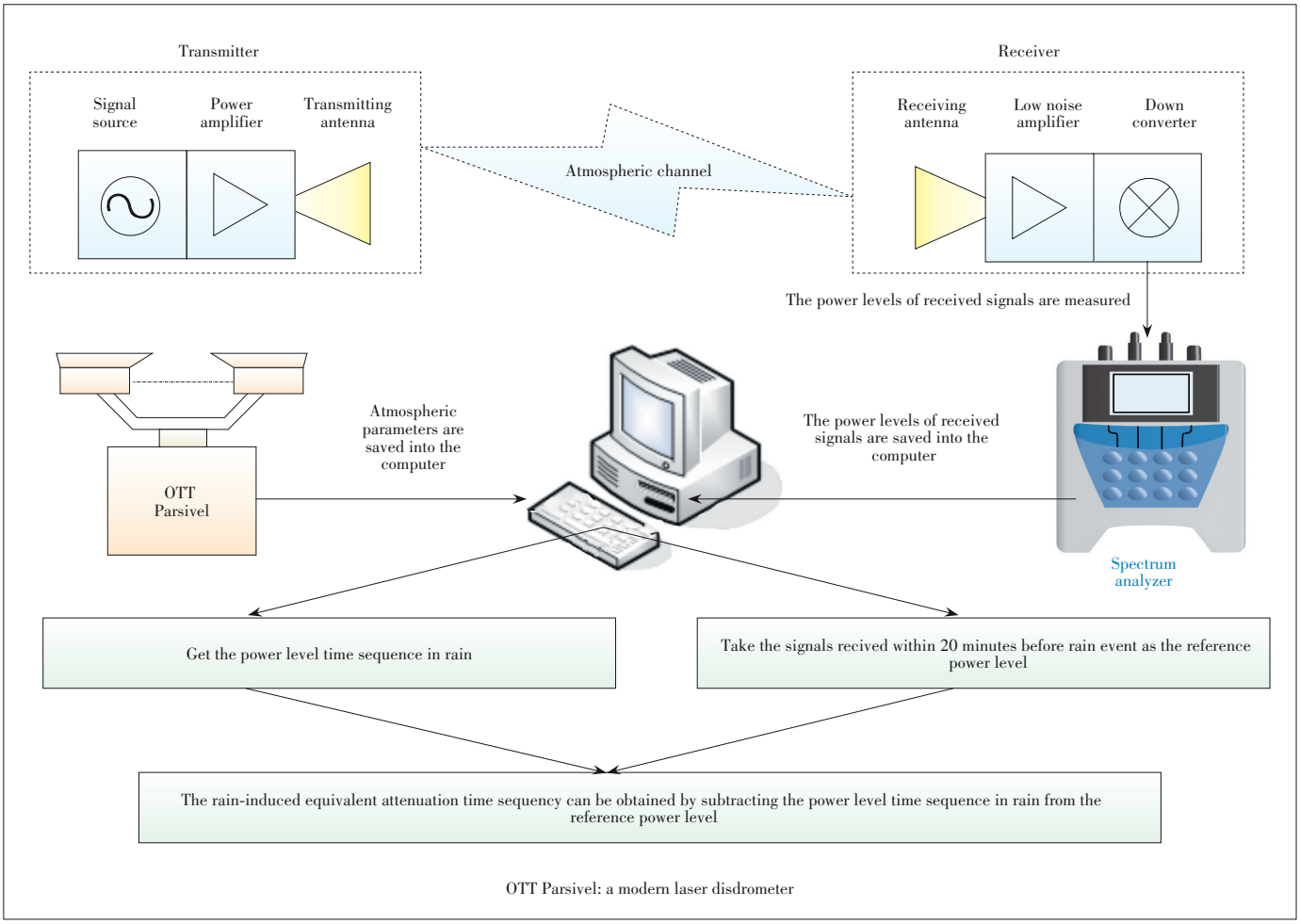

▲**Figure 3. Testing flow chart of meteorological parameter measurement.**

R in Eq. (1) notes the one-minute integration rain rate, which is replaced by the measured rain rate given in **Fig. 4**. a_h, a_v, b_h and b_v in Eqs. (2) and (3) are taken as a_h = 0.3374, a_v = 0.3224, b_h = 0.9047 and b_v = 0.8761 at 35 GHz, which are given in ITU-R P.838-3. Eq. (1) implies that it is true that the rain rate along the 100 m path in Fig. 2 is the same as that at the testing position. The measured equivalent attenuation and the calculated attenuation are shown in Fig. 4.

It is obvious that the values of the measured equivalent attenuation testing are larger than those of the calculated attenuation. The difference may be caused by the fact that the rain-induced attenuation is dependent not only on the rainfall type, raindrops' shape and size distribution, which determine the coefficients of a_h, a_v, b_h and b_v in Eqs. (2) and (3), but also on the space distribution of the rain rate, which determines the equivalent path length. In other words, the difference may arises from wrong values of a_h, a_v, b_h and b_v or the unseemly approximation of taking the geometry path length 0.1 km as the equivalent path length in Eq. (1). In addition, the difference in Fig. 4 may also be generated by wet antenna[20 – 23]. In order to verify the guesses mentioned above, another measurement in non-multipath environment was carried out. **Fig. 5** shows the testing scenario, which is the north campus of Xidian University. The transmitter and the receiver were placed on the top of two buildings with a distance of 820 m, respectively, and the height difference between the transmitter and the receiver was about 20 m. It was sure that there were no ground objects in the Fresnel region of the link in Fig. 5, the radius of which was about $0.5\sqrt{820 \times 0.0086}$ = 1.3256 m. In addition, it was sure that there were no ground objects in the two antennas' common beam space. Therefore, it is logical to consider the link in Fig. 5 as a LOS link.

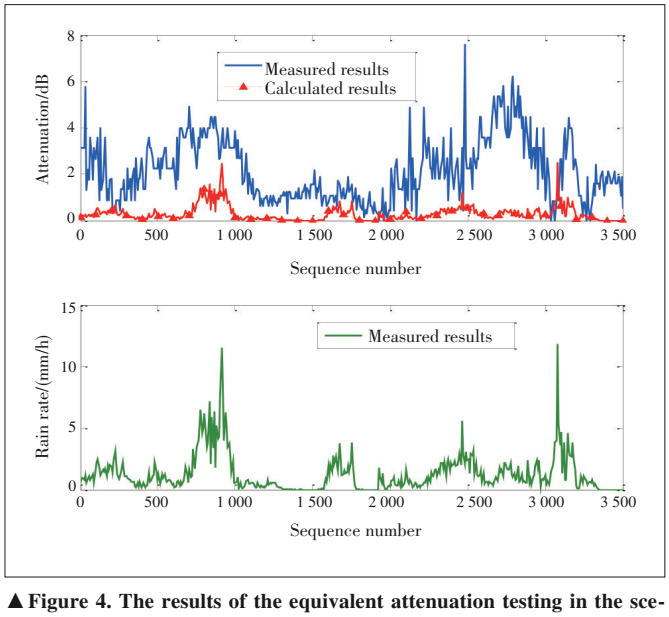

▲**Figure 4. The results of the equivalent attenuation testing in the scenario given in Figure 2.**

▲**Figure 5. Test scenario in line of sight (LOS) propagation environment.**

During the measurement period from March 2018 to June 2018, about 12 000 min time sequence of one-minute integration rain rate and the corresponding equivalent attenuation time series were recorded. The rain-induced attenuation was also calculated by Eq. (1). The measured attenuation and the calculated attenuation are shown in **Fig. 6**.

Fig. 6 shows that the measured attenuation and the calculated attenuation are approximatively matched. The subtle difference should be caused by the wet antenna mentioned in Refs. [20] – [23]. The results in Fig. 6 verify that the difference between the measured data and the calculated data in Fig. 4 is not mainly caused by the wrong a_h, a_v, b_h and b_v or the unseemly approximation of taking the geometry path length 0.1 km as the equivalent path length in Eq. (1). In other words, the obvious difference in Fig. 4 is likely to be caused by the coupled influence of rain-caused effects and ground-objects-induced multipath propagation, and it is not reasonable to regard rain-induced attenuation and other impacts on mmW terrestrial links as negligible factors just according to the traditional models, which are used to estimate the effects caused individually by rain. In what follows, the coupled influence mechanism of rain-caused effects and ground-objects-induced multipath propagation on mmW terrestrial link will be qualitatively analyzed.

3 Coupled Influence Mechanism of Rain-Caused Effects and Ground-Objects-Induced Multipath Propagation on MmW Terrestrial Links

In fact, the random variation of the power level received in the measured environment in Fig. 5 is attenuation-induced fade, and the attenuation is caused individually by rain. Furthermore, Eq. (1) is just used to calculate the attenuation induced solely by rain. Consequently, the attenuation calculated by Eq. (1) is approximatively matched with that obtained by subtracting the power level time sequence in rain from the ref-

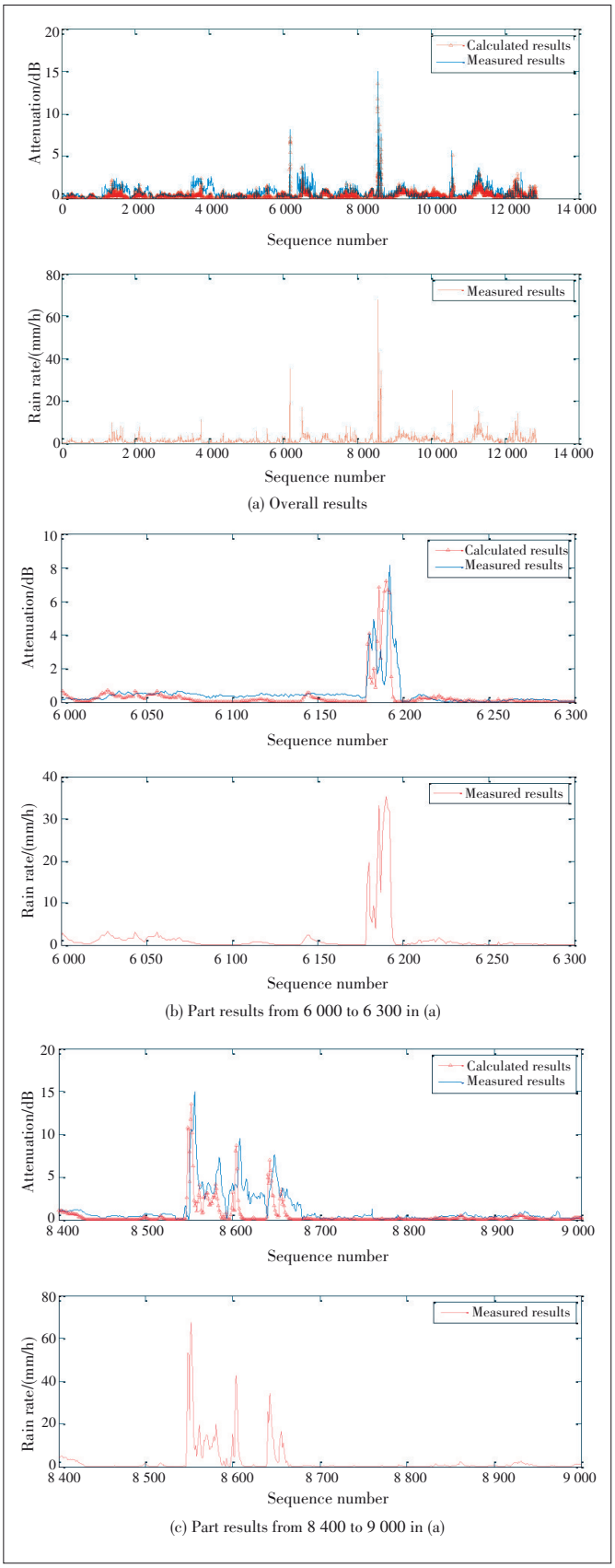

▲Figure 6. Results of attenuation testing in the scenario given in Figure 5.

erence power level, which is simply introduced in Section 2. However, each path of the multipath in Fig. 2 is affected by rain-induced effects, such as attenuation and phase shift. That is, the fade of the power level received in the scenario in Fig. 2 is induced by rain-caused multipath propagation. However, Eq. (1) is just used to calculate the attenuation induced only by rain. Therefore, the obvious difference in Fig. 4 is inevitable and not surprising at all.

In order to qualitatively analyze the coupled influence mechanism of rain-caused effects and ground-objects-induced multipath propagation on mmW terrestrial links, the simplest two-path propagation case is considered (**Fig. 7**). Suppose the vector complex amplitudes at the receiving antenna via Path-1 and Path-2 are $\mathbf{E}_1$ and $\mathbf{E}_2$, respectively. The vector complex amplitude of the total field can be written as

$$\mathbf{E} = \mathbf{E}_1 + \mathbf{E}_2. \tag{4}$$

The module $|\mathbf{E}|$ of $\mathbf{E}$ can be calculated by

$$|\mathbf{E}| = \sqrt{|\mathbf{E}_1|^2 + |\mathbf{E}_2|^2 + 2|\mathbf{E}_1| \cdot |\mathbf{E}_2| \cos(\theta_2 - \theta_1)}, \tag{5}$$

where θ_2 and θ_1 are the phase angles of $\mathbf{E}_1$ and $\mathbf{E}_2$. The phase angle θ of $\mathbf{E}$ can be calculated by

$$\theta = \operatorname{arctg} \frac{|\mathbf{E}_1| \sin(\theta_1) + |\mathbf{E}_2| \sin(\theta_2)}{|\mathbf{E}_1| \cos(\theta_1) + |\mathbf{E}_2| \cos(\theta_2)}. \tag{6}$$

Moreover, the total power is proportional to $|\mathbf{E}|^2$, which is expressed as

$$|\mathbf{E}|^2 = |\mathbf{E}_1|^2 + |\mathbf{E}_2|^2 + 2|\mathbf{E}_1| \cdot |\mathbf{E}_2| \cos(\theta_2 - \theta_1). \tag{7}$$

For the similar scenario in Fig. 2, in which the random-ground-objects-induced multipath propagation can be neglected with very high approximation, if rain does not occur, $|\mathbf{E}_1|$, $|\mathbf{E}_2|$ and θ_1, θ_2, are approximatively constant values.

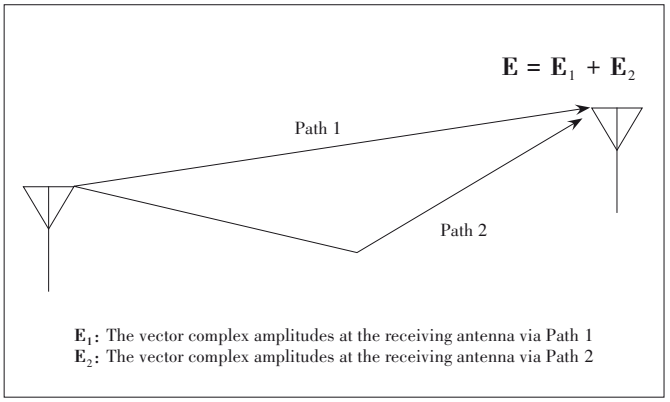

▲Figure 7. The two-path propagation case.

However, once rain occurs, $|\mathbf{E}_1|$, $|\mathbf{E}_2|$ and θ_1, θ_2 become random values because of rain-induced attenuation and scattering. Based on the results in Ref. [24], $|\mathbf{E}_1|$, $|\mathbf{E}_2|$ and θ_1, θ_2 can be expressed as

$$|\mathbf{E}_1| = \langle |\mathbf{E}_1| \rangle + |\mathbf{E}_1|_f, \tag{8}$$

$$|\mathbf{E}_2| = \langle |\mathbf{E}_2| \rangle + |\mathbf{E}_2|_f, \tag{9}$$

$$\theta_1 = \langle \theta_1 \rangle + \theta_{1f}, \tag{10}$$

$$\theta_2 = \langle \theta_2 \rangle + \theta_{2f}, \tag{11}$$

where $\langle |\mathbf{E}_1| \rangle$, $\langle |\mathbf{E}_2| \rangle$ and $\langle \theta_1 \rangle$, $\langle \theta_2 \rangle$ denote the mean values, $|\mathbf{E}_1|_f$, $|\mathbf{E}_2|_f$ and θ_{1f}, θ_{2f} denote the fluctuation induced by random scattering. Rain-induced attenuation and phase-shift determine $\langle |\mathbf{E}_1| \rangle$, $\langle |\mathbf{E}_2| \rangle$ and $\langle \theta_1 \rangle$, $\langle \theta_2 \rangle$, which slowly change. It should be noted that, as mentioned in Section 1, $\langle |\mathbf{E}_1| \rangle$ or $\langle |\mathbf{E}_2| \rangle$ may disappear because of very large attenuation, which means that rain-induced effect removes the terrain or ground objects-caused multipath. Rain-induced scattering determines $|\mathbf{E}_1|_f$, $|\mathbf{E}_2|_f$ and θ_{1f}, θ_{2f}, which rapidly change. $|\mathbf{E}_1|_f$ and $|\mathbf{E}_2|_f$ follow Rice distribution, while θ_{1f} and θ_{2f} follow uniform distribution from 0 to 2π. Therefore, even if in the simplest two-path propagation environment, $|\mathbf{E}|^2$, which is proportional to received power, is expressed as

$$\begin{aligned} |\mathbf{E}|^2 = {} & [\langle |\mathbf{E}_1| \rangle + |\mathbf{E}_1|_f]^2 + [\langle |\mathbf{E}_2| \rangle + |\mathbf{E}_2|_f]^2 + \\ & 2[\langle |\mathbf{E}_1| \rangle + |\mathbf{E}_1|_f] \cdot [\langle |\mathbf{E}_2| \rangle + |\mathbf{E}_2|_f] \cos\Big[(\langle \theta_2 \rangle - \\ & \langle \theta_1 \rangle) + (\theta_{2f} - \theta_{1f}) \Big]. \end{aligned} \tag{12}$$

Based on Eq. (12), it is quite clear that $(|\mathbf{E}_1|_f)^2$, $(|\mathbf{E}_2|_f)^2$ and the complex interference terms of $\langle |\mathbf{E}_1| \rangle \cdot |\mathbf{E}_1|_f$, $\langle |\mathbf{E}_2| \rangle \cdot |\mathbf{E}_2|_f$, $\langle |\mathbf{E}_1| \rangle \cdot \langle |\mathbf{E}_2| \rangle$, $|\mathbf{E}_1|_f \cdot |\mathbf{E}_2|_f$, $|\mathbf{E}_1|_f \cdot \langle |\mathbf{E}_2| \rangle$ and $|\mathbf{E}_2|_f \cdot \langle |\mathbf{E}_1| \rangle$ are introduced into $|\mathbf{E}|^2$. That is, the ground-objects-induced multipath propagation makes rain-induced scattering effect also more complicatedly impact the equivalent attenuation, because the received power is proportional to $|\mathbf{E}|^2$. It can be concluded that $|\mathbf{E}|^2$ will be more complex in more-path propagation environment. Eq. (12) also implies that quantitatively investigating $\langle |\mathbf{E}_1| \rangle$, $\langle |\mathbf{E}_2| \rangle$, $\langle \theta_1 \rangle$, $\langle \theta_2 \rangle$ and $|\mathbf{E}_1|_f$, $|\mathbf{E}_2|_f$, θ_{1f}, θ_{2f} is necessary for quantitatively analyzing $|\mathbf{E}|^2$. However, $\langle |\mathbf{E}_1| \rangle$, $\langle |\mathbf{E}_2| \rangle$, $\langle \theta_1 \rangle$, $\langle \theta_2 \rangle$ and $|\mathbf{E}_1|_f$, $|\mathbf{E}_2|_f$, θ_{1f}, θ_{2f} are decided by not only rain-caused effects but also wet antennas and wet ground surface. The impact of wet antenna on $\langle |\mathbf{E}_1| \rangle$ and $\langle |\mathbf{E}_2| \rangle$ is reported in some publications[20 – 23]. Moreover, it is very complicated to quantitatively analyze $\langle \theta_1 \rangle$, $\langle \theta_2 \rangle$, $|\mathbf{E}_1|_f$, $|\mathbf{E}_2|_f$, and θ_{1f}, θ_{2f} in rainy multipath environments. Therefore, Eq. (12) mathematically analyzes the coupled influence mechanism of rain-caused effects and ground-objects-induced multipath propagation on mmW terrestrial links, but the quantitative analysis of $|\mathbf{E}|^2$ will not be given in this paper. In a word, the traditional model for calculating rain-induced attenuation is suitable for LOS propagation case, while the quantitative analysis of $|\mathbf{E}|^2$ by the model similar to Eq. (12) is necessary for none LOS propagation case in rainy multipath environments. Hence, the obvious difference in Fig. 4 and the approximate accordance in Fig. 6 are logical.

According to the same mechanism, it can be concluded that other rain-induced effects on mmW terrestrial links, such as depolarization, phase-shift and atmosphere noise, cannot be estimated by traditional models, which are used in LOS propagation case. Therefore, the impacts of rain on 5G mmW terrestrial links are likely to be non-negligible on account of the coupled impaction of rain-induced effects and multipath propagation phenomenon, and it is necessary to deeply investigate the impacts of rain on 5G mmW terrestrial links.

4 Conclusions

The transmission effects, such as attenuation-induced fade, equivalent attenuation, phase-shift, and atmosphere noise, on mmW terrestrial links in rain environment are severer than those on mmW LOS links in rain because of the coupled action of rain-induced scattering and ground-objects – induced multipath propagation. For mmW terrestrial links, it is wrong to estimate rain-induced effects using traditional models, such as ITU-R models, which are suitable for LOS propagation cases. In other words, the impacts of rain on 5G mmW terrestrial communication system are likely to be non-negligible on account of the coupled impaction of rain-induced effects and multipath propagation phenomenon. It is necessary to build a model for quantitatively estimating the transmission effects on mmW terrestrial links in rain environment, which has not been included in any previous publications, but the mathematically analytic process in Section 3 is a good start and helpful to build such a model. The testing results in this paper are significant for developing 5G mmW terrestrial links.

References

[1] YUAN Y F, ZHAO X W. 5G: vision, scenarios and enabling technologies [J]. ZTE communications, 2015, 13(1): 3 – 10. DOI: 10.3969/j.issn.1673.5188.2015.01.001
[2] MARCHETTI N. Towards 5th generation wireless communication systems [J]. ZTE communications, 2015, 13(1): 11–19. DOI: 10.3969/j.issn.1673.5188.2015.01.002
[3] LUO F L. Signal processing techniques for 5G: an overview [J]. ZTE communications, 2015, 13(1): 20 – 27. DOI: 10.3969/j.issn.1673.5188.2015.01.003
[4] HAN S F, I C-L and XU Z K. Energy-efficient large-scale antenna systems with hybrid digital-analog beamforming structure [J]. ZTE communications, 2015, 13(1): 28–34. DOI: 10.3969/j.issn.1673.5188.2015.01.004
[5] WONG V W.S, SCHOBER R. Key technologies for 5G wireless systems [M]. Cambridge, England: Cambridge University Press, 2017: 15 – 64
[6] MACCARTNEY G R, RAPPAPORT T S, SAMIMI M K, et al. Millimeter-wave omnidirectional path loss data for small cell 5G channel modeling [J]. IEEE access, 2015, 3: 1573–1580. DOI: 10.1109/access.2015.2465848
[7] SAMIMI M K, RAPPAPORT T S. 3-D millimeter-wave statistical channel model for 5G wireless system design [J]. IEEE transactions on microwave theory and techniques, 2016, 64(7): 2207–2225. DOI: 10.1109/tmtt.2016.2574851
[8] MACCARTNEY G R, RAPPAPORT T S, SUN S, et al. Indoor office wideband millimeter-wave propagation measurements and channel models at 28 and 73 GHz for ultra-dense 5G wireless networks [J]. IEEE access, 2015, 3: 2388–2424. DOI: 10.1109/access.2015.2486778
[9] ISHIMARU A. Electromagnetic wave propagation, radiation, and scattering [M]. Hoboken, USA: John Wiley & Sons, 2017. DOI: 10.1002/9781119079699
[10] GONG S H, GAO Y F, SHI H B, et al. A practical MGA-ARIMA model for forecasting real-time dynamic rain-induced attenuation [J]. Radio science, 2013, 48(3): 208–225. DOI: 10.1002/rds.20028
[11] GONG S H, WEI D X, XUE X W, et al. Study on the channel model and BER performance of single-polarization satellite-earth MIMO communication systems at Ka band [J]. IEEE transactions on antennas and propagation, 2014, 62 (10): 5282–5297. DOI: 10.1109/tap.2014.2342754
[12] XU X L, LIU M, XIONG J B, et al. Key technology and application of millimeter wave communications for 5G: a survey [J]. Cluster computing, 2019, 22(S5): 12997–13009. DOI: 10.1007/s10586-018-1831-x
[13] NIU Y, LI Y, JIN D P, et al. A survey of millimeter wave communications (mmwave) for 5G: opportunities and challenges [J]. Wireless networks, 2015, 21(8): 2657–2676. DOI: 10.1007/s11276-015-0942-z
[14] ICHKOV A, ATANASOVSKI V, GAVRILOVSKA L. Potentials for application of millimeter wave communications in cellular networks [J]. Wireless personal communications, 2017, 92(1): 279–295. DOI: 10.1007/s11277-016-3850-3
[15] ZHOU L, XIAO L M, YANG Z, et al. Path loss model based on cluster at 28 GHz in the indoor and outdoor environments [J]. Science china information sciences, 2017, 60(8): 080302. DOI: 10.1007/s11432-017-9127-6
[16] JAECKEL S, RASCHKOWSKI L, WU S B, et al. An explicit ground reflection model for mm-wave channels [C]//IEEE Wireless Communications and Networking Conference Workshops (WCNCW). San Francisco, USA: IEEE, 2017: 19–22. DOI: 10.1109/wcncw.2017.7919093
[17] RAPPAPORT T S, SUN S, SHAFI M. 5G Channel model with improved accuracy and efficiency in mmwave bands [J]. IEEE 5G tech focus, 2017, 1(1): 1–6
[18] ZHAO X W, LI S, WANG Q, et al. Channel measurements, modeling, simulation and validation at 32 GHz in outdoor microcells for 5G radio systems [J]. IEEE access, 2017, 5: 1062–1072. DOI: 10.1109/access.2017.2650261
[19] RAPPAPORT T S, SUN S, SHAFI M. Investigation and comparison of 3GPP and NYUSIM channel models for 5G wireless communications [C]//IEEE 86th Vehicular Technology Conference (VTC-Fall). Toronto, Canada: IEEE, 2017: 24–27. DOI: 10.1109/vtcfall.2017.8287877
[20] ZHANG X, ZHAO Z W, LIN L K, et al. Rain attenuation characterization on 5G millimeter wave links with short distance [J]. Chinese journal of radio science, 2017, 32(5): 507–512, 2017.DOI: 10.13443 / j.cjors.2017091901
[21] GARCIA-RUBIA J M, RIERA J M, BENARROCH A, et al. Estimation of rain attenuation from experimental drop size distributions [J]. IEEE antennas and wireless propagation letters, 2011, 10: 839 – 842. DOI: 10.1109/lawp.2011.2163609
[22] BLEVIS B. Losses due to rain on radomes and antenna reflecting surfaces [J]. IEEE transactions on antennas and propagation, 1965, 13(1): 175–176. DOI: 10.1109/tap.1965.1138384
[23] KHARADLY M M Z, ROSS R. Effect of wet antenna attenuation on propagation data statistics [J]. IEEE transactions on antennas and propagation, 2001, 49(8): 1183–1191. DOI: 10.1109/8.943313
[24] GONG S H, HUANG J Y, ZHAO X L. Rain-induced effects on the envelope probability density functions in multipath channels [J]. Radio science, 2008, 43(2): 1–11. DOI: 10.1029/2007rs003759

Biographies

GONG Shuhong (shgong@xidian.edu.cn) received the M.S. and Ph.D. degrees in radio physics from Xidian University, China in 2004 and 2008, respectively. Now, he is a professor and a doctorial tutor at Xidian University. His research interest focuses on radio wave propagation in near-earth space and its applications.

ZHANG Xingmin is currently working toward the M.S. degree in radio physics from Xidian University, China. His current research interest is MIMO wireless channel modeling for 5G communication system.

DOU Jianwu received the Ph.D. degree from Beijing University of Technology, China in 2001. Since 2001, he has been in charge of research and system design of the radio resource management algorithm in UMTS, TD-SCDMA and LTEv1 at ZTE Corporation. From 2006, he has also been responsible for system simulation of 2G, 3G, 4G, and WLAN as a department director at ZTE Corporation. His research interests include RRM, system simulation, wireless channel sounding and modelling, data mining, high frequency physical layer design, and MTC.

HUANG Weifang received the master degree in electromagnetic field and microwave technology from the School of Electronic Engineering, Xidian University, China in 2006. He is a senior engineer of the Algorithm Department, ZTE Corporation. Since May 2008, he has been engaged in the research of the communication system. His main research directions are wireless environment modeling, high-frequency communications, and communication system networking simulation modeling.

ZTE Communications Guidelines for Authors

Remit of Journal

ZTE Communications publishes original theoretical papers, research findings, and surveys on a broad range of communications topics, including communications and information system design, optical fiber and electro-optical engineering, microwave technology, radio wave propagation, antenna engineering, electromagnetics, signal and image processing, and power engineering. The journal is designed to be an integrated forum for university academics and industry researchers from around the world.

Manuscript Preparation

Manuscripts must be typed in English and submitted electronically in MS Word (or compatible) format. The word length is approximately 3000 to 8000, and no more than 8 figures or tables should be included. Authors are requested to submit mathematical material and graphics in an editable format.

Abstract and Keywords

Each manuscript must include an abstract of approximately 150 words written as a single paragraph. The abstract should not include mathematics or references and should not be repeated verbatim in the introduction. The abstract should be a self-contained overview of the aims, methods, experimental results, and significance of research outlined in the paper. Five carefully chosen keywords must be provided with the abstract.

References

Manuscripts must be referenced at a level that conforms to international academic standards. All references must be numbered sequentially in-text and listed in corresponding order at the end of the paper. References that are not cited in-text should not be included in the reference list. References must be complete and formatted according to *ZTE Communications Editorial Style*. A minimum of 10 references should be provided. Footnotes should be avoided or kept to a minimum.

Copyright and Declaration

Authors are responsible for obtaining permission to reproduce any material for which they do not hold copyright. Permission to reproduce any part of this publication for commercial use must be obtained in advance from the editorial office of *ZTE Communications*. Authors agree that a) the manuscript is a product of research conducted by themselves and the stated co-authors; b) the manuscript has not been published elsewhere in its submitted form; c) the manuscript is not currently being considered for publication elsewhere. If the paper is an adaptation of a speech or presentation, acknowledgement of this is required within the paper. The number of co-authors should not exceed five.

Content and Structure

ZTE Communications seeks to publish original content that may build on existing literature in any field of communications. Authors should not dedicate a disproportionate amount of a paper to fundamental background, historical overviews, or chronologies that may be sufficiently dealt with by references. Authors are also requested to avoid the overuse of bullet points when structuring papers. The conclusion should include a commentary on the significance/future implications of the research as well as an overview of the material presented.

Peer Review and Editing

All manuscripts will be subject to a two-stage anonymous peer review as well as copyediting, and formatting. Authors may be asked to revise parts of a manuscript prior to publication.

Biographical Information

All authors are requested to provide a brief biography (approx. 100 words) that includes email address, educational background, career experience, research interests, awards, and publications.

Acknowledgements and Funding

A manuscript based on funded research must clearly state the program name, funding body, and grant number. Individuals who contributed to the manuscript should be acknowledged in a brief statement.

Address for Submission

http://mc03.manuscriptcentral.com/ztecom

ZTE COMMUNICATIONS
中兴通讯技术(英文版)

ZTE Communications has been indexed in the following databases:

- Abstract Journal
- Cambridge Scientific Abstracts (CSA)
- China Science and Technology Journal Database
- Chinese Journal Fulltext Databases
- Index of Copurnicus
- Inspec
- Ulrich's Periodicals Directory
- Wanfang Data

ZTE COMMUNICATIONS
Vol. 18 No. 3 (Issue 71)
Quarterly
First English Issue Published in 2003

Supervised by:
Anhui Publishing Group

Sponsored by:
Time Publishing and Media Co., Ltd.
Shenzhen Guangyu Aerospace Industry Co., Ltd.

Published by:
Anhui Science & Technology Publishing House

Edited and Circulated (Home and Abroad) by:
Magazine House of ZTE Communications

Editorial Correspondence:
Add: 12F Kaixuan Building, 329 Jinzhai Road,
Hefei 230061, P. R. China
Tel: +86-551-65533356
Email: magazine@zte.com.cn
Website: https://tech-en.zte.com.cn

Annual Subscription: RMB 80
Printed by:
Hefei Tiancai Color Printing Company

Publication Date: September 25, 2020

China Standard Serial Number: ISSN 1673-5188
CN 34-1294/TN